Monopile Forever

Overcoming the Technical Boundaries of Monopile Foundations in Deep Waters

Yuan Enzo Liu

Technische Universiteit Delft

TU Delft

Monopile Forever

Overcoming the Technical Boundaries of Monopile Foundations in Deep Waters

by

Yuan Enzo Liu

to obtain the degree of Master of Science
at the Delft University of Technology,
to be defended publicly on Tuesday August 3, 2021 at 1:00 PM.

Student number:	4444485	
Project duration:	October 24, 2020 – August 3, 2021	
Thesis committee:	prof. dr. ir. A. Metrikine	TU Delft, Chair
	dr. ir. B. C. Ummels	TU Delft, Supervisor
	ir. T.P.J. Kamphuis	DOT B.V., Supervisor
	ing. M. Kurstjens	Sif Group, Supervisor

An electronic version of this thesis is available at `http://repository.tudelft.nl/`.

Sif

TU Delft

DOT
POSITIVE DISPLACEMENT

Abstract

Since the introduction of the first offshore wind farm in 1991, the demand for offshore renewable wind energy has experienced exponential growth all around the world. To supply this demand, the power rating and corresponding dimensions of offshore wind turbines have grown significantly. Due to the ever-shrinking availability of easily accessible shallow water sites and the abundance of high quality wind resources in deeper water, the industry is stimulated to come up with innovative, yet cost effective, solutions to tap into these deep water sites. Historically, the use of monopile foundations has been an important facilitator of cost reduction due to its relative ease of manufacturability, transportability and installability. Monopile foundations have, however, thus far only been used in relatively shallow water depths. With jacket-type and floating support structures remaining relatively costly, the question arises if the monopile could yet be scaled up further to be used in water depths beyond the current 40-60 m for future, 10+ MW wind turbines.

The goal of this research is to investigate the technical feasibility of monopile foundations in the water depth 'gap' of 60 to 120 meters, which is currently claimed by jackets, for large wind turbines and determine critical design parameters for up-scaling monopiles to these depths. With an eye on future developments a 15 MW reference turbine is adopted and to make the research widely applicable the Hywind Scotland site in the Northern North Sea is selected, a well-documented reference site with a very severe wind and wave climate.

To define monopile designs, a parametric (static) monopile geometry optimization tool is developed in Excel, which transfers the environmental data to forcing components. The monopile geometry is optimized for first natural frequency and ULS resistance (yield and global buckling) by varying the outer diameter and wall thickness along the structure. It was found that the ULS check is governed by the inertial wave forcing during survival case (50 year return period storm conditions). As the acting wave frequency is way lower than the system natural frequency, the monopile can be adequately assessed using a static approach. To assess the effect of critical variables, the tool is used to define monopile geometries for water depths ranging between 60 and 120 m, target first natural frequencies of 0.15, 0.17 and 0.20 Hz and a range of soil types, while complying with known manufacturing limits. The results show that all designs are within manufacturing limits and resistance against ULS decreases for lower target frequencies, making 0.15 Hz monopiles unfeasible.

In contrast to the ultimate limit failures, the fatigue damage is largely incurred from normal rather than ultimate wave states, which embrace the first natural frequency of the system, thus warranting a full dynamic analysis. In order to assess the fatigue resistance of 0.17 and 0.20 Hz monopiles, which pass the ULS check, an analytical full dynamic model is developed in Maple based on the fundamental equations of motion, including (added) mass, aerodynamic damping and soil/structural stiffness. The model is verified and validated against numerical modelling using ANSYS Finite Element Analysis software and found to be in very good agreement. The Maple model is then used to test the fatigue performance. It is found that the fatigue damage accumulated over the 25-year design lifetime is governed by the bending stress cycles induced by inertial wave forces. The model is used to generate a transfer function between this wave forcing and the resulting bending stress over the entire range of present wave frequencies. The transfer functions are used to transfer the wave scatter diagram to accumulated fatigue damage against a B2, C1 and D graded S-N curve. The analysis results show increasing fatigue damage for decreasing first natural frequency due to the increasing slenderness and more prominent interference with present wave frequencies, which causes th 0.15 and 0.17 Hz monopiles to fail on fatigue damage. Given the very demanding site conditions assumed in this research, more slender monopiles may be feasible in deep waters with a milder wave climate.

Over all, the results show no fundamental technical limitations for a monopile supported 15 MW wind turbine in water depths of up to 120 meters, provided that the stiffness of the structure is sufficiently high. Since steel usage increases for increasing stiffness, technically feasible monopiles will need to be relatively heavy, thus costly. Therefore, a range of strategies to reduce steel weight have been quantitatively assessed. It is found that the amount of steel can be reduced up to 35% by adopting higher-grade steel types and improved weld quality. Based on the fundamental limiting factors for monopiles found, also a novel hybrid floating-fixed bottom concept is proposed aiming at steel weight reduction. Although the concept can be considered promising, it does add complexity to the system and unfortunately does not (yet) result in steel reduction.

Preface

The end of an incredibly turbulent and demanding period is on the horizon. It was impressive to see that due to great resilience, most of us have managed to adapt and reinvent ourselves during this difficult time. This thesis work is the final task in the Offshore & Dredging Engineering study program and also marks my closing endeavours as a student at the Delft University of Technology. I am happy and proud that I managed to put my somewhat stubborn desire to make quick progress aside to take a step back, re-evaluate and achieve my final goal.

I am very grateful to the TU Delft, DOT BV and Sif Group for granting me the opportunity to complete this important phase of my academic career with a project including practically all aspects of my preceding studies. It led me through a perfect learning journey which combined the academic and the industry world. I would like to thank everyone who, in any way, contributed to the project; you made the past period memorable. In particular I would like to thank:

Bart Ummels, for your continuous unconditional support, guidance and introduction to the 'real offshore world'. You made me appreciate my own work more and inspired me to see the bigger picture. I loved the way we communicated and we will definitely meet again in the future, whether it's to grab a beer or to design a novel wind turbine foundation concept!

Michel Kurstjens, for your essential strategy input on my thesis approach. It can be challenging to combine seemingly unrelated parts of work to a coherent story. Thank you for being available at any time when I got lost during this quest. I hope my findings will help Sif make monopiles forever!

Thijs Kamphuis, I am so glad to see you back as passionate as always, after a very demanding period for you. You helped 'complete the circle' until the very last days of my thesis work, tying up the loose ends. It was a pleasure working with you and we will definitely do so in the future.

Andrei Metrikine, for again and again showing me masterly the beauty of dynamics and challenging me to walk the extra miles. This was a perfect showcase on how a well-taught course can be directly utilized to solve real-life thought-provoking problems.

My Father, Mother and Sister, for your unconditional support and patiently listening to my complaints. Whether it were engineering lessons or life lessons, you helped me improve my work and myself until now and will do so in the future. Thanks for being my family, lots of love!

My Friends, for all the much needed valuable distraction during this interesting period. Your support during the past months have helped me tremendously. Let's hope the world opens up soon so we can celebrate!

Yuan Enzo Liu
Delft, August 2021

Be not afraid of going slowly, be afraid only of standing still. - Confucius

不怕慢，只怕站.

Contents

List of Figures

List of Tables

Nomenclature

Latin Symbols

$\dot{v}$	Wave particle acceleration perpendicular to cylinder
A	Cross sectional area
A_r	Swept rotor area
A_w	Wind loading surface
C_D	Drag coefficient
C_L	Lateral foundation flexibility coefficient
C_m	Inertia coefficient
C_R	Rotational foundation flexibility coefficient
C_S	Substructure flexibility coefficient
C_T	Thrust coefficient
D	Outer diameter
d	Duration
D_{rotor}	Rotor diameter
E	Youngs modulus steel (210 GPa)
F_B	Base shear
F_D	Drag force
f_{FB}	Fixed base first natural frequency
F_I	Inertia force
f_n	First natural frequency
F_T	Thrust force
f_t	Target first natural frequency
f_y	Yield stress
g	Gravitational acceleration
H_{max}	Max Wave height
H_s	Significant wave height
I_{eq}	Equivalent area moment of inertia
I_P	Area moment of inertia monopile
I_T	Area moment of inertia tower
k	Wave number
L	Total system length
L_p	Pile embedded length
L_s	Length interface height to mudline
M	Overturning moment
m_{eq}	Equivalent mass per unit length
m_{top}	Top mass
n_h	Horizontal coefficient of sub-grade reaction
T_{m02}	Mean zero crossing period
T_n	First natural period
T_p	Peak period
T_z	Zero up-crossing period
$u_{1hr;100m}$	1-hour mean wind speed at 100 m above sea level
u_{e50}	50-year return period mean wind speed
u_{gust}	Wind gust speed
u_{hub}	Wind speed at hub height
u_{ref}	Wind speed at reference height
u_z	Wind speed at height z
V	Axial force
v	Wave particle velocity perpendicular to cylinder
W	Elastic section modulus
z_i	Interface level
z_{ref}	Reference height

Greek Symbols

α_c	Current shear parameter
α_w	Wind shear parameter
χ	Bending stifness ratio tower/monopile
Δ	Roughness
δ	Marine growth
Δ_{WL}	Water level variation

$\Delta_{z_{air}}$	Air gap
γ_b	Blockage factor
γ_e	Safety factor for environmental loads
γ_g	Safety factor for permanent loads
γ_m	Material safety factor
γ_s	Wave spreading factor
Λ_1	Turbulence scale parameter
ω	Wave frequency
ϕ	Length ratio tower/monopile
ψ	Wake amplification factor
ρ_{air}	Air density (1.025 kg/m^3)
ρ_{water}	Water density (1025 kg/m^3)
σ_{vm}	Von Mises stress
σ_x	Axial stress
τ_{xy}	Shear stress
$\zeta*$	50-year highest wave elevation above SWL
ζ	Wave crest height

Abbreviations

K_C	Keulegan-Carpenter Number
R_e	Reynolds number
DFF	Design Fatigue Factor
FLS	Fatigue Limit State
LAT	Lowest Astronomical Tide
OEM	Original Equipment Manufacturer
QTF	Quadratic Transfer Function
RAO	Response Amplitude Operator
RNA	Rotor Nacelle Assembly
SFRF	Stress Frequency Response Function
SPAR	Single Point Anchor Reservoir
SWL	Still water level
TLD	Tuned Liquid Damper
TMD	Tuned Mass Damper
TRL	Technical Readiness Level
ULS	Ultimate Limit State

1 Introduction

1.1. Current Industry Status and Future Outlook

Since the introduction of the first offshore wind farm, Vindeby, in October 1991, the offshore wind industry has experienced exponential growth. With the global energy transition and the high population density in coastal areas, the demand for offshore wind energy is continuously increasing. The global wind market surged nearly 30% per year between 2010 and 2018, benefiting from major technology improvements. Recently, new countries have taken strides forward on offshore wind. China, for example, added 3 GW of offshore wind capacity in 2020, the most of any country and half of the new global offshore wind capacity in this year [36]. Study shows that the potential of untapped offshore wind is theoretically able to supply more than the total amount of electricity consumed worldwide today [46]. The ongoing innovation results in significant cost reductions in the offshore wind industry, which clears the path to become globally competitive with fossil fuels and other sources of (renewable) energy within the next decade [46].

The average turbine power rating in the offshore wind industry increased from 3 MW in 2010 to 5.5 MW for projects completed in 2018 [48]. In the same period, annual capacity factors[1] for offshore wind projects increased from 38% to 43%. Future turbines are expected to reach capacity factors well over 50% excluding wake losses[2]. The increasing capacity factors are partly due to the technical innovation of the turbine system itself, but also importantly by making use of sea acreage with better quality wind resource. These areas are generally located further out at sea and have larger water depths. Technical potential is often divided between shallow water (i.e. < 60m) and deep water (i.e. 60 - 2,000 m) sites. Historically speaking, the shallow water sites are suitable for established fixed-bottom foundations and are relatively easy to access, while the deep water sites require new innovative solutions to be tapped into. The theoretical potential of the shallow water sites is 87,000 TWh per year, which is twice the global electricity demand in 2040 under the Stated Policies Scenario [46]. Whereas deep water sites have a theoretical potential of 330,000 TWh per year, which is eleven times the global electricity demand in 2040 [46].

Although offshore wind has the theoretical potential to meet the increasing renewable energy demands, not all sites are accessible with current state-of-the-art techniques. This limits the total amount of feasible locations. The exploitation of deeper water locations is currently costly, making it difficult to make projects in these sites financially attractive. A major contributor to cost reduction of offshore wind (and herewith making offshore wind energy competitive with other energy sources) is the monopile foundation. This simple foundation type consists of a steel pipe which is driven into the seabed. The turbine is hereafter attached to the monopile using a transition piece. Due to its relative ease of manufacturability, transportability and installability it serves as a very efficient, reliable and most of all cheap base for offshore wind turbines. However, the significant water depths of the mentioned deep water locations make the use of monopiles difficult, if not impossible. With the ongoing cost reductions in offshore wind and increasing number of offshore projects not requiring subsidies in shallower waters [17], developments are required to bring down costs in order to

[1] Capacity factor describes the average output over the year with respect to the maximum rated power capacity.

[2] Wake loss refers to the effect on the space behind a turbine that is marked by decreased wind speed on a downstream wind turbine due to the fact that the turbine itself used the energy in turning the blades.

open up the potential of the deeper waters. Innovation in various aspects of the wind industry is gaining momentum to achieve this goal. With the increasing size (meaning both wattage and rotor size) of new turbines, fewer units are required to produce an equal amount of energy. Hence, the number of moving components and (to a lesser, but still significant extent) the lengths of offshore inter-array cabling decrease and the capital expenditure shifts to the support structures. In short: in order to meet future energy demand, better and cheaper support structure solutions are required to facilitate cost-efficient installation of state-of-the-art wind turbines in deeper waters.

Figure 1.1 shows indicative shares of capital costs per component for offshore wind projects completed in 2018 [46]. As the capital expense of the turbine itself depends on the turbine type rather than the water depth, the absolute costs of this share is independent of the water depth of the project location. Hence, when pushing conventionally monopile supported wind turbines in to deeper water, the relative capital cost share of the foundation increases significantly [59]. Det Norske Veritas (DNV) indicated that the biggest cost saving opportunities lay within the optimization of support structures [7]. This confirms the benefits of innovative (cheaper) foundation solutions for deeper waters in the overall capital expenditures.

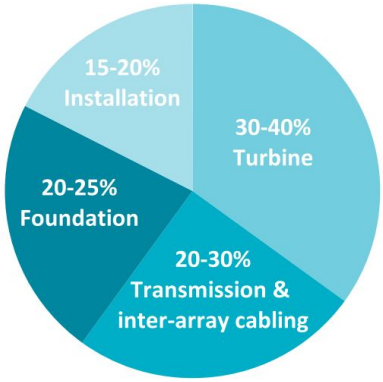

Figure 1.1: Indicative shares of capital cost by component [46]

1.2. Scale of (Future) Wind Turbines

To meet the increasing demand of renewable offshore wind energy, the power rating of wind turbines is pushed to higher levels. The turbine with the highest power rating to be used in a wind farm in the current pipeline is GE's Haliade-X at the Dogger Bank wind farm [26]. The original prototype was designed for a power rating of 12 MW, but was optimized to operate at 13 MW output. Electrical engineer groups and chip-makers are even working on extending the capacity to 14 MW output using the same rotor blades [35]. The Haliade-X is equipped with a 220 meter diameter rotor at a total height of 248 meter. Wind turbines with power ratings and rotor diameters exceeding that of the Haliade-X are already in development by several manufacturers. Siemens Gamesa recently presented their largest turbine called SG 14-222 DD [74]. This 222 meter rotor diameter turbine has a starting output of 14 MW with the future aim of reaching 15 MW. The final company in the wind turbine 'G3' is Vestas. Vestas presented the world's largest turbine (V236-15MW) in the beginning of 2021 which has a starting output rating of 15 MW with a rotor diameter of 236 meters [62]. Serial production of this turbine is expected to start in 2024 and a prototype is in the pipeline for 2022.

Even though larger rotor blades typically come with higher power ratings per turbine, the increasing size of the blades also comes with several drawbacks, examples being transportability and the increasing flexibility of the blades causing larger blade tip deflections, which makes keeping the required clearance between the tower and the blades challenging [47]. It is yet uncertain whether the offshore wind industry will keep scaling up the power ratings of the turbines with their corresponding rotor diameters. Increasing the wattage of the used wind turbines is a trade-off between the number of required units and the increasing cost of the individual wind turbines. However, current market developments indicate that the offshore wind turbine sizes are not yet stabilizing, and further up-scaling up to possibly 20 MW can be expected until 2030.

1.3. Wind Energy Potential in Deep Water

Currently Europe is the pioneer in developing solutions to ever deeper water projects and is expected to account for nearly 40 % of the global offshore wind market by 2040 [46]. This makes European waters (especially the North Sea) the most-likely location to deploy the first full scale wind farms in deeper waters. Figure 1.2 shows the water depths of European waters. It shows that the conquest of intermediate water depths (30-60 meters) yields a considerable addition of offshore area. However, significant extra offshore area is available with 60-100 m water depth or more.

The overall performance of a wind farm depends strongly on the quality of the wind resource. Figure 1.3 shows the wind resources in European waters (the explanation of the color scheme is given in Figure 1.4). If this map is placed over the water depths map in the same area shown in Figure 1.2 it indicates that a lot of high wind resource sea acreage is located in waters deeper than 60 meters. This means that, generally speaking, the potential output with the same wind turbine will be higher in deeper, yet untapped, waters.

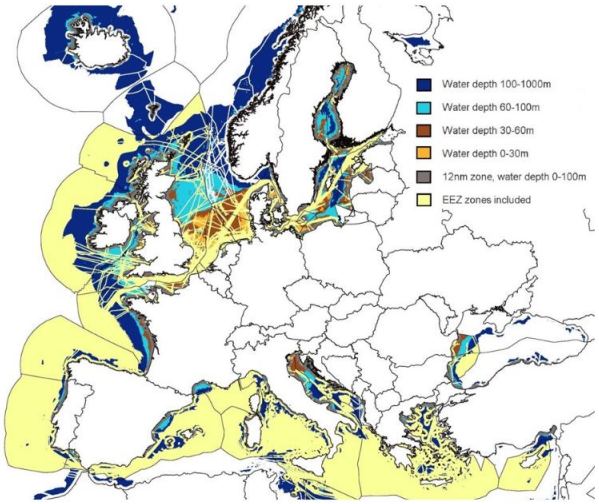

Figure 1.2: Water depths of European waters [30]

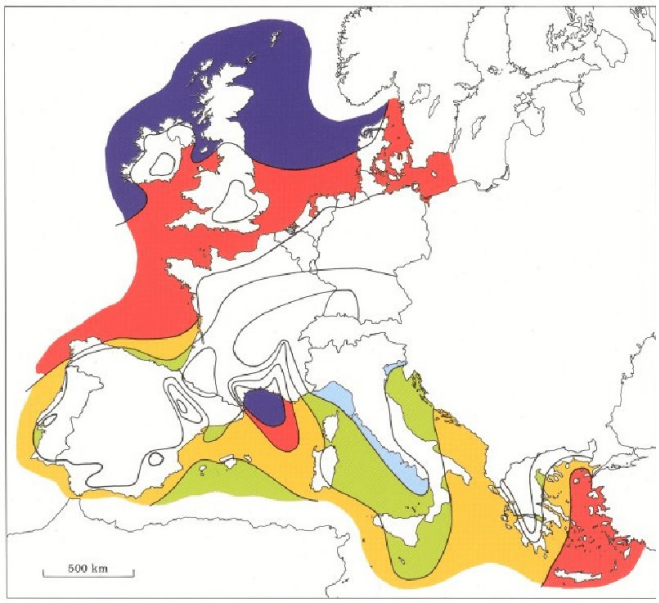

Figure 1.3: Wind resources in European waters [88], see Figure 1.4 for color scheme

A simplified estimation of the potential power output can be done following Equation 1.1 [53].

$$\text{power per unit area} = \frac{\text{power per wind turbine}}{\text{land area per wind turbine}} = \frac{\frac{1}{2}\rho_{air} u_{hub}^3 \frac{\pi}{8} D_{rotor}^2}{(10 D_{rotor})^2} = \frac{\frac{1}{2}\rho_{air} u_{hub}^3 \frac{\pi}{8}}{100} \tag{1.1}$$

Figure 1.4 shows the full potential power per unit area (excluding the capacity factor) for a 15 MW wind turbine and increasing average wind speeds, extrapolated to hub height. A spacing between the wind turbine of 10 times the rotor diameter is assumed to minimize wake losses [46]. The figure shows a non-linear trend, indicating that an increase in average wind speed at hub height results in notable extra power output potential following a cubic law. The colors correspond to the map given in Figure 1.3.

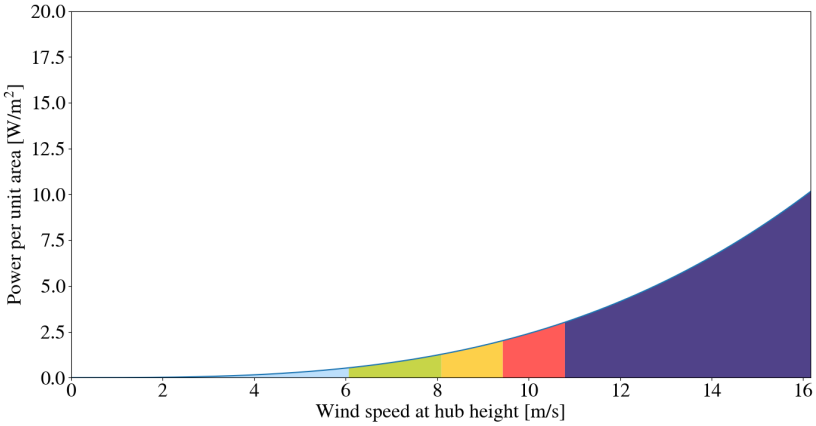

Figure 1.4: Potential power per unit area for different wind speeds

The inability to place wind farms in deeper waters is likely to constrain future growth of the offshore wind industry, by limiting the geographical reach and thus the potential scale of deployment [55]. Taking Scotland as an example, over 70% of its estimated offshore wind potential is located in waters deeper than 60 meters [68]. Therefore, research is done into methods to unlock the deep water areas. These developments include floating wind turbines, alternative bottom-fixed support concepts but also extending the limits of established foundation types like monopiles [86]. Jacket-like support structure types, which are proven technologies but previously rejected due to the high costs, are also reassessed for financial viability [7, 40].

1.4. Pushing the Boundaries of the Monopile

The design drivers for pushing conventional monopiles into future larger water depths include 15+ MW rated wind turbines with rotor diameters of up to 240 meters and hub heights of 150 meters above the platform [34]. The larger swept area in combination with the harsh conditions on open sea cause a significant increase of forcing. The deeper waters will result in a growing arm between the forcing and foundation, causing the overturning moments to increase. To withstand the loading, larger monopile diameters and wall thicknesses are required, resulting in larger loading surfaces for wave and current forcing. These factors drive the possibilities with the current state-of-the-art production and installation capacity to their limits [28]. Conventional connection techniques such as, bolted flange and grouted connection are also reaching their technical boundaries as the maximum available bolt size (M72) is already adopted in offshore wind projects and first projects using un-certified M80 bolts starting production soon [51, 60]. Innovative solutions such as the slip joint connection [27] are already proven in offshore conditions and new techniques such as the C1 Wedge connection [16] are being developed to overcome this limitation.

The monopile is and has been the industry's favorite support structure type due to its simplicity, ease of installation and most importantly, economics. Even though the application of the monopile was deemed not financially feasible beyond 25 meters water depths, monopile supported turbines have been installed up

to 40 meters deep. Production yards and installation contractors are responding to the developments and are investing in larger production equipment and fleets with higher lifting capacity to make the application of monopiles in intermediate water depths (40-60 meters) for 13-14 MW wind turbines possible. Although these technical developments provide a great range of extra potential area to tap into, these areas are heavily crowded by other industries and sites with higher potential are located in even deeper waters. Due to the economics and relative simplicity of the monopile the offshore wind industry is eager to expand the possibilities of the monopile to unlock these sites, without the needs of costly jacket or floating structures [46].

With a quickly emerging market such as the offshore wind industry, it is important to think ahead of the current state of the art. Various researches into the developments of wind turbines up to 20 megawatt have been conducted and floating wind pilots have been installed in water depths up to 220 meters. Figure 1.5 shows capital costs of offshore wind projects commissioned in mid-2020s.

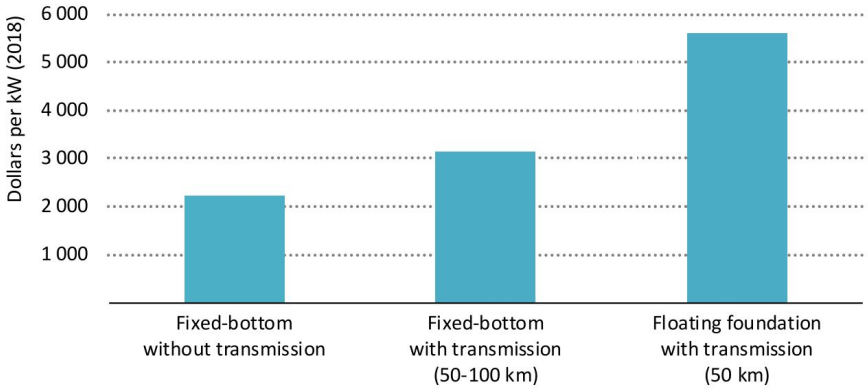

Figure 1.5: Capital costs of offshore wind projects commissioned in mid-2020s [46]

It shows that floating wind capital costs are approximately twice as high as those of fixed-bottom foundations. As floating foundations are still in an early stage of demonstration, there is still significant potential for future cost reduction. Since the capital expense of floating wind turbines (mooring excluded) is practically independent of water depths, their financial benefit over bottom-fixed foundations will become increasingly evident with growing water depths. However, mooring of floating turbines in water depths below 100 meter is a challenging task and can be very expensive [89]. Additionally, SPAR-type floating turbines, which provide most stable and cost-effective floating foundations, require a minimum water depth of around 75 meters to be technically feasible for relative small turbines due to their large draft [66]. With increasing turbine size, the required water depth is expected to increase significantly. For example, the water depth for a 15 MW turbine should, ideally, be larger than 150 m. Semi-submersible and TLP types of floaters can be used for shallower water, but they will require more steel and are very difficult to moor, making them less cost-effective than SPARs for now.

Besides floating concepts, established bottom-fixed structures are also being readopted to deploy wind turbines in deeper water areas. The jacket is widely perceived as the current best option "beyond monopiles". Their commercial use for offshore wind turbines started in 2006 with the Beatrice project [70], but jackets are still used in present time. For the East Anglia ONE wind farm, 102 three-legged jacket structures holding 7 MW wind turbines were deployed 43 km off the Suffolk coast in the UK in 2020. This was the sole project starting up in 2020 using jacket technology and yet the world's largest ever in number of turbines with such foundation. The 300 km^2 sea acreage has an average water depth of 45 meters with a maximum depth of approximately 53 meters. Another example, the 950 MW Moray East offshore wind farm, is scheduled to operate with one hundred 9.5 MW wind turbines supported by four-legged jacket structures in water depths up to 57 meters. The wind farm is expected to be fully operational in 2022. Due to the amount of required labor the use of jacket support structures has generally been more expensive than monopile foundations. Additionally, installation of jackets typically take more time since 3 or 4 pin piles need to be be hammered into the seabed prior to placing the jacket, whereas the monopile requires only a single lift, grip and hammer operation [85].

This shows that there is a gap of water depths in the range of 60 to 120 meters, that for now are claimed by relatively expensive jacket support structures. The areas with these water depths have great potential, not only in Europe, but also in North America and South East Asia [46]. The design of a novel technique to overcome these water depth in a financially attractive manner has great potential to unlock vast amounts of untapped wind resources.

1.5. Current Deeper Water Techniques

As stated, the demand for better deep water support structure solutions haven't gone unnoticed. This section will assess some of the projects deployed in deeper waters to complete the image of the current status of deep water offshore wind energy. Keeping in mind the rapid developments in the offshore wind industry, only projects including turbines with a power rating of 7 MW or higher are considered in this section. There is a vast number of floating wind support structure concept under development, which are not all on same level of technical readiness. This section will only discuss floating concepts that are either deployed in full-scale or are planned to be so before the end of 2022.

The first full-scale offshore floating wind farm was the Hywind Scotland project, which consists of five 6 MW turbines supported on SPAR type structures as shown in Figure 1.6. The original pilot of 2.3 MW was scaled to 6 MW and is expected to be deployed using 8 MW turbines in 2022 [29]. This 88 MW project is dubbed 'Hywind Tampen' and is located on the west coast of Norway with water depths up to 300 meters. The SPAR-type floater is a concept adopted from the oil and gas industry. It consists of a steel and a concrete cylinder moored to the seabed filled with a ballast of water and gravel to ensure that the wind turbine stays upright in offshore conditions [6]. Due to its large draft, it requires significant water depths not only for deployment but also for construction. Therefore, the assembly of foundation and turbine for the Tampen project had to be conducted in the deep fjords on the Norwegian coast. This deep water requirement is the case for all SPAR-type projects.

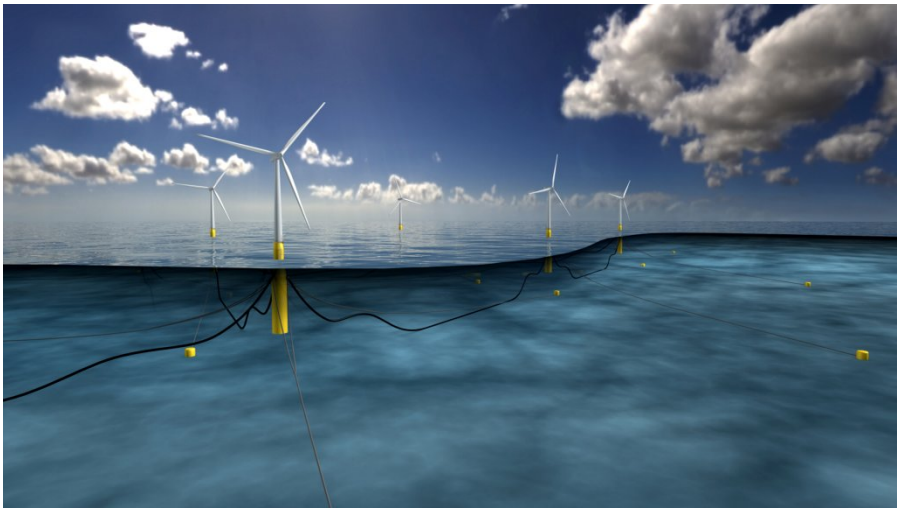

Figure 1.6: Render of Hywind Schotland [29]

Another widely proven floating support structure is the semi submersible-type floater, also adopted from the oil and gas industry. It comprises a few large column cylinders connected to each other by tubular members. The wind turbine will either sit on one of the cylinders or may be positioned at the geometric center of the columns and is supported by lateral bracing members. The floatation stability is provided by the waterplane area of the columns [6]. The first floating wind farm in continental Europe called 'WindFloat Atlantic' was installed in front of the coast Portugal in waters with a depth 100 meters. It consists of three 8.4 MW turbines mounted on semi submersible foundation [10]. A project called Golfe du Lion Wind Farm is planned to be fully operational by 2022. Here, the semi-submersible structures will hold 10 MW wind turbines [31].

1.6. Research Objective and Questions

As stated, the mooring of floating foundations in water depths below 100 meters is very challenging. This drives up the already relatively high costs of these foundation types. The remaining established foundation types used in intermediate water depths are jacket-like and monopile structures. Jacket-like structures have already proven their technical feasibility in deep waters. However, due to the amount of manual labor during production and longer installation time, the relative costs are high. Monopile foundations have thus far never been used in deep waters and have therefore not proven their technical feasibility, despite being the industry's current favorite. The main objective of this research reads:

"Investigate the technical feasibility of monopile foundations in water depths of 60 to 120 meters for large wind turbines and determine the critical design parameters for further upscaling."

This objective is reached by answering the following research questions:

1. What are the weights and operational characteristics of future wind turbines?
2. What are the current and foreseen limitations for manufacturing and installation?
3. What are the fundamental changes for monopile support structure design when entering deeper waters?
4. What are the critical design parameters for support structures?
5. Is the use of monopile foundations technically feasible for the target water depths?
6. Given the answers to research questions 3,4 and 5, what would an alternative monopile-concept look like that could go beyond the fundamental limitations while maintaining (most) of the benefits of the monopile?

1.7. Methodology and Thesis Outline

In order to reach the final goal of finding a working solution for the transition depths between established bottom-fixed and floating methods, several steps need to be taken. The thesis will be subdivided into two parts. The results of part one will provide the base input for part two. The general outline of the thesis is listed below and the location of the answers to the research questions (RQ) are indicated by number:

Part 1: Technical Feasibility of Monopile Foundations in Deep Water

1. Introduction to the current industry status and outlook. The motivation of pushing wind turbines to deeper waters is discussed and current boundaries of deep water foundation techniques are stated. Also, a literature overview is provided on the current knowledge on offshore support structure engineering, monopile design and anticipated limitations to the monopile (**RQ 1**).

2. The establishment of the design basis. The used environmental data of the reference location is explained and transferred to forcing components. This is done for two design load cases. A parametric model is established that takes environmental data and general turbine data as input and returns an optimized monopile geometry based on loading and natural frequency criteria. In order to investigate the effect of increasing water depth, the substructure is optimized for 4 different water depths: 60, 80, 100 and 120 meters (**RQ 2**).

3. Analysis model testing for ultimate limit states (ULS) and fatigue limit states (FLS). For these analyses a static and dynamic model are established respectively. The details of the models and the validation and verification through Finite Element Analysis (FEA) software are discussed and results and conclusions are presented (**RQ 3**).

4. Monopile geometry optimization. The results of the monopile geometry optimization process are discussed and conclusions are drawn. These conclusions serve as the base of the proposed alternative strategies as will be discussed in Part 2. As no strict technical limitations were found from the analysis, the solutions will focus on steel usage reduction. The solutions are an interplay between passing the ULS and FLS, depending on the selected stiffness of the system (**RQ 4, 5**).

Part 2: Alternative Solutions on Increasing the Feasibility of Usage

1. The critical parameters for extending the use of monopile based foundations are assessed and solutions are proposed. Previous attempts found in literature on mitigating these limitations and their results are presented.
2. Based on the findings of Part 1 and the critical parameters, additional model runs are performed to assess the effect of damping, higher quality welds and higher grade steel type usage. The results are used to establish what foreseeable limits there are to the monopile in deep waters.
3. Given the foreseeable limitations and considering the limiting factors, a novel concept combining the knowledge of floating and bottom-fixed foundations will be introduced and high level results in the feasibility of this concept will be presented (**RQ 6**).

1.8. Assumptions and Delineations

In order to narrow down the broad range of variables to focus on the thesis problem, some assumptions and delineations must be made. As the input parameters can vary strongly per locations or turbine type, a reference location and turbine must be selected. Also, as the Thesis covers a broad range of research fields, a set of different softwares is required. The selected references and substantiation for the selection are explained in detail below.

1.8.1. Reference Wind Turbine

The ever larger turbines come with problems such as keeping the required blade tip clearance between the rotor and the tower, transportability and installability [47]. With the aim of designing a support structure that will hold for the far future, a suitable wind turbine should be adopted as model input. To account for future developments, while not overestimating the size of upcoming turbines, the International Energy Agency (IEA) 15 MW turbine is adopted for this analysis [34]. This reference turbine is well-documented in a reference document specially tailored for researches such as the present study. As the IEA reference data doesn't provide information on the nacelle dimensions, the dimensions of the Haliade-X nacelle are adopted [64]. The general key figures for this reference wind turbine are given in Table 1.1.

Table 1.1: Key Parameters for the IEA Wind 15-MW Turbine [46][64]

Parameter	Value	Unit
Cut-in wind speed	3	m/s
Rated wind speed	10.59	m/s
Cut-out wind speed	25	m/s
Design tip-speed ratio	90	-
Minimum rotor speed	5.0	rpm
Maximum rotor speed	7.66	rpm
Maximum tip speed	95	m/s
Rotor diameter	240	m
Hub height	150	m
Nacelle width	10.0	m
Nacelle length	12.0	m
Nacelle height	10.4	m
Rotor nacelle assembly mass	1,017	t
Tower mass	860	t
Tower Length	133.3	m
Tower Basediameter	10.0	m

1.8.2. Site Selection

To assess the performance of the support structure in open sea, a reference site selection is required. The main selection criteria were for the site to have water depths up to 120 meters, harsh environmental conditions and for it to be well-documented. Firstly, because deep water sites with high quality wind resources generally come with harsh conditions. Secondly, if the structure will function in these conditions, it will persevere most locations in the world making the research widely applicable. Finally, a well-documented site reduces the number of unknown factors and assumptions making it a more credible reference.

The North Sea is well known for having one of the harshest environmental conditions on the globe with extreme wave heights and wind speeds [3]. Hence, for this study the Hywind Scotland wind farm [54], located in this sea, is selected as reference site. The power site is centred at 57.45º N, 01.31º W at Buchan Deep on the east coast of Scotland, shown in Figure 1.7. Offshore wind projects in water depths of 60 to 120 meters are relatively new to the industry, so the extensive exploration conducted for this pioneering project provides a unique base for this research. The variety in water depth (95-129 m) fulfills the first requirement as it covers the upper limits of the target depths.

The deployment of the Hywind SPAR foundations required proper evaluation of the soil conditions at the proposed turbine deployment area in order to ensure integrity of the mooring system. This soil analysis is also of great importance to bottom-fixed support structure design, such as monopiles and jackets. The observation of geological lithologies in boreholes and CPTU results at the reference site showed soil types ranging from sand with gravel to gravelly clay [76]. As soil reaction is highly non-linear, locality dependent and time dependent modelling a general soil model that will hold for all monopiles is impossible. Therefore in this thesis a set of assumptions is made and a range of soil types will be assessed to investigate the sensitivity of the design to this parameter.

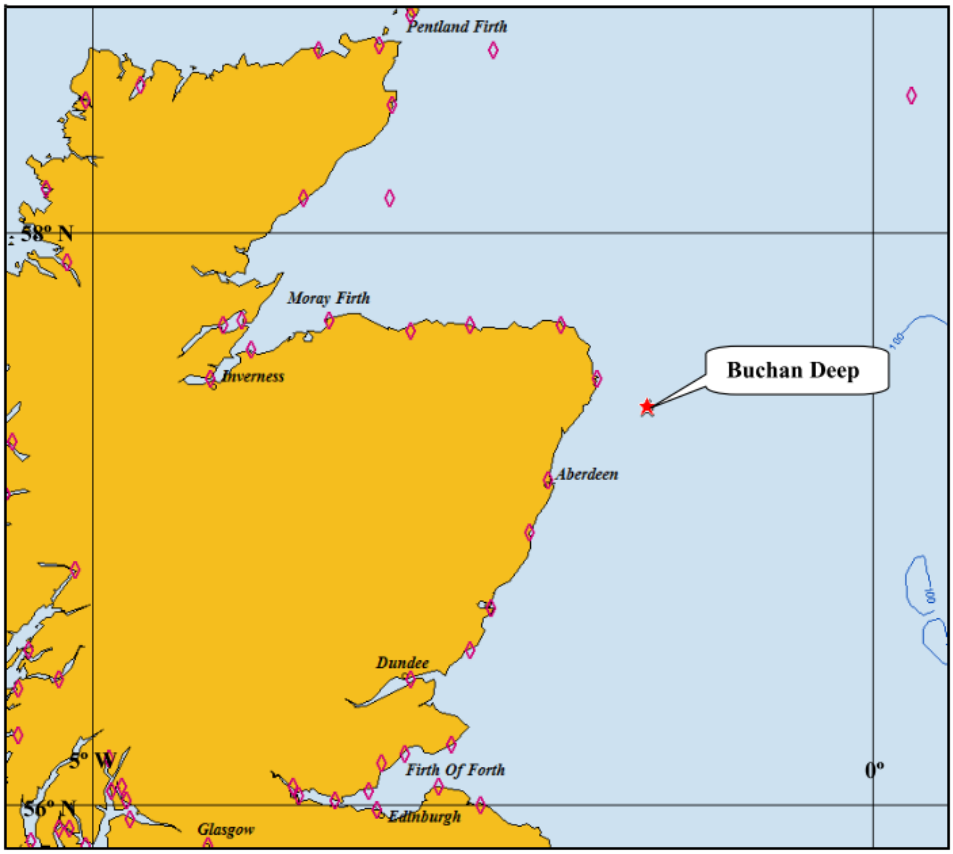

Figure 1.7: Map showing position of Hywind site at Buchan Deep

1.8.3. Tool Selection

Throughout this thesis many analysis tools are developed within a variety or combination of software. The reason behind the selection of each specific software is a combination of availability, applicability and the student's previously gained experiences during his course work. A short reasoning behind the selection of each used software is given below.

Excel

Microsoft's Excel with added macros is used to establish the main monopile optimization framework. This software was selected as the amount of input parameters is very large and one can quickly lose overview. The different tabs help organizing the input and output per subject and combine them where required. Since it is very difficult if not impossible to include dynamic effect into the static Excel framework, it is important to validate the usability of the Excel model for each step of the thesis using appropriate software and expand the results where required.

Maple

Maple is a symbolic and numeric computing environment which is used to analytically introduce dynamics into the system. The student's previous experience with the software in courses that connect to the thesis work, the structured overview of the calculation process and the readily available license makes this the preferred choice for analytical derivations and numerical computations. Additionally, the software allows for animated plotting, which accelerates the comprehension of the dynamics.

Ansys (Mechanical/AQWA)

Ansys Mechanical offers a dynamic FEA environment which is used to validate and verify the analytically established Maple models. There are multiple similar softwares available such as Comsol, OpenFAST and Orcaflex. However, previous software experience and the availability of an academic license were decisive in the selection.

As the presented novel hybrid concept was based on a reference floating foundation, topics such as mooring-, diffraction and radiaton analysis become important. The AQWA suite, developed for naval architects, is a software package that allows one to analyse these complex movements and the resulting forces can be exported to the Mechanical suite.

Part 1

2

Design Basis

In order to assess the performance of new foundation techniques, a base case of conventional and proven concepts needs to be defined as the reference, including monopile and jacket foundations. Jackets have proven their technical feasibility in water depths of 60 to 120 meters [55]. However, monopile foundations have thus far not been deployed in areas with these depths. This section presents high-level results of pushing the conventional monopile in water depths of 60 to 120 meters. It provides insight into how the order of magnitude of forcing, weight and dimensions change for increasing water depths. In the following subsections, the different components of the model are assessed and required assumptions are stated.

2.1. Environmental Data

The optimization process is conducted to ensure structural integrity during power production and parked conditions (more extensive elaboration on the load cases is given in Section 2.3). In reality the extreme waves will show non-linear behavior due to a variety of interactions [44]. However, an in-depth analysis of the effect of non-linear wave interaction is considered beyond the scope of this research and the effects are accounted for by the wave crest over maximum wave height ratio. The power production load case is assessed under 'rated'[1] conditions and the parked case under 50 year return period storm conditions [25]. A summary of both data sets is given in Table 2.1 and the data selection of critical parameters is assessed in the following subsections. A scatter diagram for waves for this site is used for fatigue damage assessment in Chapter 5.

Table 2.1: Environmental data based on Buchan Deep

	Rated	50-Year Return	Unit
Water level Deviation	2.10	3.20	m
Significant wave height	1.77	10.90	m
Max wave height	3.29	19.70	m
Crest / H_{max}	0.53	0.57	-
Wave period max	7.9	12.8	s
Mean zero crossing period	5.3	11.4	s
Peak period	7.4	14.6	s
Current speed	1.20	1.80	m/s
10 min mean wind speed at 10m	6.16	34.50	m/s

2.1.1. Wind Data

To provide the wind input of the load cases, vertical mean wind speed profiles are modeled using the power-law given by Equation 2.1 [45]. Vertical wind profiles can strongly vary under different circumstances. DTU professor Sven-Erik Gryning stated that even differences in day and night time can have a significant influence on the profile shape [37]. However, both the rated and 50 year return conditions are considered

[1] At the rated wind speed, the turbine is able to generate electricity at its maximum, or rated, capacity.

to predominantly occur during overcast weather situations at the chosen location. In these conditions the power-law profile is generally applicable. The wind shear parameter (α) determines the shape of the vertical wind profile. The adopted wind shear parameters are 0.11 for 50 year return conditions and 0.2 for rated conditions [47].

$$\frac{u_z}{u_{ref}} = \left(\frac{z}{z_{ref}}\right)^{\alpha_w} \tag{2.1}$$

Where:

u_z = wind speed at height z
u_{ref} = wind speed at reference height (z_{ref}), taken at 10 m above water level
α_w = wind shear parameter

In addition to mean wind speeds, the turbulence in the wind is a highly relevant design parameter for the wind turbines. Turbulence, including wake-induced turbulence due to neighbouring wind turbines, is an important design factor for determinating fatigue during the WTG's lifetime [72]. The maximum wind forces during rated conditions are expected to occur under rated wind speeds with a 50-year extreme operating gust (EOG) hitting the rotor [5]. The control system is assumed to be unable to respond fast enough to reduce impact [25]. The hub height gust magnitude is given by the Equation 2.2 [47].

$$u_{\text{gust}} = \text{Min}\left\{1.35\,(0.8u_{\text{e50}} - u_{\text{hub}})\,;\quad 3.3\left(\frac{0.15\,(0.75u_{\text{hub}} + 5.6)}{1 + 0.1\left(\frac{D_{rotor}}{\Lambda_1}\right)}\right)\right\} \tag{2.2}$$

Where:

Λ_1 = the turbulence scale parameter (equal to 42 m for $z \geq 60m$)
u_{e50} = the 50-year return period mean wind speed at 10 m (34.50 m/s)
u_{hub} = the rated wind speed at the hub (10.59 m/s)

The wind speed over height during such an extreme operating gust event can be found following Equation 2.3. Here T is commonly set to 10.5 s and the maximum wind speed will occur at $t = T/2$ [47].

$$u_{total}(z) = u(z) - 0.37u_{\text{gust}}\,\sin(3\pi t/T)(1 - \cos(2\pi t/T)) \tag{2.3}$$

During the 50-year return period storms the turbulence is assessed using the Extreme Wind speed Model (EWM) [25]. The turbulence is given following Equation 2.4 and the profile follows the power-law given in Equation 2.1.

$$u_{gust} = 0.11u_{hub} \tag{2.4}$$

Figure 2.1 shows the total vertical wind profiles for both the load cases under maximum turbulence gust.

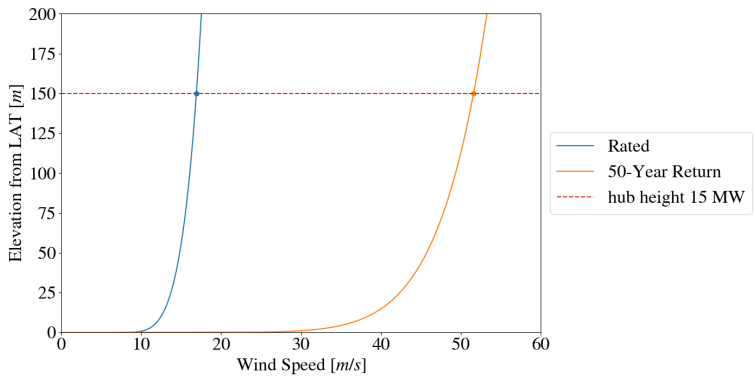

Figure 2.1: Total vertical wind profile for rated and 50-year return conditions

2.1.2. Hydro Data

The submerged part of an offshore wind turbine increases for increasing water depths. In addition to this, the relative loading surface of the hydrodynamic forcing also increases due to the larger required monopile diameters. Hence, the hydro data becomes increasingly important for deeper waters. The metocean data for the Hywind Scotland project provided by Equinor [54] states clear design wave parameters for the 50-year return conditions, which are adopted for this load case and summarized in Table 2.1. As the waves at Buchan Deep are a combination of swell and wind waves, the relation between wind speed and wave conditions is not evident. The report provides an empirical relation between the 1-hour mean wind speed at 100 meters above sea level ($u_{1hr;100m}$) and the significant wave heights (H_s), given by Equation 2.5. This relation is used to estimate the wave conditions under rated wind speeds [54].

$$H_s = 0.719 \cdot \exp^{0.0832 \cdot u_{1hr;100m}} \tag{2.5}$$

To determine the maximum wave height associated with the significant rated wave height, it is multiplied by a factor 1.95 [44]. This is based on Equation 2.6 for a 3 hour storm (d) with the mean zero crossing period (T_z) given in Table 2.1.

$$\text{mod}\left(\underline{H}_{max}\right) \approx H_{m_0} \sqrt{\frac{1}{2} \ln \frac{d}{T_z}} \tag{2.6}$$

The peak periods associated with the maximum and significant wave heights are listed in the metocean report [54]. The relation between the peak periods (T_p) and zero up-crossing period (T_z) is given in DNVGL-CG-0130 [20] and differs for the two load cases. The relations are given by Equation 2.7

$$\begin{aligned} T_{p;rated} &= 1.286 T_{z;rated} \\ T_{p;50year} &= 1.405 T_{z;50year} \end{aligned} \tag{2.7}$$

The current speed for the 50-year return condition is given in the data set. 80% of the 1-year return current speed is taken as the current speed under rated conditions. In order to capture the survival scenario, the 50 year extreme gust and wave height occur at the same time.

2.2. Loading of Structure

The total loading that has to be withstood by the monopile consists of a variety of components. The loads can be divided in two main forcing groups: wind loads and hydrodynamic loads. The following subsections include the force determination of the two forcing groups.

2.2.1. Wind loading

As the increasing power output potential of future wind turbines is partly due to the significant growth in swept area of the rotors, the wind accounts for a notable part of the force balance. The total force generated by the wind consists of four main thrust or drag components:

- Rotor Thrust or Drag
- Nacelle Drag
- Tower and Dry Monopile Drag
- Platform Drag

In this study the drag force on the platform is considered negligible with respect to the other forcing components and is therefore not included in the design process. The optimization of the turbine tower shape is not included in this research and the provided tower geometry from the reference turbine is adopted [34]. The total wind forcing is the sum of all thrust (F_t) and drag (F_D) forces which can be found with Equation 2.8 and 2.9, respectively [11, 41].

$$F_t = \frac{1}{2} \rho_{air} A_r C_T u_w^2 \tag{2.8}$$

$$F_D = \frac{1}{2} \rho_{air} A_w C_D u_w^2 \tag{2.9}$$

Here A_r is the swept rotor area during power production and A_w is the loading surface of the assessed drag component. u_w is the occurring wind speed, given by the vertical wind profiles in Figure 2.1. The thrust

(C_T) and drag (C_D) coefficients of the rotor differ for the different load cases and are given in Section 2.3. For the tower a drag coefficient of 0.65 is used (associated with smooth cylinders) and for the nacelle a drag coefficient of 1.00 is adopted (associated with a square surface) following DNVGL-RP-C205 [23].

Combining the wind profiles from Section 2.1.1 from LAT + crest height upwards with Equations 2.8 and 2.9, the wind forcing over tower height can be found of which an example is shown in Figure 2.2. The starting height of the wind forcing is the level from which the wind can freely flow, between crests and troughs wind velocities can vary dramatically. The orange arrow indicates the resulting rotor drag or thrust forces on the nacelle and rotor, which act at the hub height.

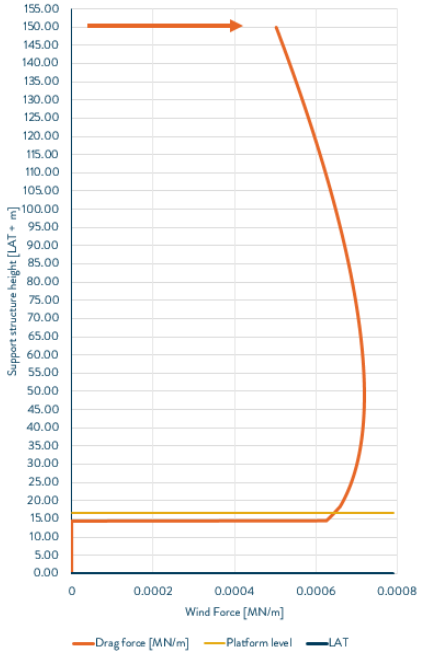

Figure 2.2: Drag over height for 15 MW turbine under 50-year return conditions

2.2.2. Hydrodynamic Loading

With deeper water and larger diameters the hydrodynamic loading surface of the foundation and arm of the hydrodynamic forcing increase. Although the exact hydrodynamic loading depends strongly on the substructure geometry, it is evident that the total magnitude increases for deeper water. Following the metocean study [54], marine growth may be assumed to increase linearly from zero to the given values in Table 2.2 in the course of a couple of years. These values are adopted for the calculations.

Table 2.2: Thickness of marine growth of Buchan Deep.
Data from NORSOK Standard N-003 Section 6.6.1 [57]

Water depth [m]	Thickness [mm]
Above +2	0
+2 to -40	100
Below -40	50

In this design the monopiles do not feature a boat landing or ladders. Omitting these features is a novel technology used by Ørsted in their Hornsea Two park [58]. The use of so called 'Get Up Safe' systems boost both safety and potential for construction and through-life cost reductions. The elimination of external ladders streamlines the foundation, resulting in no additional diameter increases besides the given marine growth, which in its turn reduces the hydrodynamic loading surface at the wave impact zone. In this design the impact of ice on the structure is neglected, large marine growth such as mussels typically results in signif-

icant extra ice growth and thus increase of loading surface.

The hydrodynamic forcing is a combination of drag (F_D) and inertia (F_I) forces and can be calculated using Equations 2.10, 2.11 and 2.12 [23, 84] for a stationary cylinder.

$$F_D = \frac{1}{2}\rho_w C_D D v|v| \qquad (2.10) \qquad F_I = \frac{\pi}{4} C_m \rho_w D^2 \dot{v} \qquad (2.11) \qquad F_{tot} = \sqrt{F_D^2 + F_I^2} \qquad (2.12)$$

Where:

C_m = Hydrodynamic inertia coefficient
C_d = Hydrodynamic drag coefficient
ρ_w = Sea water density
D = Monopile diameter including marine growth
$\dot{v}$ = The water particle acceleration
v = The water particle velocity

The drag coefficient consists of a roughness related part, C_{DS}, factored by a Keulegan-Carpenter number related wake amplification factor, $\psi(K_C)$, which results in a drag coefficient given in Equation 2.13.

$$C_D = C_{DS}(\Delta) \cdot \psi(K_C) \qquad (2.13)$$

For high Reynolds numbers ($R_e > 10^6$), which are the applicable conditions here, the roughness dependent part is given by Equation 2.14 [23]:

$$C_{\mathrm{DS}}(\Delta) = \begin{cases} 0.65 & ;\Delta < 10^{-4}(\text{smooth}) \\ \left(29 + 4 \cdot \log_{10}(\Delta)\right)/20 & ;10^{-4} < \Delta < 10^{-2} \\ 1.05 & ;\Delta > 10^{-2}(\text{rough}) \end{cases} \qquad (2.14)$$

Here, Δ is the roughness taken as $\Delta = \delta/D$ where δ is the marine growth given in Table 2.2 and D is the monopile diameter. The wake amplification factor can be estimated from Figure 2.3, where the Keulegan-Carpenter number is given by Equation 2.15.

$$K_C = \frac{\pi H}{D} \qquad (2.15)$$

The inertia coefficient is given by Equation 2.16 [23].

$$C_m = \max\begin{Bmatrix} 2.0 - 0.044\,(K_C - 3) \\ 1.6 - (C_{DS} - 0.65) \end{Bmatrix} \qquad (2.16)$$

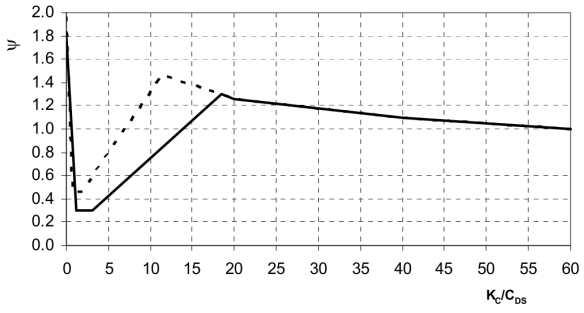

Figure 2.3: Wake amplification factor ψ as function of KC-number for smooth (C_{DS} = 0.65 - solid line) and rough (C_{DS} = 1.05 - dotted line) [23]

The water particle velocity consists of a current and wave component, of which the current component is equal to the current speed given in Table 2.1. These components are factored with a blockage (γ_b) and spreading (γ_s) factor respectively, as shown in Equation 2.17.

$$v_{total} = v_{current} \cdot \gamma_b + v_{wave} \cdot \gamma_s \qquad (2.17)$$

The wave velocity component is depth dependent as the wave velocities decays with depth. The velocity amplitude in deep waters for a given depth can be found following Equation 2.18 [44].

$$v_{wave} = \zeta \omega e^{kz} \tag{2.18}$$

Where:

ζ = Wave crest height
ω = Wave frequency (found with Equation 2.19)
k = Wave number (found with Equation 2.20)
z = Depth from free surface

$$\omega = \frac{2\pi}{T} \tag{2.19}$$

$$k = \frac{4\pi^2}{gT^2} \tag{2.20}$$

Similar to the vertical wind profile, the current will follow the power-law given by Equation 2.1 with a current shear parameter of $\alpha_c = 1/7$ which is a typical value following DNVGL-RP-C205 [23]. The monopile support structure consists of a single 'leg', resulting in zero blockage and thus a current blockage factor of 1.0. The wave spreading factor is set to 0.85, which is the average of appropriate wave spreading factors for the northern North Sea [83]. The current forces act from still water level, which is defined as LAT + tidal ranges and storm surges, whereas the wave forces act from still water level + crest height. The wave kinematics are stretched beyond the still water level using the Wheeler stretching [23].

To acquire the wave particle acceleration, the time derivative of the particle velocity is taken. As the current is considered constant over time, the acceleration will be a function of the wave velocity only. The particle acceleration amplitude can be found following Equation 2.21.

$$\dot{v} = \zeta \omega^2 e^{kz} \cdot \gamma_s \tag{2.21}$$

Figure 2.4 shows an example of the hydrodynamic forcing over the depth of the support structure for the power production and parked conditions in 60 meter water depth. It shows that the forcing is predominantly inertia driven for both situations. This means that the impact of the current and wave velocities is very small compared to the acceleration of the water particles resulting from the wave forcing.

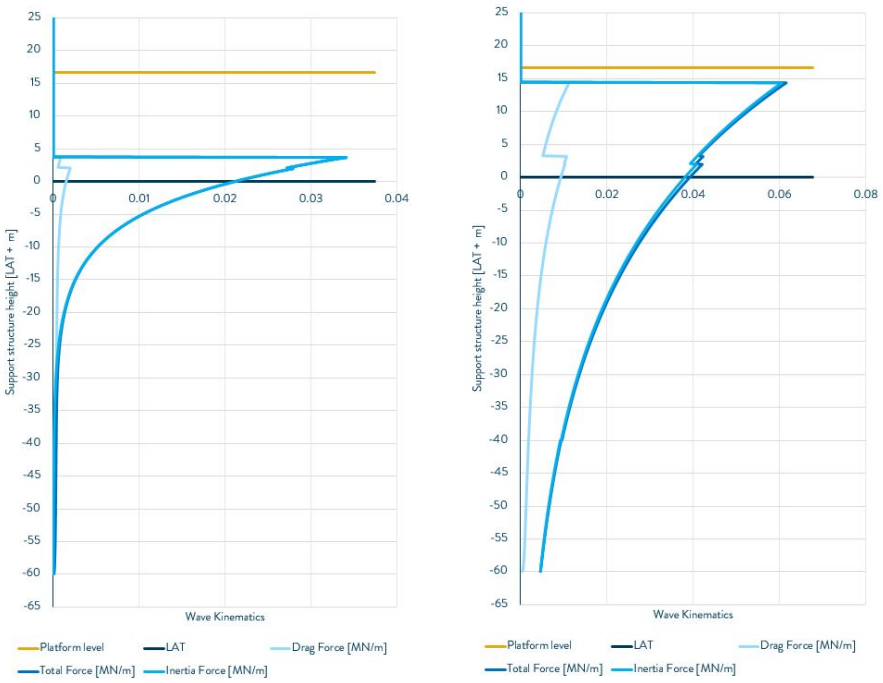

(a) Power Production (b) Parked

Figure 2.4: Hydrodynamic forcing amplitude over the depth

2.3. Load Cases

The dynamics of the wind turbine differ for power production and parked conditions. Hence, both cases should be assessed in order to find the critical load combination. The requirements of several design load cases (DLCs) are listed in DNVGL-ST-0437 [25]. The following subsections will elaborate on which DLCs are assessed for the power production and parked conditions and discusses assumptions.

2.3.1. Power Production Load Case

The turbine will be in 'power production mode' between the cut-in and cut-out wind speed and will deliver its full power potential between the rated and cut-out wind speed shown by the purple line in Figure 2.5. *Note: operational range of modern offshore wind turbines may extend to 30 m/s average wind speeds; this will however not affect the maximum resulting thrust force.*

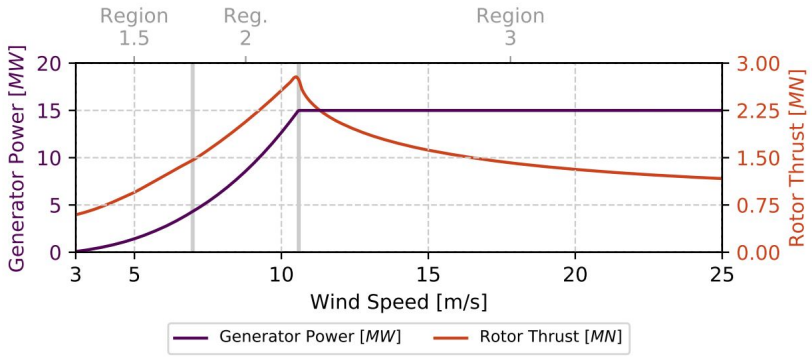

Figure 2.5: Power and thrust curve

In order to accomplish this, the turbine controller must adjust the pitch angle for Region 1.5 and 3 and generator torque for Region 2 of the blades for varying wind speeds. Figure 2.6 shows the blade pitch angle and corresponding rotor speed, torque moment and tip speed ratio (TSR).

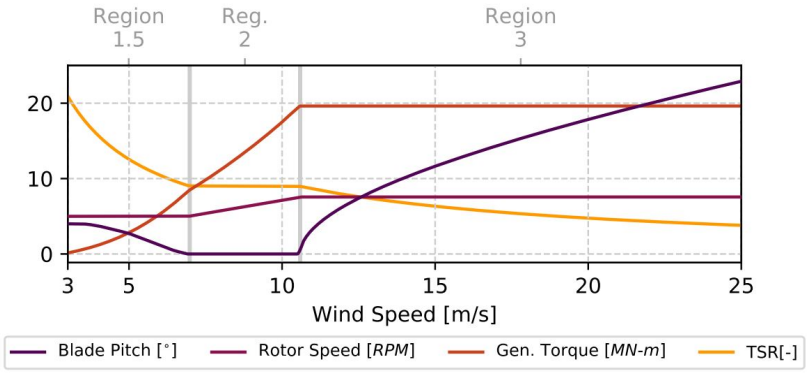

Figure 2.6: Controller regulation trajectory

The performance characteristics of the wind turbine are given by its power (C_P) and thrust (C_T) coefficients. The power coefficient represents the power output resulting from the energy taken from the wind and the thrust coefficient accounts for the developed thrust force on the rotor blades. The controller of the wind turbine pitches the blades for varying wind speeds to achieve optimal efficiency. Until the wind speed reaches its rated value and the blades rotate at their nominal RPM, the blades are fixed in such an angle that they produce maximum lift while staying below the operational limits (e.g. maximum RPM and power) of the WTG. With further increasing wind speed, blade pitch is adjusted to regulate the RPM and thrust force taken from the wind in order to limit power to the rated power of the generator.

Figure 2.7 shows the power coefficient and thrust coefficient for increasing wind speed. As shown in Figure 2.5 the thrust force reaches its maximum value at the rated wind speed. For this optimization model DNVGL's DLC 2.3 is adopted [5, 25], which assesses the forcing under rated wind speed and an extreme operating gust. The system will not be able to react to the gust due to external or internal electrical faults. The adopted hydro data under rated wind speeds is given in Table 2.1 and the rotor drag force is considered negligible during rated conditions.

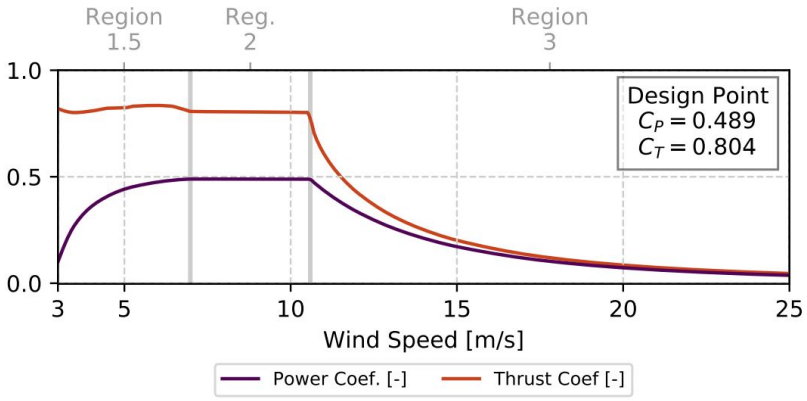

Figure 2.7: Aerodynamic performance coefficients

2.3.2. Parked Condition Load Case

When wind speeds at the hub height exceed the cut-out wind speed of the wind turbine, the power production stops and the system pitches the blades to feather to minimize their forcing. This situation is called 'the parked condition'. For this study the optimization process is conducted for DLC 6.2 [25]. This load case states that the parked turbine should be loaded by 50-year return period wind and wave conditions, while accounting for yaw misalignment of the nacelle. The DLC states that one should assess ±180° yaw misalignment. As the drag force calculation would require simulation software, for this study only 0° and 90° yaw misalignment are assessed. These are the cases where either the blades or the nacelle feel the largest drag force.

When the power production stops, the thrust force becomes zero leaving only the drag force as wind loading. This drag force is not the same for the two yaw misalignment configurations as the loading surface (A_w in Equation 2.9) of the rotor and nacelle varies. When the misalignment is zero, the wind loading surface of the nacelle is equal to the power production situation. When the wind hits the nacelle from the front, the resulting loading surface is: $A_{w;nacelle} = H_{nacelle} \cdot W_{nacelle} = 104 m^2$. When the misalignment is 90° this area becomes $A_{w;nacelle} = H_{nacelle} \cdot L_{nacelle} = 124.8 m^2$. The loading surface and corresponding drag coefficient for the blades is defined with respect to their chord length [41]. The chord length over the blade length is shown in Figure 2.8. For this analysis the average chord length depicted with the red dashed line of 3.46 meters is adopted, resulting in a loading surface of $A_{w;blade} = c_{av} \cdot L_{blade} = 404.82 m^2$. The model accounts for three blades when the wind hits from the front and for two blades when the wind hits from the side to account for the blockage caused by the blades.

Figure 2.9 shows drag versus lift coefficients for different types of airfoil families. All of these families are represented in the varying cross sectional geometry of the blade. As shown in the figure, all families show relatively similar behaviour apart from the SNL-FFA-W3-500. This line represents a relatively thicker airfoil shape, which is represented close to the blade root and accounts for a relatively small part of the blade. During parked conditions the blades will pitch such that the lift coefficient converges to zero. The figure shows that for a lift coefficient of zero the drag coefficient is approximately 0.01 to 0.018. For this study a frontal rotor drag coefficient of 0.018 is selected. The side rotor drag coefficient is estimated to be equal to the square drag coefficient of 1.00 due to its flat shape.

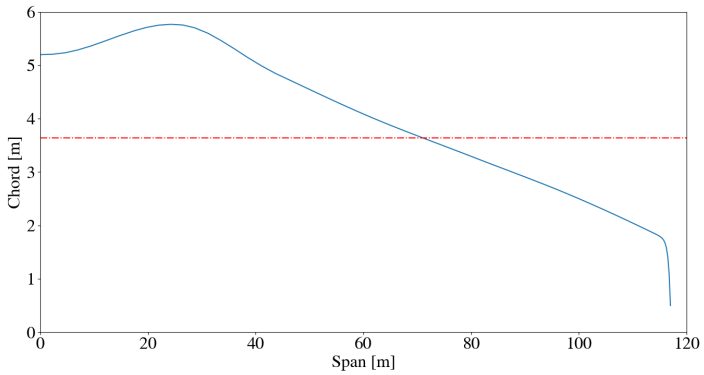

Figure 2.8: Chord Length over Blade Span

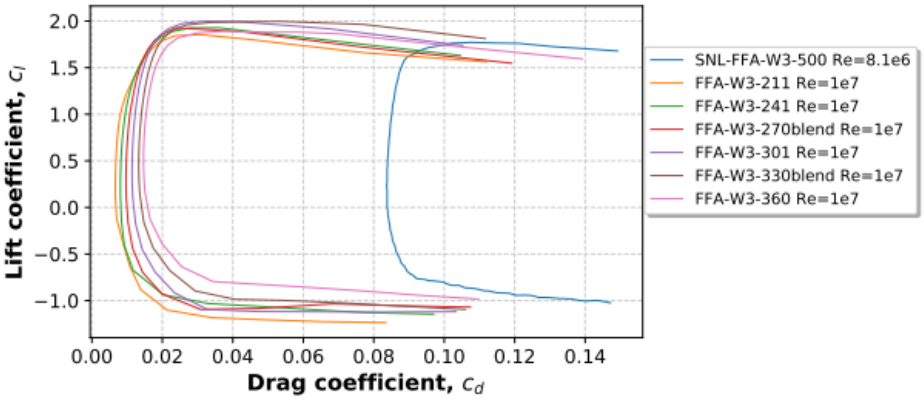

Figure 2.9: Airfoil family drag coefficients

2.4. Monopile Design Criteria

In consultation with monopile manufacturer Sif Group a number of manufacturability, installability or operationability driven design criteria are established to ensure that the design configurations represent realistic models [51]. With eye on the future, the limitations take into account expected developments in installation and production technologies. For this reason, the boundaries may exceed current state-of-art [51], taking into account already foreseen developments in installation and production technologies. A summary of the design criteria is given below, with more detail on the parameters provided in the next paragraphs.:

1. Outer diameter between 10 and 14.5 m
2. Maximum D/t ratio of 160
3. Maximum wall thickness of 150 mm
4. Taper angle of cans ≤ 4.5°
5. Platform unsubmerged at all times

2.4.1. Manufacturability

A relatively cost effective production method for the steel cans required in the monopiles is the use of so called "thermo-mechanical control processed" (TMCP) steel. Sif Group stated that the industry is expected to be able to deliver TMCP steel plates with a maximum wall thickness of 150 mm and that they will be able to produce cans with a maximum diameter of 14.5 m [51]. If the wall thickness exceeds this value, the production method switches to the quench & temper process, which is approximately twice as expensive as TMCP and has a longer delivery time. Hence, for this optimization process a wall thickness manufacturability limit of 150 mm and outer diameter limit of 14.5 m are set.

With the increasing diameter of the steel cans, the steel cans become more slender. The slenderness of the cans is defined by the outer diameter over wall thickness ratio (D/t ratio). The more slender the steel cans, the higher the local bending and hoop stresses will become [77]. This will cause the cans to be more flexible and increasingly hard to handle. An increasing D/t ratio will also enlarge the risks of local buckling during installation. Additionally, transportation and storage will become a difficult topic for very large slender cans. In consultation with Sif Group, the slenderness limit of the cans was set to a D/t ratio of 160. This limit is verified by large contractors such as Orsted and is confirmed by industry practice [28, 51].

2.4.2. Installability

When the monopile fabrication is finished, they need to be installed offshore. This is typically done by hammering the piles in to the soil until they reach an embedded length that provides sufficient stability for the wind turbine. The required embedded depth varies strongly with soil type and is a topic under extensive research. For each project an individual soil and foundation analysis is required for each individual location to acquire the appropriate embedded lengths. The adopted pile length for this is discussed in Section 3.1.1.

In order to ensure stability, the base diameter of a monopile typically needs to be larger than the base diameter of the wind turbine towewr. Thus, in order to connect the two components a tapered section is required. When hammering the piles, great vertical force is transferred through the monopile. If the taper angle of this section is too high the section will start to function as a damper, which would result in significant stress concentrations and possibly failure of installation. As the production of tapered cans is more expensive than the production of straight cans, the number of tapered cans should be minimized [51]. The taper angle is set to 4.5° in consultation with Sif Group; this is the maximum allowable taper angle to ensure installability [51].

2.4.3. Operationability

Another important geometry criteria is the interface level, which is assumed to be the top level/start of the monopile for this research. The fluctuations in water levels and waves will cause a constantly changing waterline. The interface level should be set such that the platform interface will never be hit by waves [24]. This level can be found using Equation 2.22.

$$z_i = LAT + \Delta_{WL} + \zeta^* + \Delta z_{air} \tag{2.22}$$

Δ_{WL} = Water level including tidal range and storm surge
ζ^* = 50-year highest wave elevation above still water level
Δz_{air} = Air gap max$[0.2H_{s;50}, 1.0m]$

Where $H_{s;50}$ is the 50-year return period significant wave height.

3

Monopile Design Optimization Process

Now that the environmental forcing and monopile design criteria are known, monopile geometries need to be defined for the target depth range of 60 to 120 meters. In order to optimize these geometries a parametric model is established, which is presented in Section 3.1 and a flowchart of the optimization process is shown in Appendix A. A summary of the steps of the process is listed below:

1. The monopile's first natural frequency is calculated and has to match the set target frequency. The calculation of the natural frequency is given in Section 3.1.1.
2. If the monopile geometry yields the target first natural frequency, it will first be tested on its ultimate limit state (ULS) capacities and altered accordingly (if possible and necessary). The ULS check consists of a yield stress and global buckling check, given in Section 4.1 and 4.3. The yielding check is done over the entire structure length up to the virtual fixation point which is located 1 times the outer diameter below the mudline [39]. Standards state that a local buckling check is also required [24]. However, as this check requires more detailed design, it is not conducted in this study
3. The water depth - target frequency configurations that are resistant against the ULS will be checked on fatigue life, as explained in Chapter 5.

3.1. Model Explanation

The monopile optimization model is set-up using Excel as main platform with added macros for optimization. User-defined load cases and wind turbine data are inserted with the parameters given in Table 1.1 and 2.1. For this research the support sturcture is checked under rated and 50 year return load cases.

For the monopile geometry optimization process the complete wind turbine, from the sub-soil virtual fixation point (1D below the seabed) to the hub, is subdivided into cans with a height of 4 meters. For each of these cans the bottom diameter and wall thickness are variable. If a can is tapered, it is done in such fashion that their top outer diameter matches the bottom diameter of the subsequent upper can, ensuring a flush exterior. The turbine tower optimization is not included in this research and the reference turbine tower geometry is adopted [34]. The design of this tower is not substantially different from common practice in offshore support structure design [72] The optimization process is done under a number of geometry criteria listed in Section 2.4.

The geometry optimization process is visualized in Figure 3.1. The initial input geometry extends the base diameter of the turbine tower (10 m) to the mudline. The substructure will have an initial D/t ratio of 160 (*Step 1*). When this initial input geometry doesn't pass the conducted checks, the diameter will be increased from the slender top part (L_{top}) downwards under a taper angle of 4.5° until it reaches the set base diameter. The initial value of L_{top} is set to 40 m below LAT, beyond this depths the slender top part will fail the yield check for the D/t ratio of 160 (*Step 2*). If the current geometry doesn't yield a satisfactory geometry, the length of the slender top part can be decreased and the wall thickness can be increased to stiffen the system (*Step 3*). A more elaborate explanation of the optimization process is given in Section 3.1.2.

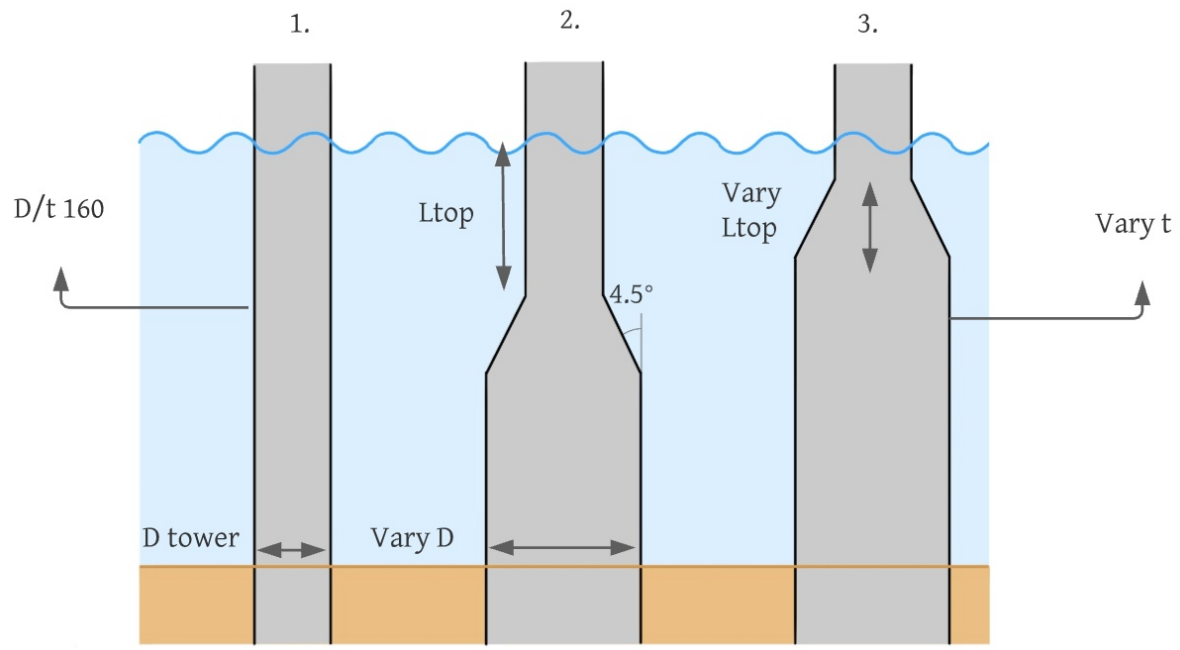

Figure 3.1: Geometry Optimization Process

3.1.1. Natural Frequency Selection and Calculation

An important parameter in the design of an offshore wind turbine foundation is the selected target first natural frequency of the system (f_t). When the system is dynamically loaded at or around this first natural frequency, the structural reaction is amplified which can result in significant damage. To avoid this interaction, it is common practice to target the f_t away from the forcing frequencies. The dynamic forces considered in this study are the wind, wave and rotor forces.

To assess the spectral power density for the frequency of the wind forcing, the Kaimal spectrum is used [47]. For the wave frequencies the JONSWAP spectrum is adopted [20]. As the open sea location of Buchan deep is likely to be subjected to a combination of wind and swell waves, a detailed design should include spectra accounting for these types of waves such as the twin-peaked Torsethaugen spectrum [54]. However, since swell waves typically have a larger period than wind waves, the excitation frequency will be lower and will not interfere with the structure frequency. Therefore, for this study the swell waves are neglected during the target frequency selection. The rotor forcing frequencies consist of the rotational frequency of the rotor during power production (1P) and the blade passing frequency (3P). The rotational frequency varies between the minimum and maximum rotor speed given in Table 1.1 and the blade passing frequency is thrice this value.

Figure 3.2 shows all forcing components over a range of exciting frequencies. It is common practice to set the target frequency between the 1P and 3P zones. However, the figure shows that this would result in significant interference with the wave frequencies. To assess the effect of the chosen natural frequency on the monopile geometry for large turbines such as considered in this research, a range of target frequencies is selected. For this study target frequencies of 0.15, 0.17 and 0.20 Hz are assessed, which all fall in the desired frequency range. The 0.15 Hz target was chosen after consultation with Marc Seidel, a Siemens Gamesa expert, based on current 14 MW designs in shallower waters [71]. The 0.17 Hz target frequency was stated in the reference data [34]. The 0.20 Hz target frequency was added to give insight in how the selection of stiffer target natural frequency impacts the technical boundaries of the monopile foundation. Due to the interference with the wave energy spectrum, dynamic simulations are required to assess the consequences of the dynamic loading such as fatigue damage.

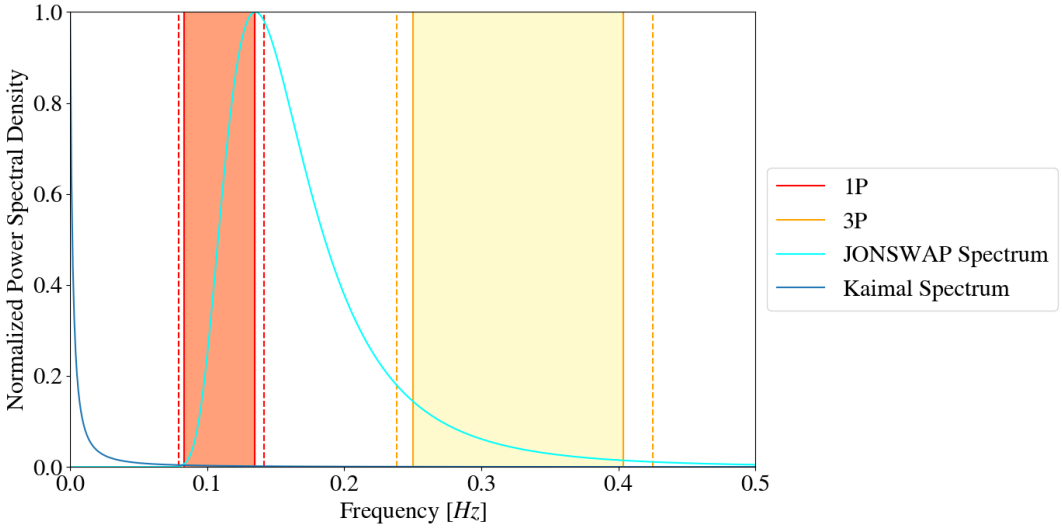

Figure 3.2: Frequency Diagram

The first natural frequency of a tower with varying diameter can be approximated by an analytic expression following the Rayleigh method factored by suitable design coefficients given by Equation 3.1 [5].

$$f_n = C_L C_R C_S f_{FB} \tag{3.1}$$

Where:

C_S = Substructure flexibility coefficient
C_L = Lateral foundation flexibility coefficient
C_R = Rotational foundation flexibility coefficient
f_{FB} = Fixed base first natural frequency

The fixed base natural period can be estimated with the analytical expression given in Equation 3.2 from which the natural frequency can be found ($f_{FB} = 1/T_n$) [42].

$$T_n^2 = \frac{4\pi^2 \left(m_{top} + m_{eq} L\right) L^3}{3 E I_{eq}} \cdot \left[\frac{48}{\pi^4}\right] \tag{3.2}$$

Where:

I_{eq} = Equivalent moment of inertia
E = Elasticity modulus steel (210 GPa)
m_{eq} = Equivalent mass per unit length
L = Total length of the system

In order to calculate the required parameters for the natural frequency calculation, the system is subdivided in to segments of 0.10 m height. The final parameters are found following Equations 3.3 and 3.4.

$$I_{eq} = \frac{\sum_{j=1}^{n} I_j l_j \cos^2\left(\frac{\pi x_j}{2L}\right)}{L} \tag{3.3}$$

$$m_{eq} = \frac{\sum_{j=1}^{n} m_j l_j \left(1 - \cos\left(\frac{\pi x_j}{2L}\right)\right)^2}{L} \tag{3.4}$$

Where:

I_j = Moment of inertia of segment j $[m^4]$
m_j = Distributed mass of segment j $[kg/m]$
l_j = Segment height $[m]$
x_j = Distance to mudline of segment j $[m]$

The substructure flexibility coefficient, C_S, is calculated using the monopile length from interface height to mudline (L_S). The substructure flexibility is expressed in terms of two dimensionless parameters, the bending stiffness ratio $\chi = EI_T/EI_P$ (where EI_T is the tower stiffness and EI_P the monopile stiffness) and the length ratio $\phi = L_S/L$. The substructure flexibility coefficient can hereafter be calculated following Equation 3.5.

$$C_S = \sqrt{\frac{1}{1+(1+\phi)^3\chi-\chi}} \tag{3.5}$$

The rotational and lateral foundation flexibility coefficients account for the foundation stiffness and are estimated following Poulos & Davis [65]. The soil data report of the reference site shows that the soil consists of a variety of soil types varying from pure sand to sandy clay [76]. For this analysis it is assumed that the full penetration depth consists of the same soil type. To assess the effect of the soil type on the monopile geometry separate designs for loose and dense sand with a respective horizontal coefficient of sub-grade reaction (n_h) of 2.8 and 70 MN/m^3 are made [5]. The foundation flexibility coefficient are calculated following Equations 3.6 and 3.7.

$$C_R = 1 - \frac{1}{1+0.6\left(\eta_R - \frac{\eta_{LR}^2}{\eta_L}\right)} \tag{3.6}$$

$$C_L = 1 - \frac{1}{1+0.5\left(\eta_L - \frac{\eta_{LR}^2}{\eta_R}\right)} \tag{3.7}$$

Where η_R, η_{LR} and η_L are non-dimensional stiffnesses which can be calculated following Equations 3.8, 3.9 and 3.10 respectively [65].

$$\eta_R = \frac{K_R L}{EI_{eq}} \tag{3.8}$$

$$\eta_{LR} = \frac{K_{LR} L^2}{EI_{eq}} \tag{3.9}$$

$$\eta_L = \frac{K_L L^3}{EI_{eq}} \tag{3.10}$$

To solve the equations, the soil dependent foundation stiffness K_R, K_{LR} and K_L are required, which, for slender piles in linear inhomogenous soils can be calculated following Equations 3.12, 3.13 and 3.14 [65]. L_P is the embedded length, which can be estimated by Equation 3.11 [65]. The validity of this embedded length estimation is assessed in Section 4.2.

$$L_P = 4.0\left(\frac{E_P I_P}{n_h}\right)^{\frac{1}{5}} \tag{3.11}$$

$$K_R = 1.48 n_h^{\frac{1}{5}} (E_P I_P)^{\frac{4}{5}} \tag{3.12}$$

$$K_{LR} = -0.99 n_h^{\frac{2}{5}} (E_P I_P)^{\frac{3}{5}} \tag{3.13}$$

$$K_L = 1.074 n_h^{\frac{3}{5}} (E_P I_P)^{\frac{2}{5}} \tag{3.14}$$

In order to validate the analytical natural frequency calculation, the provided tower geometry [34] and a selection of monopile geometries are modeled (an example is shown in Figure 3.3) in Ansys. A modal analysis is performed to obtain the first natural frequency. The resulting natural frequencies showed a maximum difference of 5% in first natural frequency, which is considered satisfactory for the present study.

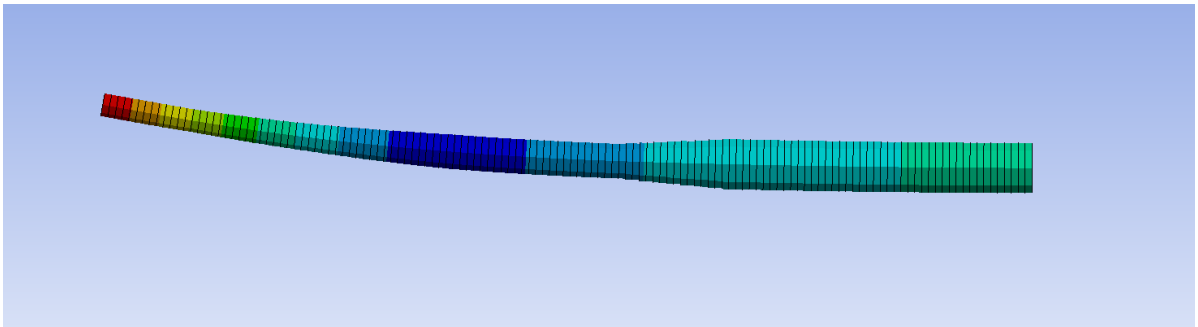

Figure 3.3: Ansys Modal Analysis First Bending Mode

3.1.2. Monopile Design Optimization Process

With all the data and structural integrity checks set, they can be combined in order to find optimized monopile geometries. The optimization is an iterative process of which an overview is given in the form of a flowchart in Appendix A. As a first step, the environmental and wind turbine data are entered and a design water depth and target first natural frequency are chosen. For this study water depths of 60, 80, 100 and 120 meters and target frequencies of 0.15, 0.17 and 0.20 Hz are assessed. To assess the effect of different soil types, the optimization is done for very loose and dense soil types. Hereafter, an initial monopile geometry is fed to the model, this initial geometry extends the 10 meter tower bottom diameter over the entire length of the monopile under a D/t ratio of 160. It is assumed that the monopile will never have a smaller diameter than the bottom of the tower.

Firstly, the first natural frequency is checked. If it is within ±0.02 Hz of the target frequency the frequency is considered accurate enough. When the deviation is larger than ±0.02 Hz, the geometry should be altered to converge the natural frequency to the desired target frequency. The first natural frequency can be changed by varying the base diameter, wall thicknesses and length of the slender top part of the monopile (L_{top}). To minimize the monopile mass, the method with the most effect per extra steel usage should be conducted first. For the proposed monopile geometry, this is empirically found to be the change in base diameter, followed by the variation in L_{top} and lastly the variation of wall thickness. The variation of wall thickness may, however, be required to pass the unity checks. The diameter will be increased or decreased, depending on the natural frequency, with steps of 0.1 m. When the diameter is varied it is also checked whether variation of L_{top} yields an acceptable geometry. If not, the process is repeated until the frequency of the structure is within ±0.02 Hz of the target frequency. If the target frequency cannot be found for a diameter between 10 and 14.5 meters, the optimization stops and no geometry that passes the criteria is found.

When the natural frequency check is passed, the current structure is checked on yield stress capacity for both load cases as explained in Section 4.1. If the check is not passed over the entire structure, the wall thickness of the failed cans is increased with steps of 1 mm. After every step, it is checked whether the natural frequency is still within the allowed margins.

If the yield check is passed, a global buckling check is conducted for the optimized geometry of the monopile as explained in Section 4.3. If this check is not passed, it is assumed that no optimized geometry can be found for the selected combination of water depth and target frequency.

When the geometry passes both ultimate limit state checks, the geometry will be tested on fatigue resistance. The fatigue analysis is explained in Chapter 5.

4

Ultimate Limit State Check

The monopile geometries will be tested and optimized according to two ultimate limit state (ULS) checks. The first one being the Von Mises stress unity check and the second one is a global buckling check [24]. DNV standards dictate the requirement of local buckling checks as well. However, these require more detailed designs and are therefore not included in the geometry optimization process. This Chapter will elaborate on both conducted checks in Section 4.1 and 4.3. Hereafter, the results will be presented and conclusion will be made accordingly in Section 4.4.

4.1. Von Mises Stress Unity Check

The first conducted check is the Von Mises stress unity check [24]. In this check the occurring stresses in the monopile will be tested against the yield strength of the used steel. The Von Mises stress is a combination of stresses resulting from axial forces, shear forces and overturning moment and is found with Equation 4.1 [19].

$$\sigma_{vm} = \sqrt{\sigma_x^2 - \sigma_x \sigma_y + \sigma_y^2 + 3\tau_{xy}^2} \tag{4.1}$$

When the loading is a combination of only longitudinal and shear stress (present in the current design), Equation 4.1 can be simplified to Equation 4.2.

$$\sigma_{vm} = \sqrt{\sigma_x^2 + 3\tau_{xy}^2} \tag{4.2}$$

Here, the axial stress (σ_x) consists of a normal force component and an overturning moment component. The normal force component results from the own weight of the top mass, tower and monopile. The overturning moment component is a result of the environmental loading, as given in Chapter 2. The factored axial stress can be found by Equation 4.3.

$$\sigma_x = \frac{V}{A}\gamma_g + \frac{M}{W}\gamma_e \tag{4.3}$$

Where:

V = Total axial force $[N]$
A = Cross section area $[m^2]$
M = Total Moment $[Nm]$
W = Elastic Section Modulus $[m^3]$
γ_g = Safety factor permanent loads (1.10) [25]
γ_e = Safety factor environmental loads (1.35) [25]

The shear stress (τ_{xy}) can be found following Equation 4.4, where F_B is the total shear at the given height.

$$\tau_{xy} = \frac{2F_B}{A}\gamma_e \tag{4.4}$$

Sif Group primarily uses S355ML graded steel for their monopile production [51]. The specified yield stress (f_y) of this material depends on the wall thickness of the plates. The present study uses the values in Table 4.1.

Table 4.1: Specified Yield Strength of S355ML for different wall thicknesses [32]

Wall thickness [mm]	Yield Stress [MPa]
3 - 16	355
16 - 40	345
40 - 63	335
63 - 100	325
100 - 150	295

Combining the above equations, the monopile geometry is checked on the final Von Mises stress unity check per 0.1 m height segment. The final Von Mises stress unity check reads as stated in Equation 4.5 with an additional overall safety factor set at 0.9 [69]. A material safety factor (γ_m) of 1.10 is applied [43].

$$\frac{\sigma_{vm}}{f_y/\gamma_m} \leq 0.9 \tag{4.5}$$

In order to find the forces and overturning moment along the structure for the yield stress check, the monopile is modeled as a cantilever beam. Due to the soil-type dependent flexibility of the foundation under the mudline, the location of the maximum stress varies per monopile geometry and soil type. A simplified analytical model is established in Maple to assess this effect for the range of soil type adopted for this study (loose to dense sand) of which a visualization is shown in Figure 4.1. For convenience a set of notations is introduced for the horizontal displacement of the different sub-sections ($u_{1,2,3,4}$), where the subscripts refer to the segment numbering in the figure.

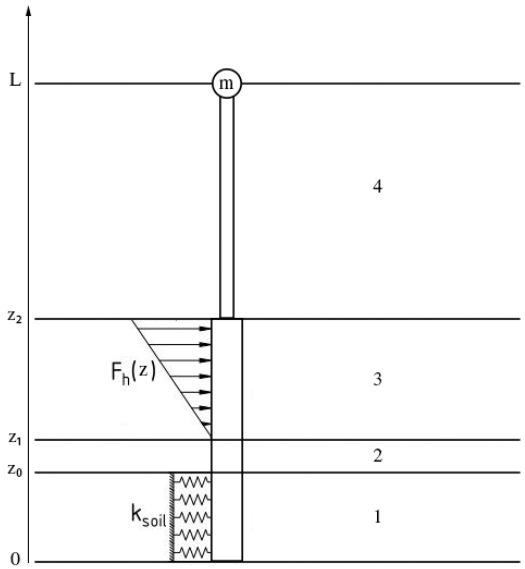

Figure 4.1: Simplified wave forcing model

Using the above notation, equations of motion for the system can be written as Equation 4.6 following the Euler-Bernoulli beam theory. In order to achieve general insight on the reaction of the pile below the mudline without over-complicating the model, only the reaction to the main force contributor is assessed. The main stress contributor in the ULS check is the wave forcing during 50 year return conditions. Soil is considered a highly non-linear factor in the foundation design. Not only does the soil- type and reaction vary over the pile penetration depth, The reaction of the soil also varies per load rate and can change over time. Hence, no general conclusion can be made on the soil behavior and a separate soil analysis must be made for every monopile. To simplify the analysis the soil stiffness is considered to be constant over depth in this model,

however a complete range of stiffnesses representative for different, soil types will be used in the analysis to obtain a good impression of the impact of soil on the overall design. f_h is the wave force at z_2 from which the forcing is assumed to decline linearly downwards and k_{soil} is the soil stiffness.

$$\begin{aligned} EI_1\frac{\partial^4 u_1}{\partial z^4} + m_1 g\frac{\partial^2 u_1}{\partial z^2} + k_{soil}u_1 &= 0 && 0 \le z \le z_0 \\ EI_1\frac{\partial^4 u_2}{\partial z^4} + m_2 g\frac{\partial^2 u_2}{\partial z^2} &= 0 && z_0 \le z \le z_1 \\ EI_1\frac{\partial^4 u_3}{\partial z^4} + m_3 g\frac{\partial^2 u_3}{\partial z^2} &= f_h\frac{z-z_1}{z_2-z_1} && z_1 \le z \le z_2 \\ EI_2\frac{\partial^4 u_4}{\partial z^4} + m_4 g\frac{\partial^2 u_4}{\partial z^2} &= 0 && z_2 \le z \le L \end{aligned} \tag{4.6}$$

The vertical location of z_0, z_1, z_2 and therefore the total length of the system depend on the specific geometry and soil type selection. z_0 is equal to the pile penetration depth and is estimated by Equation 3.11. z_2 is the location where the wave forcing is maximum, which is equal to $L - z_{hub} + \Delta d_{waterline} + H_{max}/2$. The location of z_1 determines the total magnitude of the triangular wave forcing. In order to stay close to the forcing resulting from the exponentially decaying wave forcing (Airy wave theorem as stated in Chapter 2), the overturning moment resulting from the triangular forcing at the mudline should be equal to the overturning moment resulting from the exponential forcing. Typically, using exponentially decaying wave forcing, the contribution of forcing below half times the wave length can be considered negligible [44]. To find an equivalent penetration depth for the triangular forcing to the exponential forcing, both resulting moments can be described as:

$$M_{exp} = \int_{z_2-\frac{\lambda}{2}}^{z_2} f_h^{-k(z_2-z)}(z-z_0)dz \tag{4.7}$$

$$M_{triang} = \int_{z_2-\frac{\lambda}{\lambda_{eq}}}^{z_2} f_h\frac{z-(z_2-\frac{\lambda}{\lambda_{eq}})}{z_2-(z_2-\frac{\lambda}{\lambda_{eq}})}(z-z_0)dz \tag{4.8}$$

The above system can be solved for λ_{eq}, which can be used to find z_1 using Equation 4.9

$$z_1 = z_2 - \frac{\lambda}{\lambda_{eq}} \tag{4.9}$$

Figure 4.2 shows both forcing types over structure length from an arbitrary z_0 to z_2.

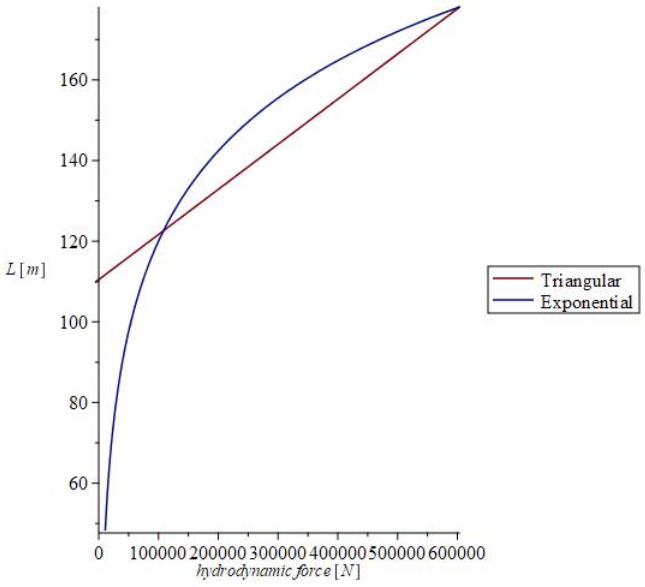

Figure 4.2: Comparison of exponential and equivalent triangular

The boundary conditions (4 in total) at the pile tip ($z = 0$) and hub height ($z = L$) are given in Equation 4.10. The pile tip is sufficiently deep to resist all acting loads; please also refer to Section 4.2.

$$\left.\frac{\partial^2 u_{1,4}}{\partial z^2}\right|_{z=0,L} = \left.\frac{\partial^3 u_{1,4}}{\partial z^3}\right|_{z=0,L} = 0 \tag{4.10}$$

and the interface conditions (3 time 4) are given by:

$$\begin{aligned} u_{1,2,3}(z_{0,1,2}) &= u_{2,3,4}(z_{0,1,2}) \\ \left.\frac{\partial u_{1,2,3}}{\partial z}\right|_{z=z_{0,1,2}} &= \left.\frac{\partial u_{2,3,4}}{\partial z}\right|_{z=z_{0,1,2}} \\ \left.\frac{\partial^2 u_{1,2,3}}{\partial z^2}\right|_{z=z_{0,1,2}} &= \left.\frac{\partial^2 u_{2,3,4}}{\partial z^2}\right|_{z=z_{0,1,2}} \\ \left.\frac{\partial^3 u_{1,2,3}}{\partial z^3}\right|_{z=z_{0,1,2}} &= \left.\frac{\partial^3 u_{2,3,4}}{\partial z^3}\right|_{z=z_{0,1,2}} \end{aligned} \tag{4.11}$$

To solve the boundary-value problem above, a general solution to the ordinary differential equations has to be established for all segments. This general solution is hereafter substituted in the system in order to find the behavior of the system.

The system has a unique solution for every segment, the segment numbering is visualized in Figure 4.1. As Segment 2 and 4 are not externally forced, their general solution only consists of a homogeneous part described by Equation 4.12 for $n = 2, 4$:

$$u_n(z) = A_n + B_n z + C_n \sin\left(\sqrt{\frac{mg}{EI_n}}z\right) + D_n \cos\left(\sqrt{\frac{mg}{EI_n}}z\right) \tag{4.12}$$

The equation of motion for Segment 1, which is the subsoil segment, can be rewritten as Equation 4.13. Here, $\alpha = \frac{mg}{EI_1}$ and $\beta = \frac{k_{soil}}{EI_1}$.

$$\frac{d^4 u(z)}{dz^4} + \alpha^2 \frac{d^2 u(z)}{dz^2} + \beta u(z) = 0 \tag{4.13}$$

The solution to this 4th order differential equation can be found in the following form:

$$u(z) = \sum_{n=1}^{4} C_n e^{i\lambda_n z} \tag{4.14}$$

for which the characteristic equation is defined and the eigenvalue problem is solved

$$\lambda^4 + \alpha^2 \lambda^2 + \beta = 0 \tag{4.15}$$

$$\lambda_1 = \sqrt{\frac{-m_1 g + \sqrt{m_1^2 g^2 - 4k_{soil} EI_1}}{2EI_1}}, \lambda_2 = \sqrt{\frac{-m_1 g - \sqrt{m_1^2 g^2 - 4k_{soil} EI_1}}{2EI_1}} \tag{4.16}$$

The solution for Segment 1 is now found and can be rewritten as Equation 4.17

$$u_1(z) = A_1 e^{(\lambda_1 z)} + B_1 e^{(-\lambda_1 z)} + C_1 e^{(\lambda_2 z)} + D_1 e^{(-\lambda_2 z)} \tag{4.17}$$

The general solution for Segment 3 consists of a homogeneous and particular solution, of which the homogeneous part is equal to the homogeneous solutions of Segment 2 and 4. To find the particular solution, the forcing can be rewritten as follows:

$$f_h \frac{z - z_1}{z_2 - z_1} = \frac{f_h}{z_2 - z_1} z - \frac{f_h z_1}{z_2 - z_1} = Az + B \tag{4.18}$$

In order to obtain the unique terms of the particular solution, a solution of the following form is substituted in the differential equation:

$$u_{3,\,\text{part}}(z) = (rz + s)z^2 \tag{4.19}$$

which results in the following system that can be solved for r and s:

$$6mgrz + 2mgs = Az + B \tag{4.20}$$

$$r = \frac{A}{6m_3g} \quad \text{and} \quad s = \frac{B}{2m_3g} \tag{4.21}$$

A and B can be found from Equation 4.18 and are $\frac{f_h}{z_2-z_1}$ and $-\frac{f_h z_1}{z_2-z_1}$ respectively
Combining the homogeneous and particular part, the solution for Segment 3 is given by:

$$u_3(z) = A_3 + B_3 z + C_3 \sin\left(\sqrt{\frac{m_3 g}{EI_1}}z\right) + D_3 \cos\left(\sqrt{\frac{m_3 g}{EI_1}}z\right) - \left(\frac{f_h z}{6(z_2-z_1)m_3 g} - \frac{f_h z_1}{2(z_2-z_1)m_3 g}\right)z^2 \tag{4.22}$$

With the full system solved, the effect of varying the soil stiffness can be assessed. The general solutions for the displacement of all segments are summarized below:

$$u(z) = \begin{cases} u_1(z) = A_1 e^{(\lambda_1 z)} + B_1 e^{(-\lambda_1 z)} + C_1 e^{(\lambda_2 z)} + D_1 e^{(-\lambda_2 z)}, \text{ for } 0 < z < z_0 \\ u_2(z) = A_2 + B_2 z + C_2 \sin\left(\sqrt{\frac{m_2 g}{EI_1}}z\right) + D_2 \cos\left(\sqrt{\frac{m_2 g}{EI_1}}z\right), \text{ for } z_0 < z < z_1 \\ u_3(z) = A_3 + B_3 z + C_3 \sin\left(\sqrt{\frac{m_3 g}{EI_1}}z\right) + D_3 \cos\left(\sqrt{\frac{m_3 g}{EI_1}}z\right) - \left(\frac{f_h z}{6(z_2-z_1)m_3 g} - \frac{f_h z_1}{2(z_2-z_1)m_3 g}\right)z^2, \text{ for } z_1 < z < z_2 \\ u_4(z) = A_4 + B_4 z + C_4 \sin\left(\sqrt{\frac{m_4 g}{EI_2}}z\right) + D_4 \cos\left(\sqrt{\frac{m_4 g}{EI_2}}z\right), \text{ for } z_2 < z < L \end{cases}$$

The successive derivatives of the horizontal deflections have important physical meanings. The bending moment M and shear force Q can be found following Equation 4.23

$$M = -EI\frac{d^2u}{dz^2} \text{ and } Q = -\frac{d}{dz}\left(EI\frac{d^2u}{dz^2}\right) \tag{4.23}$$

To assure that the two-stepped simplified system as visualized in Figure 4.1 shows similar behaviour to the full geometry, the equivalent moment of inertia of the broad and slender part are matched to the equivalent moment of inertia of the full geometry over the same length following Equation 3.3. As a check, the stiffness is set to infinite and the resulting moment at the mudline is compared to the resulting moment of the optimization model. Figure 4.3 shows that the two models show very similar results for the clamped situation (difference of less than 0.5%). Therefore, the Maple model is assumed to be valid to use.

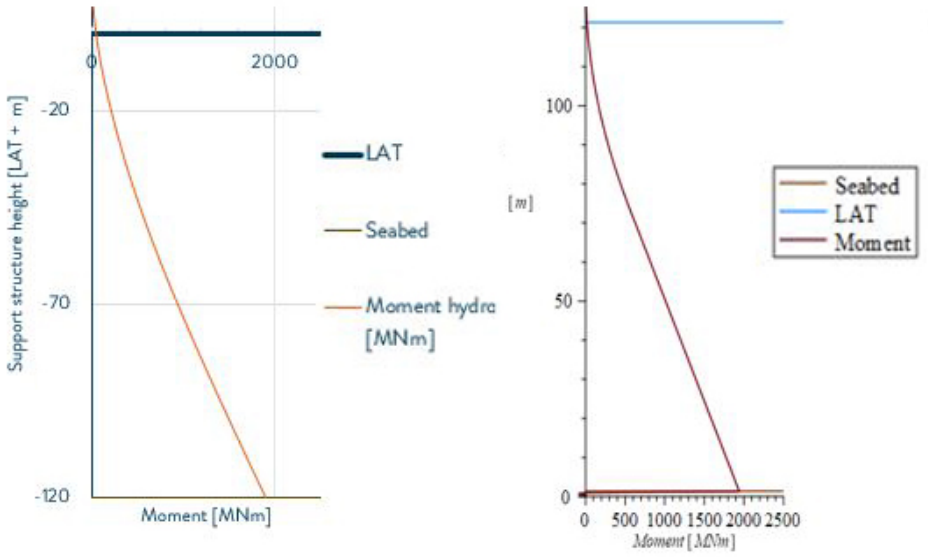

Figure 4.3: Comparison between Excel model (left) and Maple model (right)

4.2. Soil Stiffness Model Validation

To assess the effect of soil stiffness to the displacement and maximum moment, the model is run for a stiffness of $k_{soil} = D \cdot 2.8 \cdot 10^6$ N/m^3 and $D \cdot 70 \cdot 10^6$ N/m^3 representing the loose and dense sand respectively [65].

Figure 4.4 shows the displacement of the monopile and turbine for the same geometry to the ultimate wave height (with the estimated pile length following Equation 3.11). As expected, the displacements will be larger in loose soils and a deeper pile penetration is required. Several design criteria have been proposed for the required embedded length of which three criteria are listed below [22, 50]:

1. Zero toe-kick criterion: the pile length is chosen such that the displacement of the pile toe is zero or negative.
2. Vertical tangent criterion: the pile length is chosen such that the deflection curve has a vertical tangent at the pile toe.
3. Critical pile length criterion: the pile length is chosen such that a further increase in pile length has no (or very limited) effect on the displacements (deflection and rotation) at the pile head. In other words, loosely speaking the depth to which the lateral loads from the pile head are being transferred.

As the estimated pile length complies with all three criteria, the estimated embedded length is assumed to be valid for this analysis. As the soil-pile interaction is a very complex topic, the full interaction between XL monopiles and different soil types over time is a strong recommendation of further research.

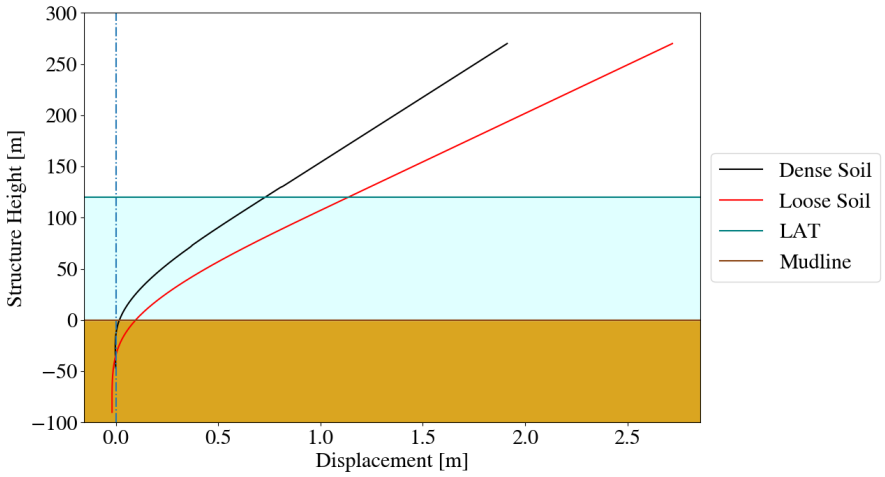

Figure 4.4: Displacement Over the System Length for Loose and Dense Soil

Figure 4.5 shows the resulting overturning moment due to the ultimate wave height along the pile. It shows that the maximum moment magnitude occurs somewhere below the mudline. The magnitudes of the maximum overturning moment is given in Table 4.2. It shows that the maximum value doesn't increase significantly between the soil types or clamped conditions. Therefore, the maximum stress can be assumed independent of the soil type and the moment at 1D below the mudline in clamped conditions is considered a safe assumption.

Table 4.2: Results of simplified ULS wave forcing model

Soil type	Top displacement [m]	Maximum Moment [MNm]
Clamped	1.39	1905
Dense Soil	1.91	1914
Loose Soil	2.72	1945

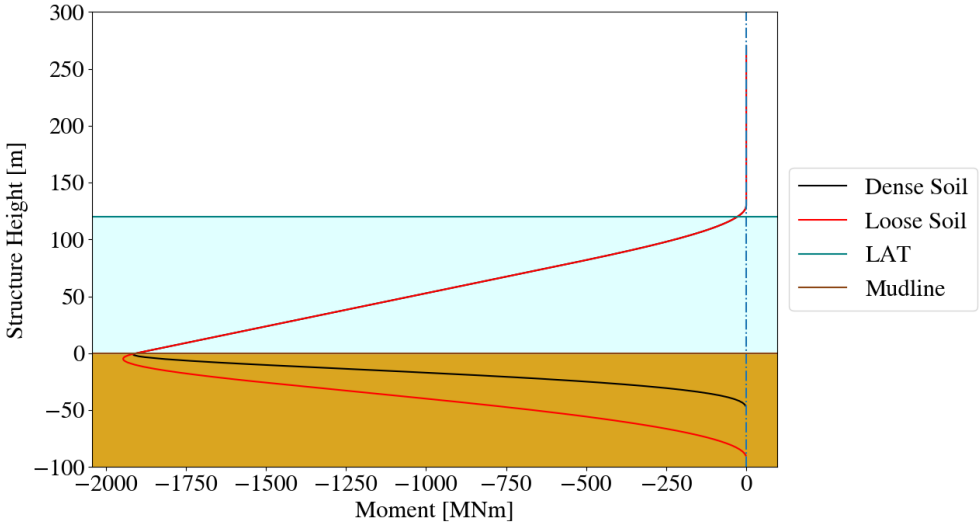

Figure 4.5: Moment Over the System Length for Loose and Dense Soil

4.3. Global Buckling Unity Check

The second unity check assesses the resistance against global buckling. The global buckling check is defined by Equations 4.24 and 4.25 following Eurocode [56]. As an extra safety factor the maximum unity check is lowered from 1.0 to 0.9.

$$\frac{N_{Ed}}{\frac{\chi_y N_{Rk}}{\gamma_{M1}}} + k_{zy}\frac{M_{y,Ed}+\Delta M_{y,Ed}}{\frac{\chi_{LT} M_{y,Rk}}{\gamma_{M1}}} + k_{zz}\frac{M_{z,Ed}+\Delta M_{z,Ed}}{\frac{M_{z,Rk}}{\gamma_{M1}}} \leq 0.9 \tag{4.24}$$

$$\frac{N_{Ed}}{\frac{\chi_z N_{Rk}}{\gamma_{M1}}} + k_{yy}\frac{M_{y,Ed}+\Delta M_{y,Ed}}{\frac{\chi_{LT} M_{y,Rk}}{\gamma_{M1}}} + k_{yz}\frac{M_{z,Ed}+\Delta M_{z,Ed}}{\frac{M_{z,Rk}}{\gamma_{M1}}} \leq 0.9 \tag{4.25}$$

Torsional moments are not considered in this study and bending moment is assumed to act at one direction, which simplifies the above equations to a single unity check given by Equation 4.26

$$\frac{N_{Ed}}{\frac{\chi_z N_{Rk}}{\gamma_{M1}}} + k_{yy}\frac{M_{y,Ed}}{\frac{M_{y,Rk}}{\gamma_{M1}}} \leq 0.9 \tag{4.26}$$

Where:

- N_{Ed} and M_{Ed} are the design normal force and moment respectively
- $\Delta M_{y,Ed}$ and $\Delta M_{z,Ed}$ are the moment due to the shift of the centroidal axis due to bending
- N_{Rk} and $M_{y,RK}$ are the resistances for the normal force and moment
- χ_z is the reduction factor due to flexural buckling term
- γ_{M1} is the partial safety factor for resistance of the monopile to instability, equal to 1.1 [56]
- x,y,z indicate acting directions

The compression- and moment resistances are calculated with Equations 4.27 and 4.28, respectively.

$$N_{Rk} = \frac{A f_y}{\gamma_M} \tag{4.27}$$

$$M_{y,Rk} = \frac{D^3 - (D-2t)^3}{6}\frac{f_y}{\gamma_M} \tag{4.28}$$

χ_z can be estimated from Figure 4.6 for which the dimensionless slenderness ($\bar{\lambda}$) is required. This parameter can be calculated using Equation 4.29 [56]. The standard states that for hot finished hollow sections of S355 steel, being the case for the applied TMCP steel, Curva *a* should be followed in Figure 4.6.

$$\bar{\lambda} = \sqrt{\frac{Af_y}{N_{cr}}} \tag{4.29}$$

In Equation 4.29, N_{cr} is the Euler buckling force which can be found following Equation 4.30. where L_{buck} is twice the total system length from the virtual fixation point to hub height (possible scour is not accounted for in this study).

$$N_{cr} = \frac{\pi^2 EI}{L_{buck}^2} \tag{4.30}$$

Finally, the coupling term k_{yy} is required, which can be calculated following Equation 4.31 for our structure.

$$k_{yy} = C_{my} C_{mLT} \frac{\mu_y}{1 - \frac{N_{Ed}}{N_{cr}}} \tag{4.31}$$

Here moment factor C_{mLT} is equal to 1.0 and C_{my} can be calculated following Equation 4.32

$$C_{my} = 1 - \frac{N_{Ed}}{N_{cr}} \tag{4.32}$$

and μ_y, which is an auxiliary term, can be calculated following Equation 4.33.

$$\mu_y = \frac{1 - \frac{N_{Ed}}{N_{cr}}}{1 - \chi \frac{N_{Ed}}{N_{cr}}} \tag{4.33}$$

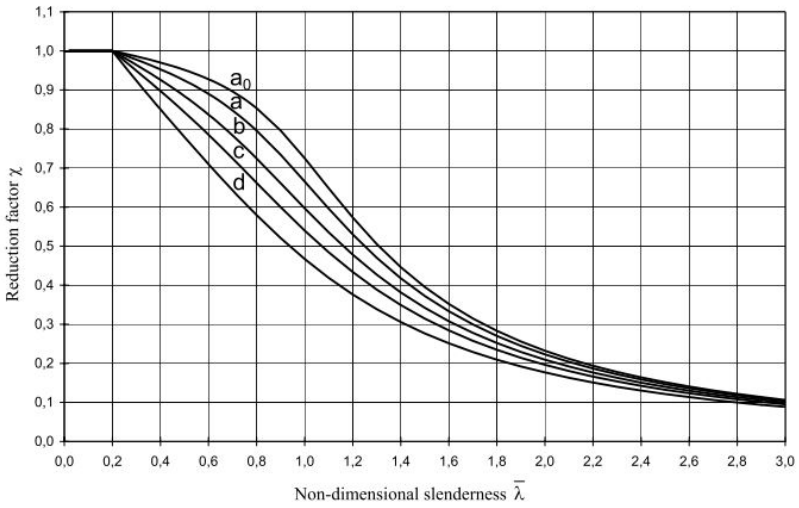

Figure 4.6: Buckling Curves [56]

4.4. ULS Check Results

After the geometries are optimized for their set target first natural frequency and the ultimate limit state checks are conducted, the results are stored and plotted in Python. When no optimized geometry could be found for a water depth - target frequency combination, a geometry matching the target frequency with minimal unity checks is established nevertheless in order to visualize trends.

4.4.1. Optimization Process Results

Figure 4.7 shows the base diameter of the monopile geometries versus the water depth for all target frequencies - water depth combinations. The color bands indicate the base diameter range of the monopiles optimized for very loose and dense sand. In loose soil more steel is required to reach the same natural frequency, hence the marked range of maximum outer diameters. The plot shows that following the stated manufacturing limit of 14.5 meter, all monopiles are within manufacture limits. For the 0.20 Hz geometries, the outer diameter reaches the base diameter limit of 14.5 meters at 100 meter water depth. However, by increasing the wall thickness the target frequency of 0.20 Hz can still be reached without exceeding the manufacturing limit of the wall thickness (150 mm) for a water depth of 120 m. Increasing the natural frequency by increasing wall thickness is, however, the least effective technique material-wise.

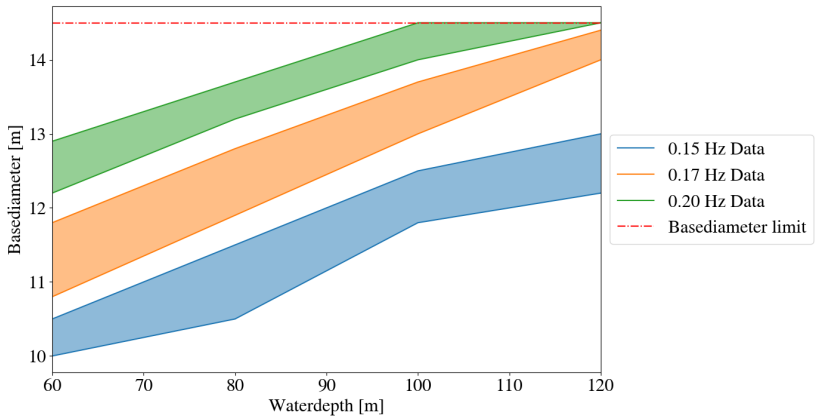

Figure 4.7: Monopile base diameter vs Water Depth

4.4.2. Von Mises Stress Unity Check Results

Figure 4.8 shows the Von Mises yield stress unity checks for all the different configurations under parked conditions, as this turned out to be the critical load case for this unity check. It shows that the 0.15 Hz target frequency geometries generally fail for the entire water depth range, which is a consequence of its relative slenderness with respect to higher target frequency geometries. The rest of the configurations stay below the stated 0.9 limit. Hence, the monopiles designed for a 0.15 Hz target frequency do in general not result in technically feasible designs for the selected water depths. For higher selected target frequencies, the acting Von Mises stresses will not be critical.

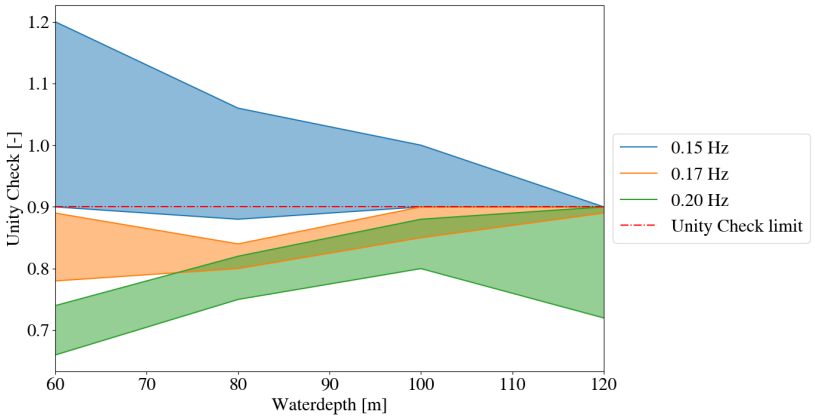

Figure 4.8: Yield Stress Unity Check vs Water Depth

As stated in Equations 4.2 to 4.4 the adopted simplified Von Mises stress consists of three components: Axial force, Overturning moment and Base shear. The component with the highest contribution to the yield stress check is the overturning moment. Figure 4.9 and 4.10 show the wind- and hydrodynamically induced overturning moment for both load cases over depth, respectively. It shows that the wind induced moment during parked conditions is approximately half the value of the power production conditions, due to the thrust force on the rotor. The hydrodynamic overturning moment starts with similar values, but the magnitude increases significantly faster for the parked conditions as a result of the increasing hydrodynamic forcing arm under harsher marine conditions.

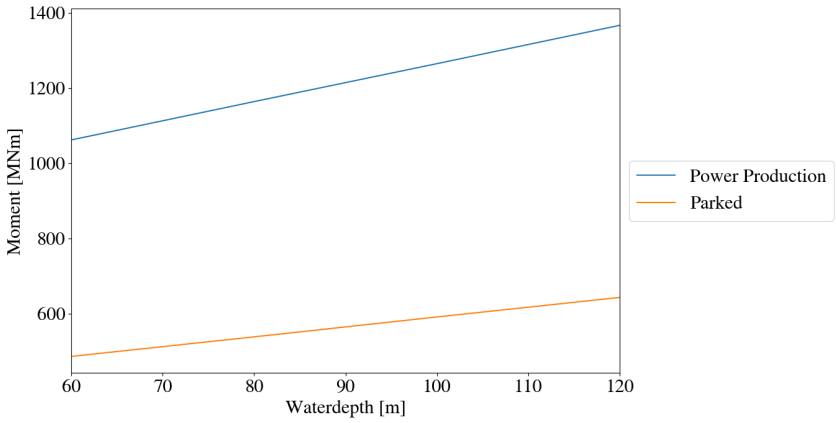

Figure 4.9: Wind Induced Overturning Moment vs Water Depth

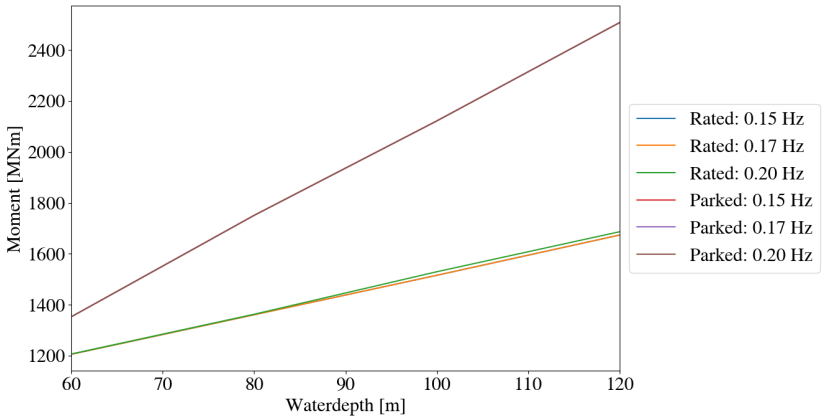

Figure 4.10: Hydrodynamically induced Overturning Moment vs Water Depth

4.4.3. Global Buckling Check Results

Figure 4.11 shows the global buckling unity check for the monopile geometries. For this check the 50 year storm conditions turned out to be the dominant load case as well. The figure shows the same failing geometries as the Von Mises stress check. Relatively higher unity checks can be observed for the 0.15 Hz target natural frequency configurations in combination with the shallower part of the water depth range. This is a result of the need for thinner walled (resulting in less resistant) monopiles to provide the slenderness required to reach the 0.15 Hz target first natural frequency.

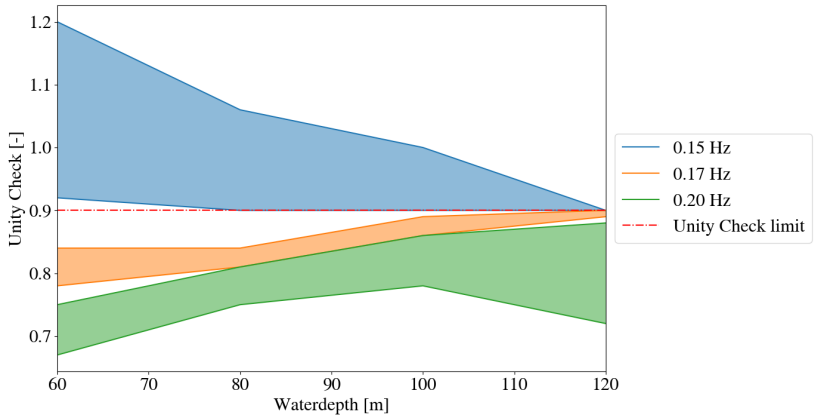

Figure 4.11: Global Buckling Unity Check vs Water Depth

Figure 4.12 shows the total monopiles masses for all configurations. The required steel usage to increase the stiffness, or in other words increase the first natural frequency, is clearly visible in the higher overall mass for 0.20 Hz target frequencies. However, between the geometries designed for 0.15 and 0.17 Hz target first natural frequencies this trend is not obvious. This is due to the required pile length as stated in Equation 3.11. It must be noted that due to the uncertainties in soil reaction, the exact pile length will be different for every monopile. Nevertheless, the graph does give a good indication of the order of magnitude.

In general, steel usage can give a decent indication of relative pricing of the substructures. However, the entire supply chain should be considered for the full financial picture. The total monopile mass graph show that the steel required to reach higher target frequencies cause notable differences in total mass. **Michel's model as comparison**

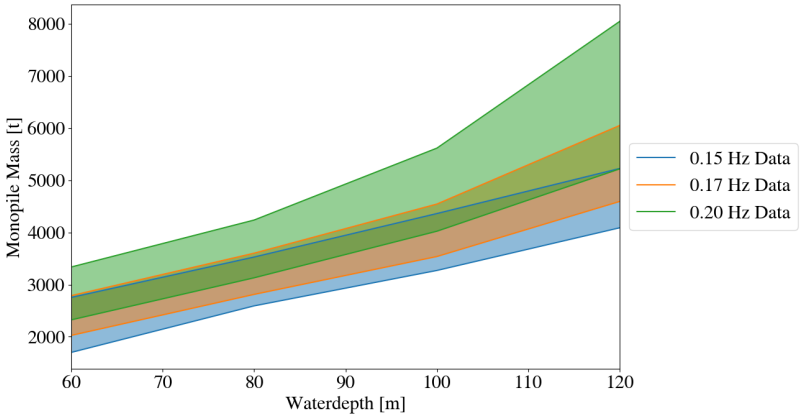

Figure 4.12: Total Monopile Mass vs Water Depth

Due to the large uncertainty of the required monopile mass below the mudline, Figure 4.13 is added showing the total monopile mass above mudline. Here, the effect of higher stiffness on the required steel usage is more evident.

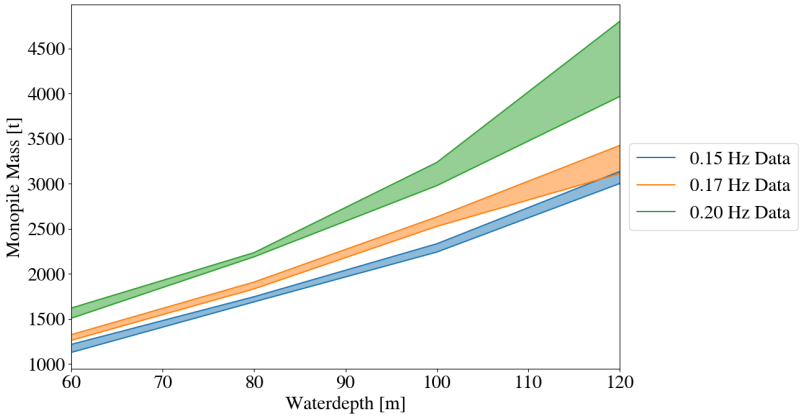

Figure 4.13: Monopile Mass Above Mudline vs Water Depth

4.4.4. Optimization Process Conclusions

When the monopile geometries are optimized for all tested water depth - target frequency combinations, a comparison table can be set up as shown in Table 4.3. It shows that for a target first natural frequency of 0.15 Hz no possible optimized geometries could be found as they fail on both the Von Mises stress check and Global buckling check. For the geometries optimized for a 0.17 and 0.20 Hz target first natural frequency, no limitations were found in the ULS checks.

		Target Frequency		
		0.15 Hz	0.17 Hz	0.20 Hz
Water Depth	60 m	✗	✓	✓
	80 m	✗	✓	✓
	100 m	✗	✓	✓
	120 m	✗	✓	✓

Table 4.3: Output Comparison Table

The table shows that at some point the slenderness of a monopile will cause the system to fail on ultimate limit state for the selected reference location. As the reference location is considered to have a very severe wave climate, this failure is not necessarily true for all locations. Strongly developing offshore wind areas such as the east coast of the US and south east Asia generally have less severe ultimate waves.

5

Fatigue Limit State Check

The monopile geometries for a set target frequency - water depth combination that passed both ULS checks will be checked on their fatigue damage resistance, meaning that the monopiles optimized for a 0.15 Hz first natural frequency are excluded from the fatigue analysis. The determination of fatigue damage is usually done through time series using computational software. Various WTG OEMs own proprietary software to perform those calculations and little information is available in the public domain. This is very time consuming, especially for multiple different monopile geometries such as assessed in the present study. Besides, the 'blackbox' of computational software limits the ability to observe the influence of individual parameters. In order to achieve faster first order results and remain in control of all parameters, it is decided to develop an assessment procedure with suitable simplifications. The procedure consists of an analytic dynamic model and fatigue damage calculation script, which are explained in this section.

5.1. The Dynamic Fatigue Model

As fatigue is a highly dynamic phenomenon, it is necessary to include factors such as mass, damping and stiffness into the model. The model includes a top mass, representing the RNA, a damper, representing the aerodynamic damping caused by the rotor blades during power production [81], and a rotational spring representing soil stiffness [65]. The system also has structural, hydrodynamic and soil damping but they are much smaller than the rotor's aerodynamic damping and hence are neglected. The influence of added mass of the water will be included. In order to reduce the computation time, the triangular load introduced in Section 4.1 is integrated and taken as a point load at 1/3 of the penetration depth which induces the same moment at the mudline. Figure 5.1 shows a visualization of the dynamic model, for which the governing equations are stated and solved below.

The top mass is equal to 1017 t [34] (Table 1.1), the soil spring is calculated via Equation 3.12 and the aerodynamic damping can be calculated using Equation 5.1 which results in a damping of 209585 Ns/m [81]. It is assumed that the turbine is always in power production during fatigue waves conditions [81].

$$c_{\text{aero}} = \frac{1}{2}\Omega N_b \rho_{air} C_{L_\alpha} m_{1b} \tag{5.1}$$

Where:

Ω = Rotational velocity $[rad/s]$
N_b = Number of blades [-]
C_L = Slope of lift coefficient ($= 2\pi$) [34] [-]

The first order static moment of area of the chord along the blade (m_{1b}) is found using reference turbine data [34] and Equation 5.2 [81].

$$m_{1\text{ blade}} = \int_{R_{\text{root}}}^{R} c(r) r\, dr \tag{5.2}$$

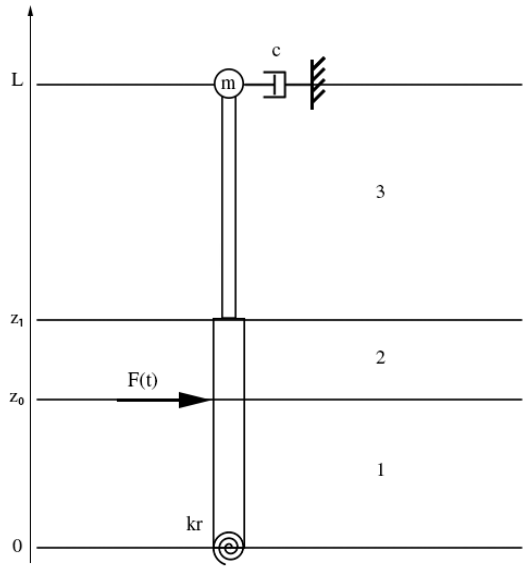

Figure 5.1: Simplified Fatigue Model

As all forcing elements are located on 'nodes' rather than the 'beams', the equations of motion for all 3 segments have a similar form, described by Equation 5.3. The axial component is negligible for the fatigue analysis, which is governed by the bending stress cycles caused by wave forcing. Also, the Ansys modal analysis performed with a full monopile geometry in Section 3.1.1 showed a difference in first natural frequency of less than 2% between inclusion and exclusion of the gravity on the tower and monopile. Research shows that there is no strong correlation between fatigue damage and mean thrust ($R^2 = 0.48$ for a 10 MW wind turbine supported on a monopile foundation [82]) and thrust is therefore not considered. Also the current forcing is considered constant in this research and will hence not contribute to the magnitude of the stress cycles.

$$\rho A_n \frac{\partial^2 u_n}{\partial t^2} + EI_n \frac{\partial^4 u_n}{\partial z^4} = 0 \tag{5.3}$$

When the submerged monopile accelerates, so too must the seawater surrounding it. This added mass behaviour is modelled by increasing the mass of the monopile for the submerged part. The added mass can be calculated with Equation 5.4 [67] where the added mass coefficient C_a is equal to 1.0 [1]

$$m_a = C_a \rho_w \frac{\pi D^2}{4} \tag{5.4}$$

The boundary conditions at $x = 0$ and $x = L$ are defined by Equation 5.5, neglecting the rotational inertia of the RNA:

$$\begin{aligned} u_1(0) &= \left.\frac{\partial^2 u_3}{\partial z^2}\right|_{z=L} = 0 \\ EI_1 \left.\frac{\partial^2 u_1}{\partial z^2}\right|_{z=0} &= k_r \left.\frac{\partial u_1}{\partial z}\right|_{z=0} \\ EI_2 \left.\frac{\partial^3 u_3}{\partial z^3}\right|_{z=L} &= m \left.\frac{\partial^2 u_3}{\partial t^2}\right|_{z=L} + c \left.\frac{\partial u_3}{\partial t}\right|_{z=L} \end{aligned} \tag{5.5}$$

All the interface conditions have a similar form to the conditions defined in Equation 4.11, except the shear balance at $z = z_0$. Here, the shear force should balance with the point load $F \cdot \sin(\Omega t)$.

The forcing is assumed to be in a pure harmonic form, so the steady state solution to the problem can be separated in a space- and time dependent part as shown in Equation 5.6. This can be substituted in the above

stated system to find the governing equations in the frequency domain, for which the equation of motion is rewritten to in a more convenient form as shown in Equation 5.7.

$$u_n(z,t) = U_n(z)e^{i\Omega t} \tag{5.6}$$

$$\frac{d^4U_n(z)}{dz^4} - \beta^4 U_n(z) = 0, \quad \beta^4 = \frac{\rho_{steel} A_n}{EI_n}\Omega^2 \tag{5.7}$$

Due to the introduced aerodynamic damping in the system, the solutions have an imaginary and real part. In order to find the maximum amplitude of the harmonic reactions, the solution should be phase shifted with a phase angle defined by the arc-tangent of the real part over the imaginary part of the desired solution. Figure 5.2 shows the real part, the imaginary part and the phase shifted resulting horizontal top displacement to a 1 meter high unit wave for a range of frequencies. It shows that in the resonating frequencies, the imaginary part will become dominant. This is due to the fact that the motions become highly damping controlled in this frequency areas.

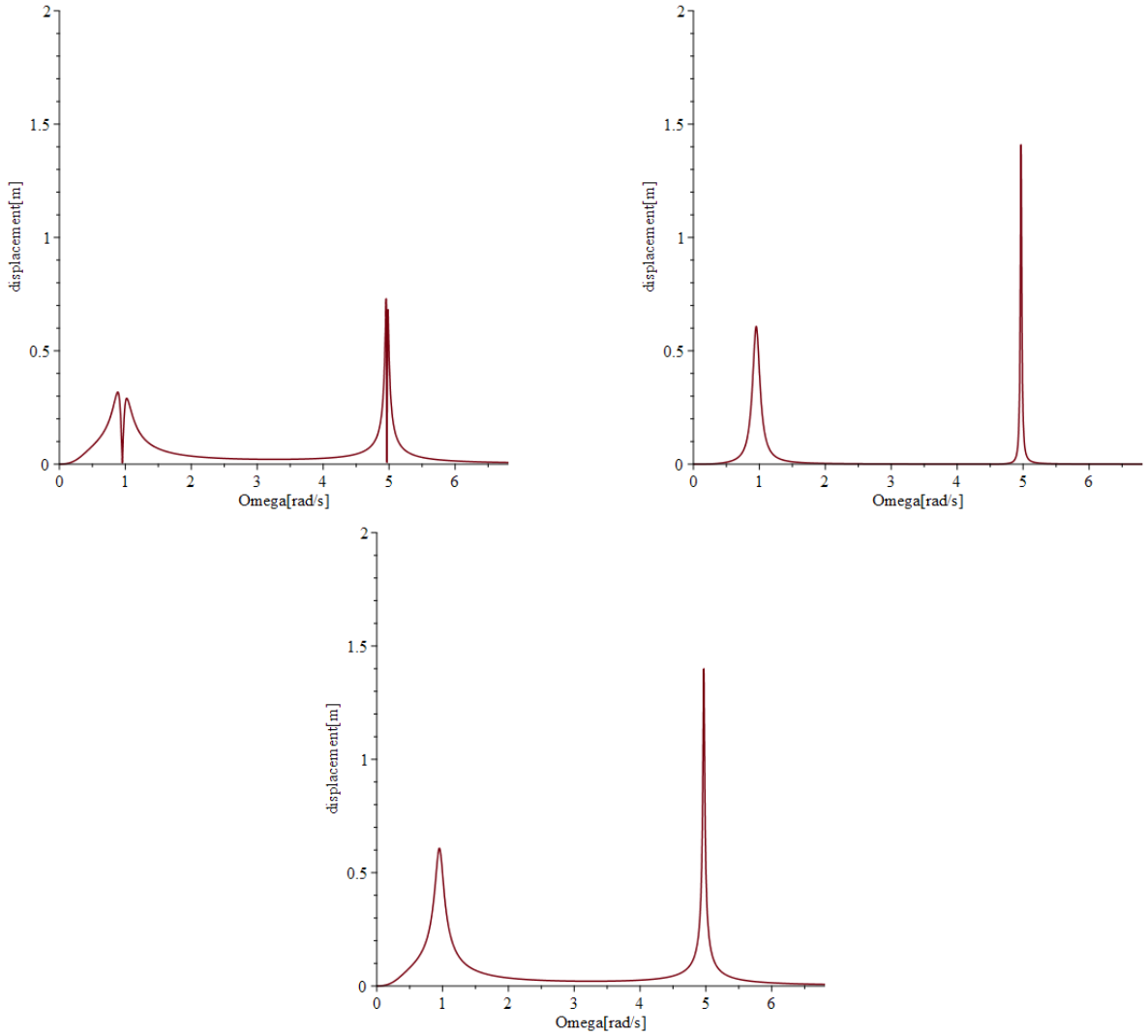

Figure 5.2: Top Left: Real Part, Top Right: Imaginary Part, Lower: Phase Shifted Solution

5.2. Wave Forcing and Influence of Wave Frequency

To find the magnitude of the wave forcing the exponentially decaying inertia component of the Morison wave forcing (as stated in Equation 2.11 and 2.21) is integrated from $z_1 - 0.5\lambda$ to z_1, as the influence of the waves can be considered negligible beyond half a wave length below the surface [44]. It is well-known that the magnitude of wave forcing at the waterline increases for an increasing wave frequency as the acceleration of the particles increases [44]. In a fully inertia dominated system, this force increase will be quadratic. However, an important hydrodynamic factor that is often forgotten is the decay of influence depth (0.5λ) with increasing wave frequency, which is also exponential. Figure 5.3 shows the inertia force at the waterline, the influence depth of the waves and the total integrated force for a range of wave frequencies. It shows that the two factors cancel each other out and the total forcing stays constant with wave frequency. The vertical acting location of the forcing, however, does change with frequency affecting the resulting overturning moment.

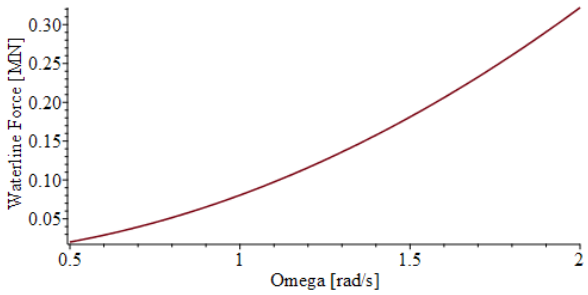

(a) Force at Waterline

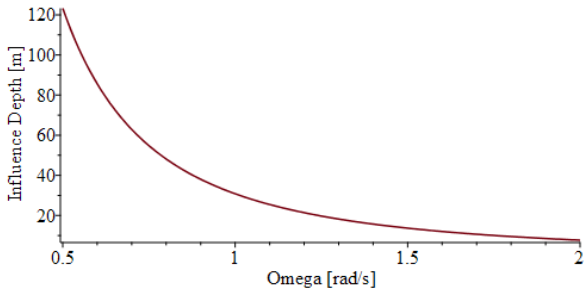

(b) Influence Depth

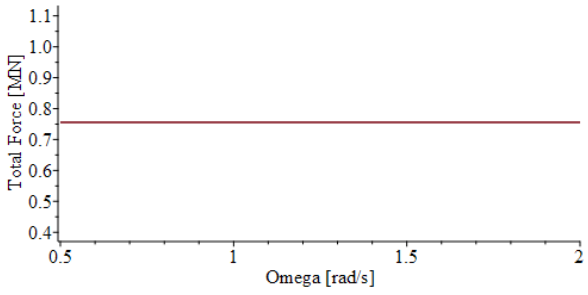

(c) Total Integrated Force

Figure 5.3: Influence of Wave Frequency

This finding can also be analytically proven as shown in Equation 5.8 by taking the integral of the inertia forcing in parametric form. It shows that the forcing is independent of wave frequency.

$$\int_0^{\frac{\lambda}{2}} A\dot{u}dz = \int_0^{\frac{\lambda}{2}} A\omega^2 e^{-kz}dz = \int_0^{\frac{\lambda}{2}} e^{-\frac{2\pi}{\lambda}z}\frac{2\pi g}{\lambda}Adz = \left(-ge^{-\frac{2\pi\lambda}{2\lambda}} - -g\right)\cdot A = \left(1-e^{-\pi}\right)gA \tag{5.8}$$

Where: $A = \frac{H}{2}\frac{\pi}{4}\rho_w C_m D^2 \sin(\Omega t)$

5.3. Analytical Model Validation using Ansys

The same full monopile-tower geometry as shown in Figure 3.3 was used to validate the analytical model in Ansys. Figure 5.4 shows the top displacement comparison between the Ansys and Maple model. It shows that the first natural frequency shows great resemblance and the order of magnitude of the first peak is equal. The quite significant difference in the second natural frequency can be explained by the fact that the analytical model consists of two parts, whereas the Ansys full geometry consists of a continuously changing geometry over height. The largest differences in geometry(and thus in bending resistance) is therefore more pronounced in the middle part of the structure, which influences the first natural frequency less than the second. The figure shows that the second resonance peak occurs at approximately 0.75-0.85 Hz. This means that this peak will not coincide with the realistic exciting frequencies as marked in the Figure 5.4. Therefore, it is assumed that the system will only be excited in its first mode by the waves.

Note: The aerodynamic damper is modelled as a moving body to a fixed point connection as shown in Figure 5.1. Therefore the damper doesn't follow the rotations of the top part and will underestimate the damping, especially in the second mode. The second mode is, however, not important in the current analysis as the figure shows that it will not be excited by the main forcing component being the wave forcing.

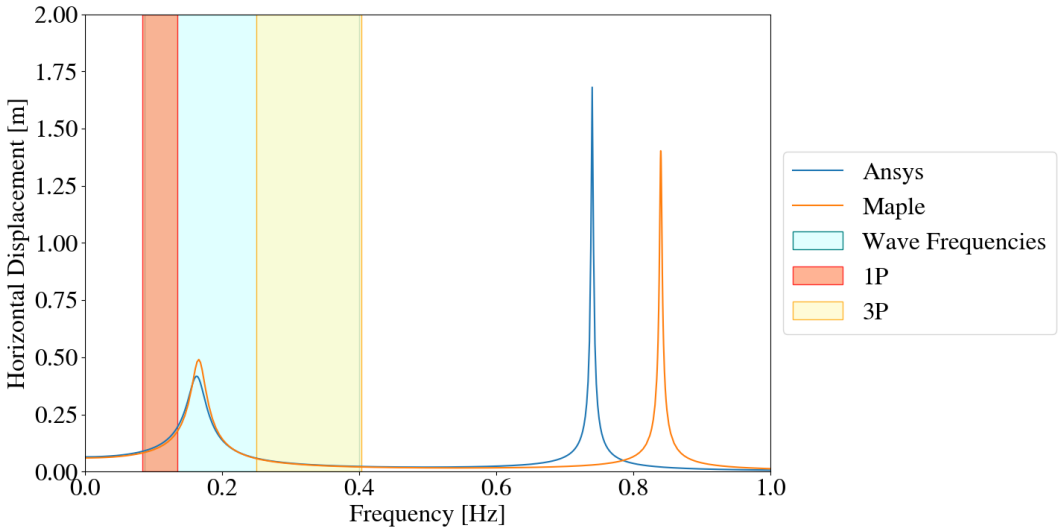

Figure 5.4: Comparison of the Ansys and Maple models

Ansys is also used to find the free decay response to an impulse force, of which a result is shown in Figure 5.5 for visualization. This test is used to extract the damping ratio in the system following Equation 5.9. The damping ratio showed to be relatively independent of the water depth. This is due to the aerodynamic damping mainly working on the relatively flexible tower part, rather than the stiff monopile foundation. The damping ratio is equal to approximately 8.5% using the aerodynamic damping found from Equation 5.1. This value is well in line with industry experiences [81]. An additional 0.5-1% structural damping is typically added, thus the total damping is an underestimation [81]. However, the aerodynamic damping is assumed to be present during the entire fatigue analysis at rated rotor velocity, which is an overestimation. In reality the damping resulting from the rotor is highly complex as it depends on a large number of variables. As the system damping is highly dominated by aerodynamic damping, other damping forms are neglected for the purpose of the this study. In Equation 5.9 the amplitudes are both the maxima and minima (half cycle) of the top displacement.

$$\zeta_i = 2\frac{\ln\left(\frac{amp_{i-1}}{amp_i}\right)}{2\pi} \tag{5.9}$$

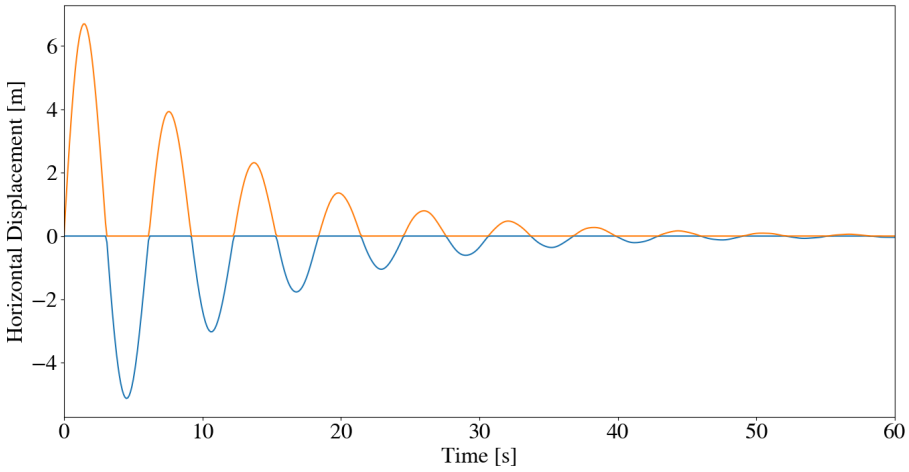

Figure 5.5: Free Decay Test Result for Reference Geometry

5.4. Effect of Hydrodynamic Added Mass

With the increasing relative submerged part of the offshore wind turbine system, the effect of hydrodynamics become increasingly visible. Section 4.4 already showed that the wave forcing becomes highly dominant over the wind forcing. As stated before, the system showed to be in the inertia dominated regime. Inertia force is governed by the acceleration of mass. When the monopile accelerates, the mass of the fluid surrounding it must accelerate as well. The calculation of this added hydrodynamic mass is done following Equation 5.4.

Figure 5.6 shows the top displacement of the wind turbine for two monopiles designed for a 0.17 Hz first natural frequency in 80 meter and 120 meter water depth. For both geometries the analysis is run with and without added hydrodynamic mass for the submerged part.

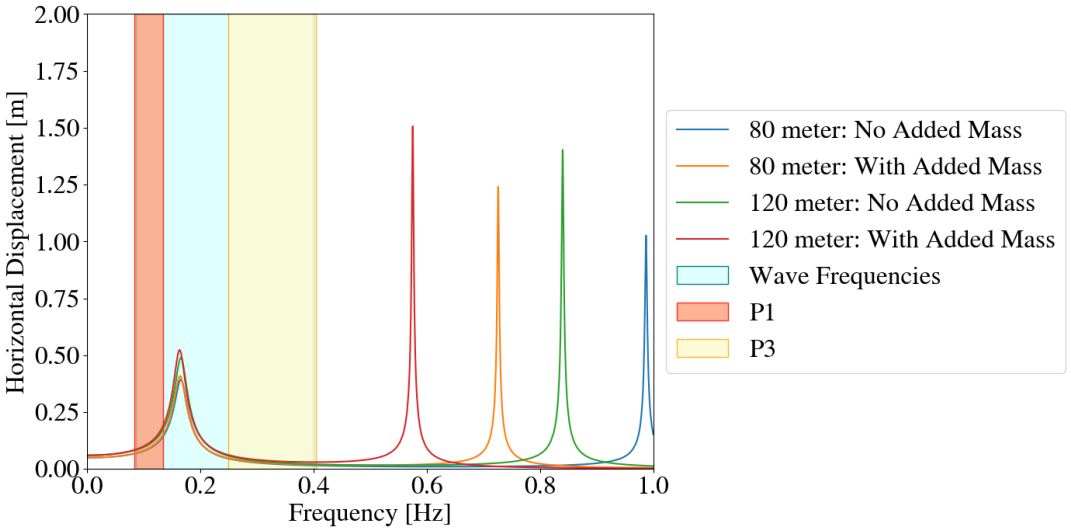

Figure 5.6: Effect of Hydrodynamic Added Mass

Inertia force is related to the acceleration of mass. The submerged part has more pronounced acceleration in the second mode than in the first mode. Therefore, the second mode is affected far more significantly in comparison with the first mode reaction. The addition of added mass will, however, still not cause the second mode to be activated by the present wave frequencies or the 1P and 3P.

5.5. Fatigue Calculation Method

The maximum resulting bending stress cycles due to the wave forcing for different frequencies can be found. As the forcing is fully in the inertia dominated regime, the resulting bending stress scales linearly with the wave height (Equation 2.21 shows a linear relation with crest height). Therefore, the stress response can be plotted against a unit wave of 1 meter wave height to find the response to all important fatigue waves. The change in waterline due to wave height is considered negligible for the fatigue inducing waves. The bending stress can be found using Equation 5.10, where the environmental safety factor (γ_e) is equal to 1.0 [25]. The wave spreading factor (γ_s) is set to 0.85, which is the average wave spreading factor for the Northern North Sea. Here the overturning moment (M) can be found using Equation 4.23 and W is the elastic section modulus.

$$\sigma_x = \frac{M}{W}\gamma_e\gamma_s \tag{5.10}$$

Figure 5.7 shows the bending stress to frequency response functions of the 0.17 Hz and 0.20 Hz design frequency geometries for a water depth of 60 and 120 meters. It shows that the difference in resulting bending stress is limited and the resulting bending stress is therefore considered independent of water depth. The 0.17 Hz target frequency geometries show higher response and will therefore have a lower fatigue life. The geometries designed for loose and dense soil also showed a difference of less than 5%. Therefore, the resulting 'stress frequency response functions' (SFRF) are assumed to be valid for both the water depth and soil type range.

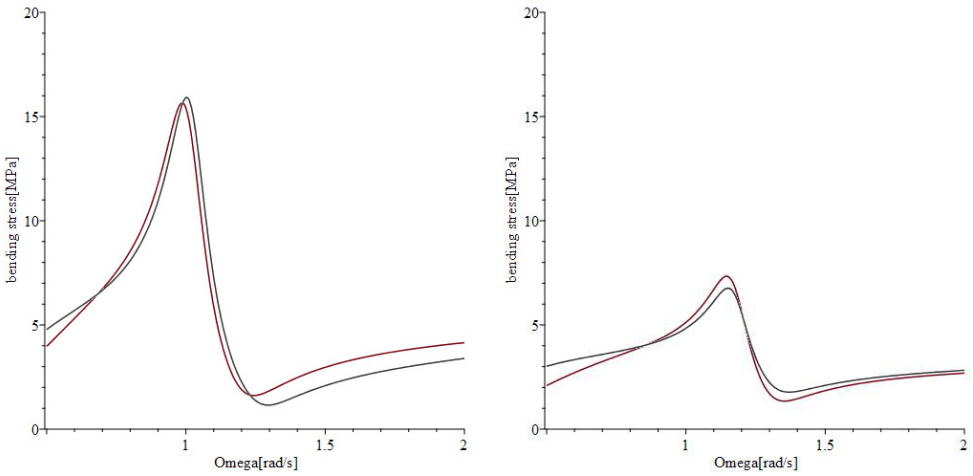

(a) 0.17 Hz (b) 0.20 Hz

Figure 5.7: Bending Stress to Frequency Response Functions, where red is 60 meter water depth and black is 120 meter water depth

To find the total fatigue life for the 25 year design life of the foundations, wave data of the reference location is required. A scatter diagram of significant wave height and spectral peak period at Buchan Deep for the period 1958 - 2010 (53 years) is obtained from Nora10 hindcast data [54] and shown in Figure 5.8. The duration of each given sea state is 3 hours, as this is the reference period for a sea state to be normally considered stationary [80]. As the bins of the peak period and wave height are 1 second and 1 meter respectively, the accuracy is limited. Especially for the peak period this can yield a large error due to the relatively large dynamic amplification differences as shown in Figure 5.7. However, as each wave states needs at least 3 hours to be considered stationary, it is very difficult to acquire more specific data. For the fatigue analysis all calculations are thus done with the average of the bin (e.g. 3.5 seconds for the 3-4 second bin).

H_S (m)	Spectral peak period (T_p) - (s)																				
	2-3	3-4	4-5	5-6	6-7	7-8	8-9	9-10	10-11	11-12	12-13	13-14	14-15	15-16	16-17	17-18	18-19	19-20	20-21	21-22	22-23	Sum
0-1	177	3746	10423	9068	7551	4984	2983	2033	1142	626	309	167	63	38	12	3	4					43329
1-2		57	5281	13966	12849	10034	7653	5074	3720	2476	1254	571	245	109	36	9	3					63337
2-3			32	1413	7085	7423	4826	3338	1985	1397	1132	582	228	125	31	12	7					29616
3-4				4	599	2588	3559	2404	1332	553	388	204	141	63	20	5	2	1	1			11864
4-5					15	168	1046	1398	993	445	152	94	50	22	14	4			1			4402
5-6						5	113	429	497	358	114	57	12	10	5							1600
6-7							3	55	132	166	103	43	13	3	2							520
7-8								2	18	42	57	16	10	4	4							153
8-9									1	6	14	7	7	2	1							38
9-10												1	2									3
10-11											1											1
Sum	177	3803	15736	24451	28099	25202	20183	14733	9820	6069	3524	1742	771	376	125	33	16	1	2	0	0	154863

Figure 5.8: Scatter Diagram of significant wave height (H_s) and spectral peak period (T_p) at Buchan Deep for the period 1958 - 2010 (53 years). Duration of sea state is 3 hours.

Assuming that the fatigue damage accumulates linearly with the number of stress cycles, stress cycles with a constant stress range ($\Delta\sigma$, equal to two times the stress found from the stress frequency response functions) can be related to the number of cycles to failure (N_f) using Wöhler's equation [25]. This number can be found on so called S-N curves, which give the number of cycles to failure for given stress ranges and different member types [22]. These curves (as shown in Figure 5.15) consist of two slopes defined by material parameters $m = 3$ and $m = 5$ for the upper and lower region respectively. If the magnitude of a stress cycle is above the given stress limit at 1 million cycles, the $m = 3$ curve is used. If the stress magnitude is below this value, the $m = 5$ curve is used. The equation for the number of cycles to failure (N_f) can than be given by Equation 5.11, where $\log \bar{a}$ is the intercept of the $\log N$ axis and the S-N curve.

$$N_f = \bar{a}(\Delta\sigma)^{-m} \tag{5.11}$$

Standards dictate the use of the D-class S-N curve for piles [22]. Industry practice suggest, however, that within the near future higher class SN curves can be used, due to improved welding techniques and standardization. Therefore, in this analysis the fatigue damage is assessed for a B2 class (weld equivalent to base material), C1 (grinded circumferential butt weld), and D (circumferential butt weld) S-N curve which are curves for different weld qualities. The fatigue strength of welded joints is to some extent dependent on plate thickness, due to the local geometry of the weld toe in relation to the thickness of the adjoining plates. The stress cycles are modified for the C1 and D curve with a so called thickness factor given by Equation 5.12 [22].

$$\gamma_t = \left(\frac{t}{t_{ref}}\right)^k \tag{5.12}$$

Here t is the wall thickness of the monopile and t_{ref} is the reference thickness, which is equal to 32 mm for tubular joints. Table 5.1 show the $\log \bar{a}$ and thickness exponent k for the three different S-N curves. As S-N curve B2 represents an equivalent weld quality to the base material, it is not affected by plate thickness differences and the thickness factor is not required.

Table 5.1: $\log \bar{a}$ and thickness exponent k

SN curve	$\log \bar{a}(m = 3)$	$\log \bar{a}(m = 5)$	k
B2	14.685	16.856	-
C1	12.049	16.081	0.10
D	11.764	15.606	0.20

The fatigue damage (D) is hereafter predicted using the Palmgren-Miner summation [22]. Assuming a narrow-banded wave spectrum where the number of stress cycles (n_i) over a given time are inversely related to the peak wave period, the fatigue damage can be simplified as shown in Equation 5.13. Here, t_{life} is the 25 year lifetime in seconds and P is the probability of occurrence of the assessed wave state as found from Figure 5.8.

$$D = \sum_{i=1}^{n_{\text{wavestate}}} \frac{n_i(\Delta\sigma_i)}{N_{f,i}(\Delta\sigma_i)} \approx \sum_{i=1}^{n_{\text{wavestate}}} \frac{t_{life} P_i\left(\frac{1}{T}\right)}{\bar{a}\cdot(\Delta\sigma)^{-m}} \tag{5.13}$$

DNVGL-RP-C203 dictates that the total fatigue over the design life of the structure must be factored by a design fatigue factor (DFF), which varies from 1 to 3. Following the code, a factor of 2.0 may be used in atmospheric or submerged zones if an inspection plan is established with documented inspection method and sufficient inspection intervals. For this fatigue analysis, it is assumed that such an inspection method is established and a DFF of 2.0 is adopted. However, the range of DFF (1-3) is rather large and as it is a linear multiplication factor, a DFF reduction from 2.0 to 1.0 would result in half the accumulated fatigue damage. Solutions to reduce the DFF close to 1.0 are a recommended topic of further research.

5.6. Operational Loads

With the significant increase of power rating of offshore wind turbines, the dimensions and masses of the moving components also increase. The motions of these components in combination with the environmental loading cause so called operational loads to the system. This section assesses a set of expected operational loads and estimates the order of magnitude of these forcing components.

5.6.1. 1P Loading: Mass Imbalance

As shown in Figure 3.2, the system is subjected to a cyclic loading with a frequency in the rotational frequencies or 1P frequency range. The main source of this forcing is the rotor mass imbalance. As the magnitude of this forcing depends on the extent of the imbalances, it is difficult to assign an exact number to this. In this section an estimation is given for the fore-aft bending moment in the monopile caused by the mass imbalance and rotor overhang.

The mass imbalance (I_m) is modelled as an additional mass (m) at a distance (R) from the centre of the hub. This mass causes an extra centrifugal force (F_{cf}), which can be calculated using Equation 5.14 [4].

$$F_{cf} = ma = mR\Omega^2 = I_m\Omega^2 \tag{5.14}$$

This centrifugal force is translated to a bending moment in the system using Eqation 5.15. Where b is the rotor overhang equal to 11.59 m.

$$M_{1p} = F_{cf} b \tag{5.15}$$

To estimate the fatigue induced by a possible mass imbalance, the resulting moment from the centrifugal force is taken and the recurring stress cycles are calculated. As data on mass imbalance is scarce, available upper boundary mass imbalance values for the Siemens SWT-107-3.6 turbine are scaled up to the reference 15 MW dimensions as shown in Equation 5.16 [4, 73], where M and D are the rotor mass and diameter of the reference ($15MW$) and Siemens ($SWT-107$) turbine respectively.

$$I_{m,15MW} = I_{m,SWT-107}\cdot\frac{M_{15MW}}{M_{SWT-107}}\cdot\frac{D_{15MW}}{D_{SWT-107}} = 2000\cdot\frac{195}{95}\cdot\frac{240}{107} = 9208kg\cdot m \tag{5.16}$$

Figure 5.9 shows the bending cycles resulting from the rotor mass imbalance at rated rpm for all optimized monopile geometries. It shows that the magnitude of these bending cycles is very small. Even though it is a very frequently recurring stress, it can be considered negligible with respect to the wave induced bending stress cycles. Typically, the SN curves used to calculate accumulated fatigue damage start at a stress range threshold of 10 MPa, which is not reached for the 1P mass imbalance loading cycles. Also, the selection of the target first natural frequency is sufficiently far away from the 1P frequency region to avoid dynamic amplification.

Generally, larger rotors rotate at slower RPMs than smaller turbines. The centrifugal force and thus bending stress cycles scale quadratically with the rotational velocity. Therefore, it can be expected that the relative share of the 1P forcing due to mass imbalance reduces for larger turbines. Also, the precision of the blade manufacturing process can be increased by new developments, which also reduces the centrifugal forcing imbalance.

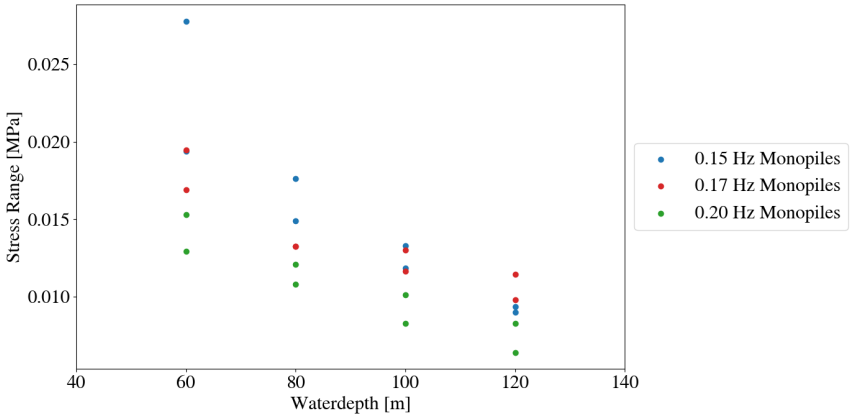

Figure 5.9: 1P Loading cycles for All Optimized Monopiles

5.6.2. 3P Loading: Blade Passage and Tower Shadowing

As shown in Figure 2.2, the wind produces a varying drag force over the height of the turbine tower. When a turbine blade passes the tower (i.e. it points downwards) the flow downwind of this blade is disturbed and the drag on the tower is decreased for a short period, which is called load loss [4]. The frequency of this load loss is three times the rotational velocity (1P), which is equal to the 3P or blade-passing frequency. The magnitude of the stress cycles caused by the drag loss is estimated using the ratio between the blade loading area and the tower loading area. The drag force on the covered part of the tower is taken to be zero.

Equation 5.17 gives the 3P drag loss moment amplitude at the virtual fixation point from which the bending stress cycles are calculated. Here, the loading surface of the blade (A_{blade}) is 440 m^2 and the loading surface of the tower (A_{tower}) is 990 m^2. M_{drag} is the overturning moment caused by the drag force on the turbine tower from $z = z_{hub} - R_{rotor}$ to $z = z_{hub}$.

$$M_{3P} = R_A M_{drag} = \frac{A_{blade}}{A_{tower}} M_{drag} \tag{5.17}$$

Figure 5.10 shows the bending stress cycles caused by the drag loss of the tower during cut-out wind speed velocities. This is the maximum mean wind velocity under which the turbine will be operating, which will result in the largest drag loss on the turbine tower. The figure shows that the bending stress cycles stay below 8 MPa and are therefore considered negligible with respect to the wave induced stress cycles.

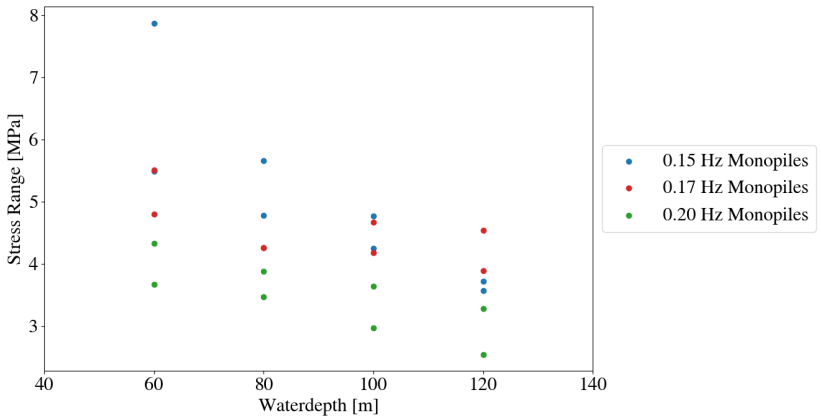

Figure 5.10: 3P Loading cycles for All Optimized Monopiles

The presence of the turbine tower also alters the local wind field. For an upwind turbine tower the blades will encounter a reduced wind speed when passing the tower. This will in turn lead to a cyclic reduction in thrust, fluctuating with the blade passing frequency [75].

The equivalent wind speed accounting for tower shadow ($u_{eq,ts}$) can be found by Equation 5.18 [75]. It should be noted that thrust reduction only occurs on the blades rotating into the lower half of the swept area. The thrust fluctuations are expected to be the largest around the rated wind speed, as the rotor thrust curve is the steepest around this point (Figure 2.5).

$$u_{eq,ts}(t,\theta) = \frac{u_0 a^2}{3\,(R-r_0)} \sum_{n=1}^{3} \left(\frac{r_0}{r_0^2 \sin^2\theta_n + b^2} - \frac{R}{R^2 \sin^2\theta_n + b^2} \right) \tag{5.18}$$

a = Tower Diameter (4 m)
R = Rotor Radius (120 m)
r_0 = Hub Radius (3.75 m)
θ_n = Location of Blade n ($\theta + n \cdot \frac{2\pi}{3}$)
b = Rotor Overhang (11.59 m)

The Equation is used to produce an equivalent wind speed plot for a full rotor rotation during rated wind speed conditions as shown in Figure 5.11

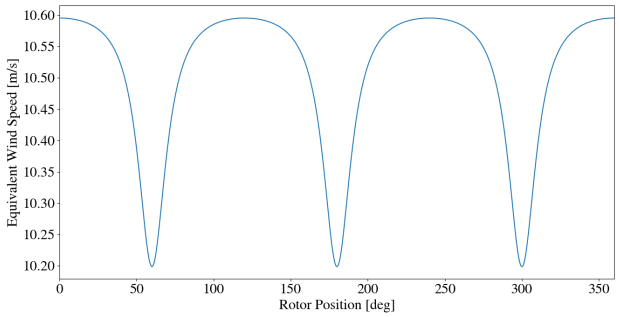

Figure 5.11: Equivalent Wind Speed for Full Rotor Rotation

This equivalent wind speed drop results in a total thrust force fluctuation of approximately 0.1 MN following the rotor thrust curve. As the thrust is only lost on 1 of the 3 blades, this is a fluctuation of approximately 33 kN recurring at blade passing frequency. This fluctuation results in bending stress cycles for the optimized monopiles as shown in Figure 5.12. The magnitudes of these cycles can again be considered negligible with respect to the wave induced bending stress cycles.

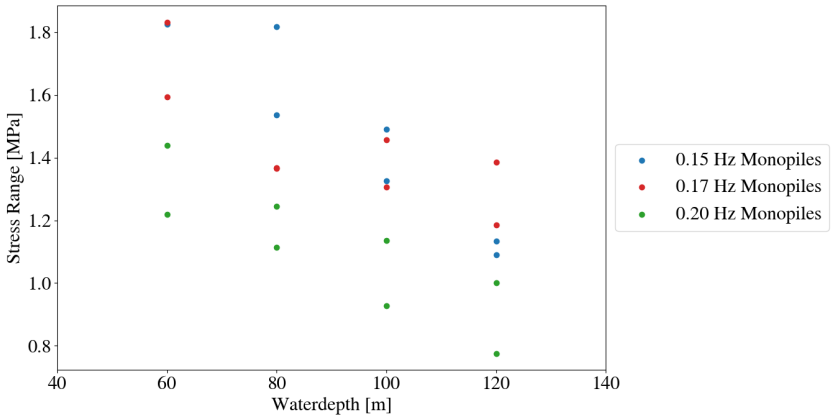

Figure 5.12: Tower Shadowing Induced Bending Stress Cycles

5.6.3. Turbulence Induced Thrust Fluctuations

In order to assess the validity of the assumption that the wind induced fatigue damage can be neglected, the maximum bending stress cycles due to turbulence induced thrust variations are estimated and compared with the wave induced bending stress cycles. The maximum fluctuation in thrust is expected to happen due to variations in wind speed around the rated wind speed. As shown in Figure 2.5, the variation of the rotor thrust for variation in wind speeds is the largest in this area.

The maximum expected wind speed fluctuation at hub height during rated conditions is taken as the difference between the mean rated wind speed at the hub (10.59 m/s) and the extreme operating gust (EOG) as calculated following Equation 2.2, which is equal to 14.68 m/s. The difference in thrust due to this gust is extracted from the curve as shown in Figure 5.13. In reality, this is an overestimation as the control system won't be able to pitch the blades instantaneously and additionally the total variation in thrust will be reduced due to the blades load shedding capacity (which increases for larger turbines).

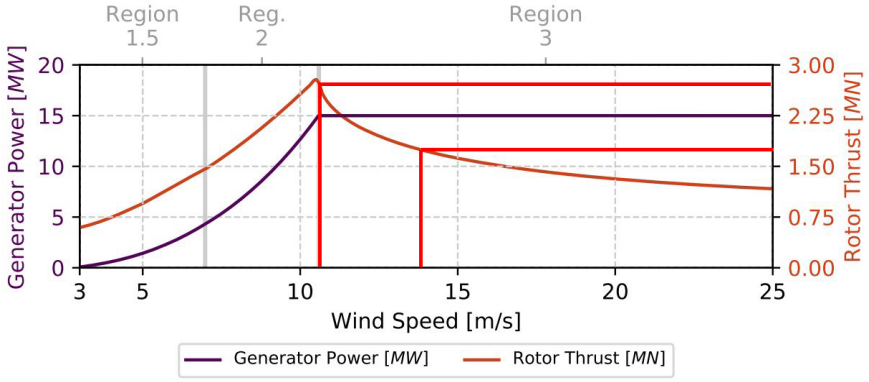

Figure 5.13: Rotor Thrust Fluctuation Estimation

The figure shows that the variation in rotor thrust is approximately 0.9 MN. This thrust force variation is transferred to a bending stress at the virtual fixation point of the monopiles. All the bending stress cycles resulting from the maximum expected thrust fluctuation are plotted for all the geometries in Figure 5.14.

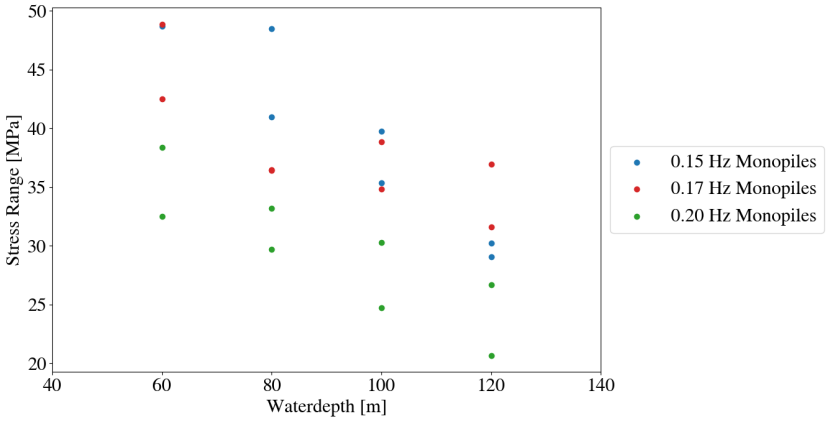

Figure 5.14: Extreme Operating Gust Induced Bending Stress Cycle

The figure shows the **maximum** expected stress cycles due to thrust fluctuation. Hence, all thrust induced bending stress cycles will stay below this value. The typical period of a turbulence in the Kaimal spectrum is 1 to 10 minutes [4]. The total accumulated fatigue damage resulting from the maximum expected thrust fluctuation induced bending stress cycle (48 MPa) with a return period of 1 minute (which both, again, are an overestimation) still only results in a worst case additional 3.5 % in the fatigue unity check.

Therefore, the neglecting thrust fluctuations on the fatigue damage is considered valid for this research. For the turbine tower design, however, the accumulated fatigue due to thrust fluctuations is of importance. It is also observed that the maximum wind induced bending stress cycles decrease for increasing water depth. This is in line with the earlier found results: the resistance against failure of the system is increasingly used to withstand hydrodynamic loading rather than aerodynamic loading. This can be explained by the difference in relative increase of forcing arm. For example, when the water depth increases from 10 to 20 meters, the hydrodynamic forcing arm approximately doubles, whereas the aerodynamic forcing arm only increases by a factor of 1/17. In other words, the hydrodynamically induced bending stress increases significantly faster with increasing water depth than the aerodyanmically induced bending stress.

5.7. Fatigue Analysis Results & Conclusions

As shown in Figure 5.7, the fatigue damage is assumed independent of water depth and therefore only two fatigue analyses are required. In order to account for the dependence on thickness variation for the C1 and D graded welds, the minimum and maximum wall thickness at the base over the entire water depth range are substituted in Equation 5.12.

Using the wave scatter diagram provided in Figure 5.8, the total fatigue damage over the design lifetime of 25 years. Figure 5.15 shows the different S-N curves for steel in seawater in cathodic protection. The graph show the number of cycles to failure on the x-axis for a given stress range on the y-axis. It clearly shows that the D-curve allows a significantly lower number of cycles to failure than the C1 and B curve.

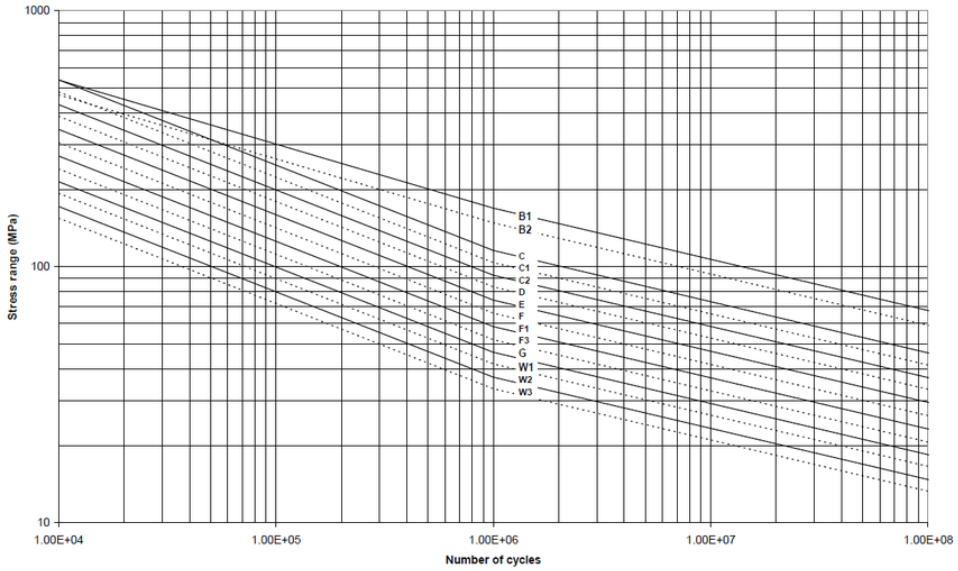

Figure 5.15: SN curves for steel in seawater with cathodic protection [22]

Combining the wave data with the S-N curves, the analysis can be ran for the two target frequency monopile geometries. The accumulated damage unity checks over the design life are shown in Table 5.2. This check must stay below 1.0 to pass the fatigue analysis checks.

Table 5.2: Results of FLS analysis

SN curve	0.17 Hz	0.20 Hz
D	19.64-22.46	0.15-0.25
C1	6.23-6.68	0.03-0.04
B2	0.41	0.00

Table 5.2 shows that the geometries designed for 0.20 Hz first natural frequencies have very high resistance against the fatigue waves at the reference location, whereas the monopiles designed for a 0.17 Hz first natural frequency fail the unity check for two of the three selected S-N curves. The lower resistance against fatigue damage is not only due to the higher acting stress cycles as shown in Figure 5.7, but also due to the fact that the probability of waves with a frequency close to the first natural frequency of 0.20 Hz frequency (equal to 5 seconds) is significantly lower than the probability of waves with a wave frequency close to 0.17 Hz.

This implies that the fatigue life of the system is highly locality driven. In general more 'open' waters have longer wave periods as their fetch is longer, providing more time for waves to build up [44]. In order to assess the effect of a different more open location, the entire scatter diagram was shifted a wave period of 0.5 and 1 second higher. Table 5.3 shows the results of this analysis for the 0.17 Hz target frequency monopiles. The results show a significant decrease in fatigue damage, underlining the necessity of proper metocean analysis for each different project location.

Table 5.3: Results of shifted FLS analysis

SN curve	+ 0.0s	+0.5 s	+ 1.0 s
D	19.64-22.46	15.17-17.53	8.33-9.69
C1	6.23-6.68	3.29-3.57	1.99-2.16
B2	0.41	0.27	0.16

Summarizing, the full analysis showed no strict technical limitations for extending the usage of monopile foundations over the full target water depth range. However, in order to pass all conducted structural checks a substantial amount of steel tonnage is required. The total overall weight increases significantly with respect to today's monopiles which already support 11-13 MW wind turbines. This shows the need of solutions to either extend the technical feasibility of the conventional monopile or the design of a working novel support structure for the target depths with reduced steel usage.

Part 2

6

Alternative Solutions

The results of the technical feasibility analysis for monopile foundations in deep waters showed no technical show-stoppers for the selected reference location and wind turbine, provided that sufficient steel is used. However, as the energy industry is a highly competitive market, it is key to keep energy prices as low as possible. Monopile foundations have been a major contributor to the cost reduction of offshore wind energy over the years. Additionally, with the increasing water depths, the relative share of foundation costs in the overall expenses grows and small cost reductions in the foundation design can thus have a larger impact on the final price of energy.

Figures 4.12 and 4.13 show the total steel usage for the assessed monopile geometries over water depth. The figures show a non-linear increase of required steel mass for an increasing water depth and an increase of required steel mass for increasing first natural frequency. Table 4.3 shows that, the only monopiles passing both the ULS and FLS checks are the stiffest foundations (0.20 Hz). The required stiffness is in direct relation with the high usage of steel, making them relatively more expensive. Since, typically, steel usage reduces for a decreasing first natural frequency, ideally an as low as technically possible first natural frequency is desirable.

This Chapter will propose alternative solutions based on the results of Part 1 of this thesis, which are aimed at bringing down the overall steel usage. Accompanying high level results of the proposed modifications will also be presented in this Chapter. The solutions assessed are listed below:

1. Usage of a higher steel grade
2. Increased (localized) damping
3. Improved weld quality
4. Novel hybrid concept foundation.

6.1. Higher Steel Grade: S420

The monopiles designed for the lowest first natural frequency (0.15 Hz) showed not to be technically feasible at the chosen reference location. Figures 4.8 and 4.11 showed that both ULS checks failed for practically the entire selected target water depth range. Hence, the FLS check was not required to assess the technical feasibility of these monopiles. In order to pass the conducted ULS checks, either the overturning moment resulting from the ultimate wave forcing must reduce or the yield resistance of the selected material must increase. As the reduction of hydrodynamic loading (by perforating the monopile) is a topic under simultaneous investigation for Sif and DOT BV [79], the current study will only focus on the effect of increasing the yielding capacity of the steel. The feasibility of the use of higher grade steel types in the monopile fabrication process is confirmed by Sif [51].

The steel type primarily used in Sif's monopile fabrication process is S355ML of which the wall thickness dependent yield strength properties are listed in Table 4.1. According to Sif [51], the next steel grade applicable to use in the monopile fabrication process is S420 steel, of which the wall thickness dependent yield strength properties are listed in Table 6.1 [21].

Table 6.1: Specified Yield Strength of S420 for different wall thicknesses [21]

Wall thickness [mm]	Yield Stress [MPa]
3 - 50	420
50 - 100	390
100 - 250	365

The ultimate limit state analysis as described in Chapter 4 is re-run while the steel grade is changed from S355ML to S420 for all steel cans. Figures 6.1 and 6.2 show the comparison of ULS results between the two steel types over the target water depth range.

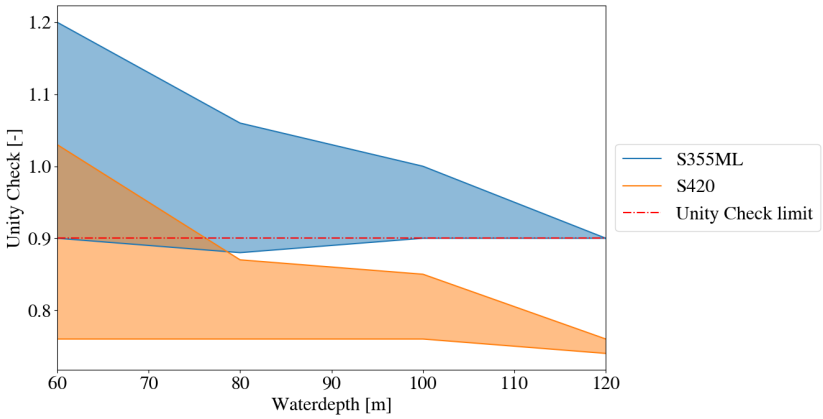

Figure 6.1: Von Mises Stress Unity Check for Different Structural Steel Grades

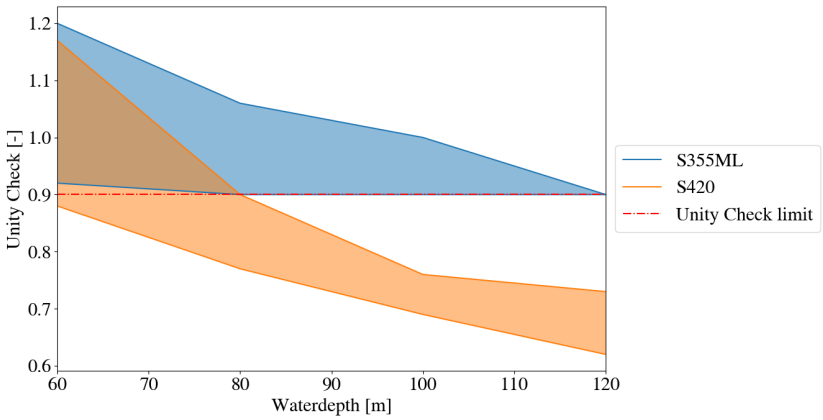

Figure 6.2: Global Buckling Unity Check for Different Structural Steel Grades

The results show that, as expected, the adaption of higher grade steel significantly improves the resistance against ULS failure for the monopiles designed for a 0.15 Hz first natural frequency. The decreasing trend in unity check is a result of the relative increase of monopile length in the total system length. Due to

this increasing share, varying the slenderness of the monopile can be done in a more controlled fashion while keeping the first natural frequency close to the set target frequency.

Typically, designers aim to minimize the usage of higher-grade steel types as their cost per ton is higher. The revised ULS results show that the monopiles have increasing tolerance with respect to the set unity check limit for water depths over 80 meters. This means that for these monopiles, a combination of S355ML and S420 steel plates can be used in order to reduce the overall costs [51].

Since the revised 0.15 Hz target first natural frequency monopiles now pass both ULS checks for the majority of the selected target water depth range, a fatigue limit state analysis for these geometries is required to ensure technical feasibility. The fatigue analysis procedure is explained in Chapter 5. The preceding fatigue analysis results showed that the variation in bending stress response is limited for increasing water depth. However, the response strongly depends on the selected first natural frequency of the system. Figure 6.3 shows the bending stress response to a unit wave of 1 meter for increasing wave frequency and the 3 selected target natural frequencies. The figure shows that the trend of increasing bending stress response for decreasing stiffness also holds for the additional 0.15 Hz stress frequency response function.

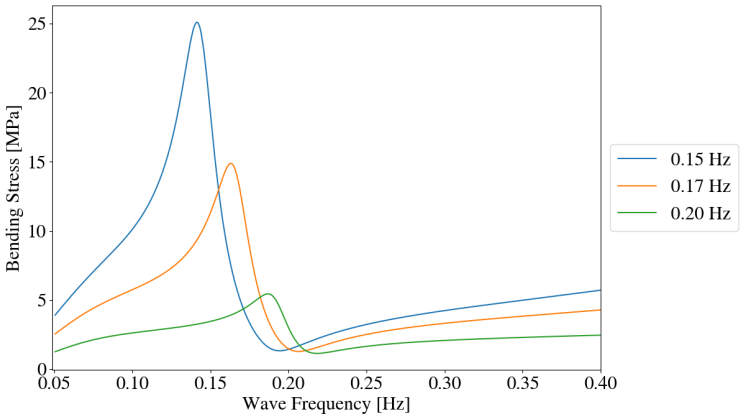

Figure 6.3: Bending Stress Frequency Response Function for Different First Natural Frequencies

The wave scatter diagram shown in Figure 5.8 is used to calculate the accumulated fatigue damage over the design lifetime of 25 years. The accumulated fatigue results for the 0.15 Hz monopiles and three different weld quality S-N curves are shown in Table 6.2

Table 6.2: Results of FLS analysis for 0.15 Hz monopiles

S-N curve	0.15 Hz
D	132.3 - 207.5
C1	54.9 - 68.0
B2	0.96

The results of the fatigue analysis of monopiles designed for a 0.15 Hz first natural frequency show significantly higher accumulated damage than the previous results for higher first natural frequencies as shown in Table 5.2. The monopiles fail the check for both the D-grade S-N curve and the C1-grade S-N curve. Hence, following the DNV standard the monopiles are not resistant against the fatigue damage [22]. For the B2-grade S-N curve, which represents welds with properties comparable to the base material, the fatigue analysis check is just passed.

Following this result it can be be concluded that the adoption of higher grade steel in the design on its own will not serve as a solution for technically feasible monopile foundations with a reduced amount of steel tonnage. Even though, the failure on ultimate limit state loading is avoided, the monopiles still fail severely on the fatigue check.

6.2. Increased (Localized) Damping

Both the ULS and FLS analysis results showed an increasing probability of failure for increasing slenderness of the monopile foundation. The ULS slenderness limit was found to be somewhere between a first natural frequency of 0.15 Hz and 0.17 Hz, whereas the monopiles designed for a 0.17 Hz first natural frequency were neither resistant against the accumulated fatigue damage following the dictated D-class S-N curve, or the higher quality weld C1 S-N curve. The adoption of the higher-grade structural steel type S420 in the monopile design shows to prevent the failure on ULS for a significant part of the selected target water depths of 60-120 meters for the most slender monopiles. Table 6.2, however, shows that the more slender 0.15 Hz target frequency monopiles are less resistant against fatigue damage than the previously assessed 0.17 and 0.20 Hz target frequency monopiles. Two solutions to increase the fatigue lifetime of the more slender monopiles are proposed and evaluated in this and next Section..

Chapter 5 shows that the fatigue lifetime of the monopiles is governed by a variety of external and internal factors. One of the external factors which varies for each project site is the dominant wave states. Table 5.3 shows that the fatigue damage over the design lifetime reduces significantly for a wave period shift of the dominant wave states, underlining the importance of reliable metocean data. However, adapting the monopile to the environment is more realistic than vice versa. Therefore, even though this is a promising finding for expanding the technically feasible locations for the monopile, this external factor can not be seen as a fundamental solution for extending the fatigue life of monopiles. The governing internal factors of the monopile itself were the slenderness of the pile, the total damping in the system and the quality of the crucial fatigue segments, being the welds around the mudline.

The 3 selected target first natural frequencies of the monopile optimization process are set to assess the effect of varying slenderness on the technical feasibility of the monopile in deep waters. Increasing the stiffness (up to first natural frequency of 0.20 Hz) shows to be a technically feasible solutions for the usage of the monopiles over the entire water depth range. However, as this solution requires a significant amount of steel tonnage, the two other remaining main critical factors (overall damping and weld quality) are investigated and used to find a solution to increase the fatigue lifetime. First the damping in the system and its variation will be discussed in this Section and the requirements and effect of higher weld quality will be considered Section 6.3.

The FLS analysis presented in Chapter 5 assumed constant aerodynamic damping over the entire analysis. In reality the aerodynamic damping is a highly variable parameter which depends on a large set of internal and external parameters such as the wind climate, the pitch controller and rotational velocity [81]. Additionally, due to the relatively low inherent damping of cross-wind tower vibrations, the cross-wind vibrations caused by wave loading misaligned by wind can decrease the fatigue life even more [78]. Literature implies that other sources of damping such as structural-, soil- and hydrodynamic damping can be highly uncertain, ranging from an overall damping ratio of 1-3%, which is also variable over time [12]. A way to extend the technical feasibility of the monopile structures is by means of structural control, in which external devices are installed in order to increase the damping and reduce the dynamic response.

The most widely adopted type of structural control of fixed offshore wind turbines in both the industry and literature is the concept of resonant damping [78]. A variety of resonant dampers like a Tuned Liquid Damper (TLD) and Tune Mass Damper (TMD) have shown to lead to a reduction of accumulated fatigue damage over the design life of offshore wind turbines in experiments [13, 15, 52, 67]. Resonant dampers are the most effective when installed at the location where the absolute motion of the targeted vibration mode is the largest. As concluded in Section 5.4, waves at the reference site will only excite the system in its first bending mode. This means that the largest absolute motions will be at the top of the system and the most effective placement location would be either on top or inside the RNA. Even though TMDs and TLDs show to reduce the overall structure response, the increased damping is directly associated with large damper motions and large damper masses. This may result in different complications when installed at the top of a slender wind turbine, as an increase of top mass is highly undesirable [9]. In order to overcome the installation issues, different forms of passive dampers inside of the tower are proposed in literature such as a toggle-brace-damper system or stroke amplifying braces [9, 33].

As the turbine tower is significantly more slender than the monopile itself, the largest absolute motions are centralized in the tower part. Figure 6.4 shows a displacement trajectory induced by an arbitrary full forcing cycle of a fatigue wave. It shows that the trajectory follows a 'fish-tailing' movement, rather than a classic cantilever beam movement. The wave induced vibrations on the foundations are transferred to the turbine tower resulting in a whip-like response with significantly larger displacement in the tower than in the monopile.

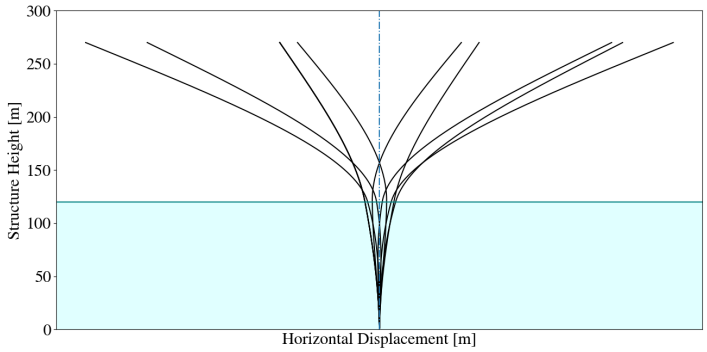

Figure 6.4: Displacement Trajectory During Full Fatigue Wave Cycle

Therefore, the introduction of extra damping to reduce the structural response will be increasingly effective the higher it is localized. To assess the effect of additional damping on the fatigue life, the damping ratio resulting from the horizontal top damping (originally only caused by the aerodynamic damping equal to ~ 8.5% as found in Chapter 5) is increased with steps of 10% and the fatigue analysis is re-run. The damping ratio is defined as the percentage of the critical damping as shown in Equation 6.1.

$$\zeta = \frac{c}{c_{crit}} \tag{6.1}$$

Using this equation, the critical damping of the system can be found. The only introduced damping in the simplified system is the aerodynamic damping which was found to be equal to 2.1e5 Ns/m. Substituting the damping ratio of 8.5% and re-writing the equation gives a critical damping of approximately 2.5e6 Ns/m. Figure 6.5 shows the bending stress response to a unit wave of 1 meter wave height for increasing frequency and different damping ratios. It shows the response curve flattens quickly between the original damping and 20% damping, hereafter the curve still flattens but the increase of damping ratio is less effective. It can be seen from Figure 6.4 that while high damping flattens the stress amplification over the resonance frequencies, it does increase responses at higher frequencies, which means that it will do more damage there than good.

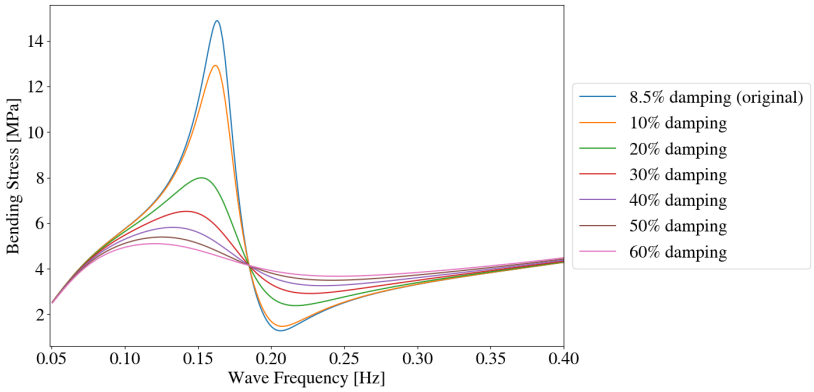

Figure 6.5: Bending Stress Frequency Response Function for Increasing Damping Ratio for the 0.17 Hz Monopiles

With the resulting bending stress frequency response for increasing damping ratio caused by higher horizontal top damping, the resistance against fatigue damage for increasing damping ratio can be assessed. Figure 6.6 shows the resulting fatigue damage for the monopiles designed for a 0.17 Hz target frequency. A sharp decrease of fatigue damage for the C1 and D graded S-N curves up until a damping ratio of approximately 20% is observed. Hereafter, the decrease rate of accumulated fatigue damage slightly decreases. Previous results show that the FLS analysis for the B2 graded S-N curve already passed the unity check for the original damping. The figure shows that a damping ratio of approximately 32% would be required to make the monopile resistant against fatigue following a C1 graded S-N curve, whereas the dictated D graded S-N curve fatigue does not come below the limit line. This implies that the 0.15 Hz monopiles are not resistant against fatigue damage, even with much flattened dynamic amplification. The assessed range of damping already exceeds the amount of expected technically feasible damping and thus it is concluded that the additional top damping will not result in fatigue resistant monopile designs following the D graded S-N curve.

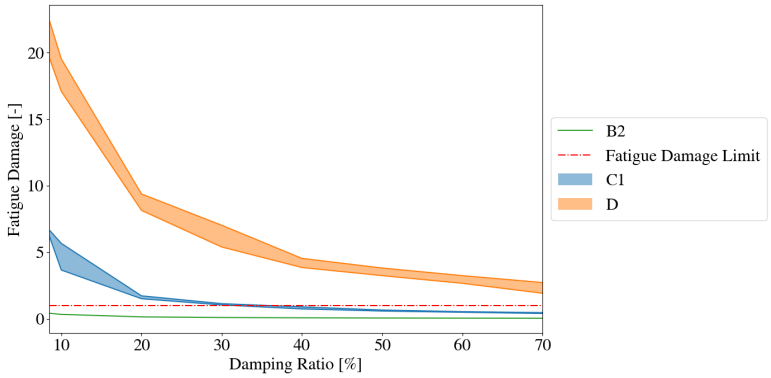

Figure 6.6: Accumulated Fatigue Damage for Increasing Damping Ratio for Different Grades S-N Curves

Literature shows modified Tuned Mass Dampers with damping ratios up to 30% [61]. Dampers with this magnitude of damping along with the additional aerodynamic- and residual damping would yield fatigue resistant monopiles designs against the C1 graded S-N curve for the monopiles designed for a 0.17 Hz first natural frequency. However, the resulting increase in top mass due to the installation of a damper will affect the first natural frequency of the system. As the reference turbine tower is not designed for this mass, its dimensions would have to be increased in order to ensure structural integrity. Increasing the overall dimensions and thus the mass and stiffness of the turbine tower also strongly affects the resulting natural frequency, dynamic behaviour and bending moment at the mudline. The design of the turbine tower and its connection to the monopile is not considered in this thesis. Even without the additional top mass the bending stress resulting from the curvature in the turbine tower will increase for increasing water depth, this might cause a required increase of stiffness which will, again, strongly affect the dynamic behavior. To ensure the technical feasibility of XL wind turbines in deep water the structural integrity against both ultimate and fatigue limit state is a highly important topic and is therefore a strong recommendation for further research. An estimate on the estimated accumulated fatigue damage is given Appendix C.

6.3. Improved Weld Quality

Even though the upgrade of steel type from S355ML to S420 as proposed in Section 6.1 enables the most slender monopiles of the assessed first natural frequency range to pass the ULS check, Table 6.2 shows that they fail the FLS check for the code recommended S-N curve. Recently a lot of research has been done or is currently ongoing on the validity of the dictated S-N curves. Research that compares experimental results with the dictated S-N curves suggests that the curves can be very conservative in specific situations [**?**]. Additionally, the DNV code states a so called 'thickness effect' for circumferential welds, which is the weld type present in the monopiles [22]. A joint interdisciplinary research project including the University of Stuttgart and Dillinger is currently aiming to include the reassessed S-N curves in the revised Eurocodes, (roughly) expected to be released in 2024 [18]. This Section will elaborate on the thickness effect and assess its impact on the technical feasibility of the monopiles. Hereafter, the possibility and effects of adopting higher class S-N curves is discussed in more detail.

6.3.1. Thickness Effect

A vast amount of experimental investigation show that, in general, the fatigue resistance decreases with increased size of specimens. This phenomenon, called the *thickness effect* or *size effect*, is observed for both machined and welded specimens [63]. Typically, this effect is accounted for by a correction factor. In this thesis this is done via the thickness effect factor given by Equation 5.12. The thickness effect is considered to consists of 3 sub-effects listed below. Each sub-effect will be explained separately.

1. Geometric size effect
2. Statistical size effect
3. Technological size effect

The *geometric size effect* accounts for two issues that worsen the fatigue resistance for thicker plates. Firstly, when a joint becomes thinner the stress gradient will become steeper as visualized in Figure 6.7. This means that $t_1 < t_2$ will result in $\sigma_1 < \sigma_2$ for an equal nominal stress. Secondly, the scale of the weld toe will not scale linearly with the increasing plate thickness. It could be stated that the radius of the weld toe will remain constant regardless of the size of the joint plates. Therefore, a thicker joint will result in a smaller toe radius to plate thickness ratio and the concentration of stress on the joint will increase.

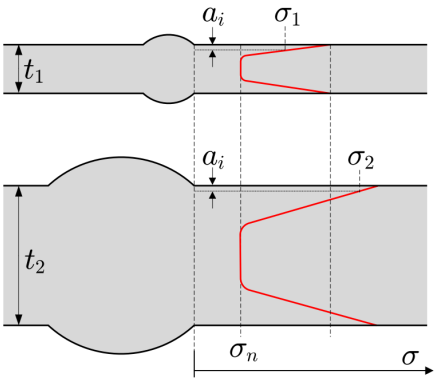

Figure 6.7: Geometric Size Effect [14]

The *statistical size effect* refers to the larger probability of a crucial defect in a larger volume of mass. For welded joints this sub-effect is governed by the length of the weld.

The *technological size effect* accounts for the change in manufacturing conditions when increasing the size of the structures, for example, the requirement of multiple weld passes compared to a single pass or a few passes. It also refers to the difference in residual stress, surface roughness and micro-structure [38].

The analysis of the most relevant experimental results showed very low thickness dependency, with thickness correction exponents of $k = 0.01$ whereas the correction exponents of the C1 and D curve are $k = 0.10$ and $k = 0.20$ respectively (Table 5.1). When the suggested conservative correction exponents are set to zero, the accumulated fatigue following C1 and D graded S-N curves significantly decreases. As the B2 graded curve is already independent of wall thickness, the damage for this curve will remain unchanged.

Figure 6.8 shows the FLS results for the 0.17 Hz monopiles along with the reduced thickness effect results. As expected, ignoring the thickness effect impacts the fatigue damage following the D curve the most (due to its higher original correction exponent). Even though the accumulated fatigue is significantly reduced, the result does not directly lead to fatigue resistant monopiles for the dictated D curve. For the C1 graded curve an additional 11.5% damping ratio is required to pass the check. The before-mentioned joint research project plans on investigating the thickness effect for thick walled plates. As the current standards are calibrated on a plate thickness of 35 mm [22], which significantly differs from wall thicknesses present in modern day monopile designs.

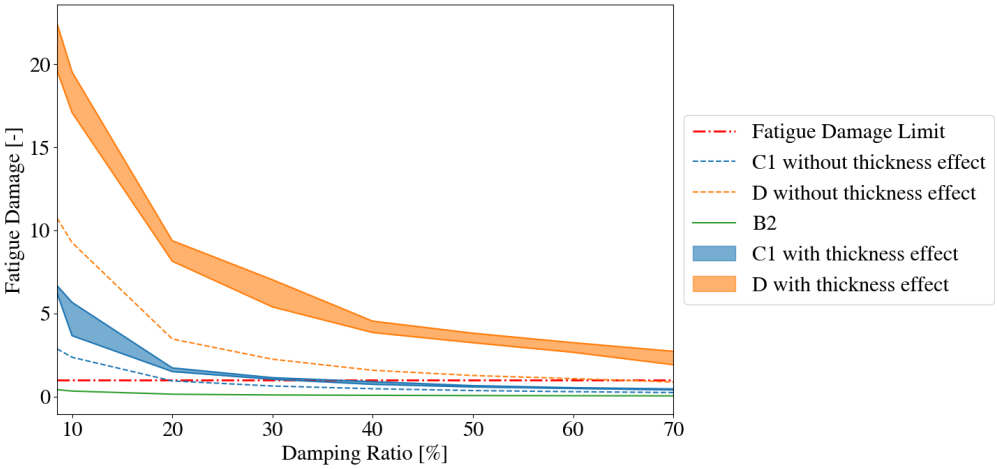

Figure 6.8: Reduced Thickness Effect

6.3.2. Higher Grade S-N Curve

Currently the status quo of dictated S-N curves following standards reads the use of the D-grade S-N curves for regular butt weld circumferential welds, as used in the monopile fabrication process. Analysis of experimental data compared to the D-grade S-N curve confirms that this status quo is approximately correct [**?**].

The weld toes that develop during the welding process cause a concentration of stress. To reduce this stress concentration, the fabricator can grind the welds to plate level if required. Following the standards, this allows the designer to increase the S-N curve grade from D to C1 graded S-N curves. Figure 6.8 shows that this already has a significant impact on the fatigue life.

The comparison of experimental fatigue data for steel specimens in air with the C1 graded S-N curve, however, suggests that this curve grade is very conservative. Figure 6.9 shows the characteristic S-N curve, which is the C1 curve, and the best fitted line for slope parameters $m = 3$ and $m = 5$. The results from this research suggest that the so called FAT class (which is the name convention in the Eurocode) could increase from 127 to 171 [**?**]. This is equivalent to an increase from C1 to B2 graded S-N curve following the DNV code [22]. As this research is conducted for steel in air, whereas the monopiles follow the S-N curves for steel in seawater with cathodic protection, additional research is required to verify this trend in these conditions.

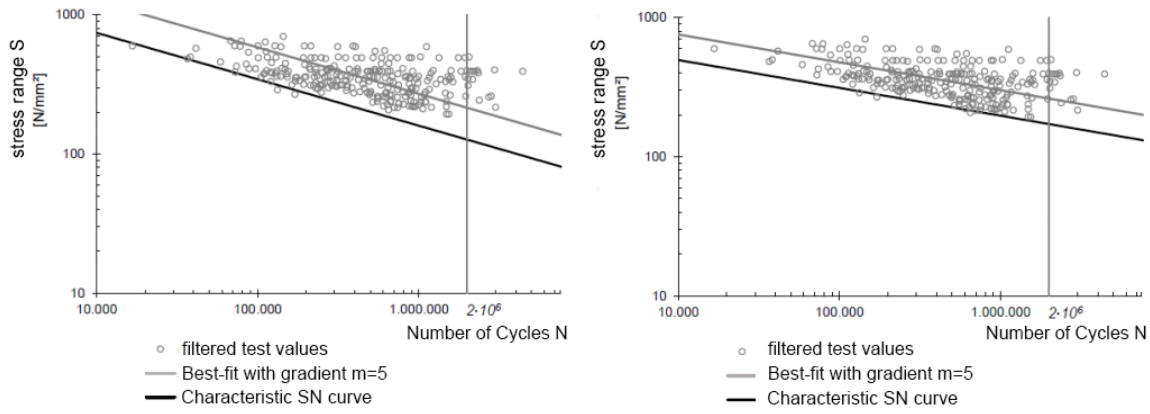

Figure 6.9: Experimental Fatigue Data versus C1 S-N Curve in Air

It is expected that the revised Eurocode, which are likely to be released around 2024, will adopt a new look on the dictated S-N curves [18]. If it is proven and standardized that the fatigue class can be upgraded to B2 graded welds, Table 5.2 shows that the 0.17 Hz monopiles will be resistant against fatigue for the given conditions. This will lead to an overall steel reduction with respect to the monopiles found to be technically feasible up until now over water depth as shown by Figure 6.10. It shows a wide spread of potential mass reduction, strongly dependent on the soil type.

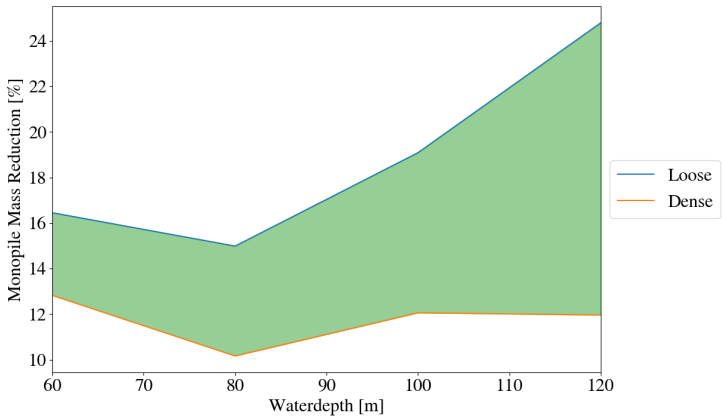

Figure 6.10: Total Mass Reduction of 0.17 Hz Monopiles with respect to 0.20 Hz Monopiles Using B2 Graded S-N Curve

Table 6.2 suggests that the monopiles optimized for a 0.15 Hz first natural frequency also just pass the FLS check using a B2 graded S-N curve. Hence, when the higher grade steel as explained in Section 6.1 is combined with the B2 graded S-N curve, even higher steel reductions can be achieved. Figure 6.11 shows this reduction in overall steel usage for the 0.15 Hz monopiles. Due to the sharp increase of required mass as seen in Figure 4.12, the relative percentage of the monopiles optimized for loose soil grows significantly and up to 35% steel reduction can be achieved in 120 meter water depths.

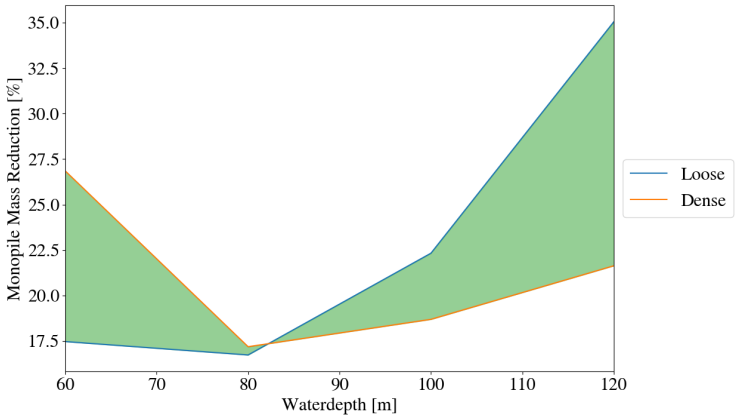

Figure 6.11: Total Mass Reduction of 0.15 Hz Monopiles with respect to 0.20 Hz Monopiles Using B2 Graded S-N Curve

6.4. Hybrid Novel Concept

The solutions to expand the technical and herewith financial feasibility of the monopile as assessed in this Chapter thus far focused on critical parameters in the system without modifying the fundamental working principle of the monopile foundation concept. Even without modifications, no technical limitations were found for the conventional monopile in the target water depth range, provided that enough steel is used. Additionally, the required steel usage can potentially be reduced with earlier proposed solutions. However, it cannot be ruled out that one or several aspects still limits the use of monopiles in deep water. Therefore, a new foundation concept is developed that addresses the most likely limiting factors, namely the crucial bending moment at or below the mudline (or in the turbine tower) and the accumulated fatigue damage at the mudline. This foundation concept combines the main benefits of the monopile (manufacturability and installability for the assessed water depth range) with the developed knowledge on floating support structures aiming to reduce overall steel usage.

Currently, many researches strive to find a solution to capture the high quality wind potential of deep waters. The ongoing developments in the offshore floating wind industry has resulted in numerous floating support structure concepts, with a strongly varying Technical Readiness Level (TRL). The prototype test sites of the Hywind project showed promising results for SPAR-type structures. Whereas semi-submersible type based floating support structures have also seen great acceleration in development. However, as discussed in Section 1.4, floating support structures are currently relatively costly and will start becoming increasingly financially attractive for water depths beyond the assessed target range. Additionally, the installation of SPAR-type concepts require significant free draft, also reaching beyond the target water depth range assessed in this thesis. The mooring of semi submersible based concepts is very challenging in water depths up to 100/120 meters due to the required horizontal spacing of the mooring lines. The proposed concept aims at omitting the latter issue by replacing the mooring lines with a monopile-based foundation.

6.4.1. Concept Description

To accelerate the development of floating wind structures, the International Energy Agency (IEA) provided an accompanying reference floating support structure developed by UMaine along with the chosen 15 MW reference turbine [2]. Figure 6.12 shows a render of the turbine and floating foundation. The dimensions and adopted reference coordinate system are given in Appendix B and the main semi-submersible properties are listed in Table B.1

Table 6.3: Semi Submersible Platform Properties [2]

Parameter	Value	Units
Hull Displacement	20,206	m^3
Hull Steel Mass	3,914	t
Tower Interface Mass	100	t
Ballast Mass (Fixed/Fluid)	2,540/11,300	t
Draft	20	m
Freeboard	15	m
Vertical COG from SWL	-14.94	m
Vertical COB from SWL	-13.63	m
Roll Inertia about COG	1.251E+10	kg-m^2
Pitch Inertia about COG	1.251E+10	kg-m^2
Yaw Inertia about COG	2.367E+10	kg-m^2

Figure 6.12: The UMaine VolturnUS-S Reference Platform Designed to Support the IEA-15-240 OWT System Definition. [2]

The idea of the presented novel concept is to replace the catenary mooring system as shown Figure 6.12 with a monopile and universal joint. A universal joint is a type of hinge that is free to rotate in two degrees of freedom (in this case pitch and roll) and transmits a moment in the third rotational degree of freedom (yaw) [8]. Additionally, all translational displacements (surge, sway and heave) are restricted at the joint. This way, the mooring of the floating support structure does not require any horizontal spacing. The increased dimensions of the platform close to the waterline with respect to the conventional monopile result in a larger hydrodynamic forcing and thus an increase of shear force acting on the joint. However, as all forcing will be transferred to the monopile through the joint, locating the joint closer to the virtual fixation point will reduce the arm and thus the overturning moment. Additionally, lowering the location of the joint allows for horizontal movement and acceleration of the top part. Following Newton's second law (force = mass x acceleration [49]), an inertial horizontal forcing component arises. The magnitude of this forcing component depends on the total mass (+ added mass) and acceleration, the latter in turn being dependent on the vertical location of the joint. In order to achieve a reduction of forcing, a suitable balance between these forcing components must be found.

The freedom in pitch and roll direction will cause an extra restoring moment due to the growing buoyancy for larger pitching angles. Power production of a wind turbine is related to the angle between the in-flow of the wind an the rotor plane. This angle, in turn, is dependent on the pitch angle of the floater. Turbine efficiency is expected to significantly reduce for pitch angles greater than 10 degrees [87]. To minimize the effect of the pitch angle on the power production, the maximum allowed dynamic oscillation pitch during operation is set at 10°. A visualization of the proposed hybrid concept is given in Figure 6.13.

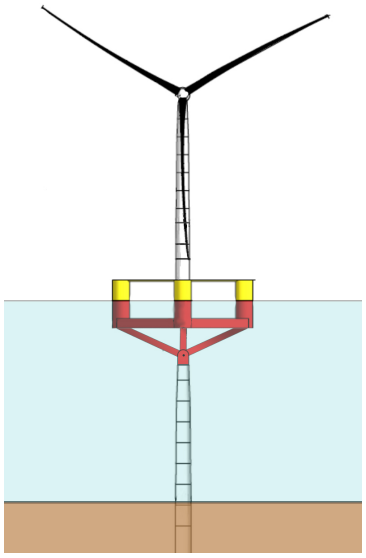

Figure 6.13: Novel Hybrid Floating-Fixed Bottom Concept

6.4.2. Reproduction of Reference Platform

The novel hybrid concept is a complex system, involving aerodynamics, hydrodynamics, ship hydro-mechanics and structural dynamics. Such a complex system can only be effectively analysed using a FEA simulation suite. There are several software suites available that can be used for analysing floating/hybrid offshore wind turbines such as OpenFAST and OrcaWave/Orcaflex. However, the ANSYS suite is the only software that is accessible for the TU Delft students via academic license. Therefore, ANSYS AQWA is used to simulate the semi-like platform. Prior to application of the developed FEA model to the selected hybrid concept, the semi-submersible (catenary moored) model is validated and verified against a well-documented and reliable reference model, as published by NREL and the University of Maine [2].

The reference model was analysed using a different software package, namely, OpenFAST's hydrodynamics module, HydroDyn. Frequency-dependent coefficients for the potential flow model were computed using the boundary-element-method hydrodynamics solver WAMIT v6, which solves the first-order hydro statics, diffraction, and radiation problems, and then uses the resulting response amplitude operators (RAOs) to compute second-order wave-excitation quadratic transfer functions (QTFs).

Following the selected software package route, the reference platform is modelled in accordance with the provided reference document. The geometry of the floater is developed using the ANSYS DesignModeler and imported to ANSYS AQWA. Point masses with corresponding inertia properties were added to simulate the mass of the turbine tower, RNA and floater. Typically, floating offshore wind turbine towers have higher stiffness requirements than fixed-bottom configurations because of the increased inertial and gravity loads resulting from platform motions [2]. The total reference floating turbine tower mass is 1,263 t, which is a significant increase with respect to the tower mass of the original reference turbine (860 t). For this analysis, the stiffer tower is adopted.

A diffraction analysis adopting the 3D panel method is conducted in ANSYS AQWA which can be used to solve linearized-potential-flow hydrodynamic radiation and diffraction problems in the frequency domain. This analysis is used to compare the added mass and damping matrix between the AQWA model and the reference document. The maximum allowed frequency (0.368 Hz) during the analysis is governed by the mesh properties. As the main wave forcing components are already captured before this frequency, the limit is considered sufficient for this research. Figures 6.14 and 6.15 show that the comparison of added mass and damping force entries is in good agreement with the reference floater and the modelling technique is considered valid. In the presented RAOs the directional convention is as follows: 11, 22, 33, 44 ,55, 66 = Surge, Sway, Heave, Roll, Pitch, Yaw.

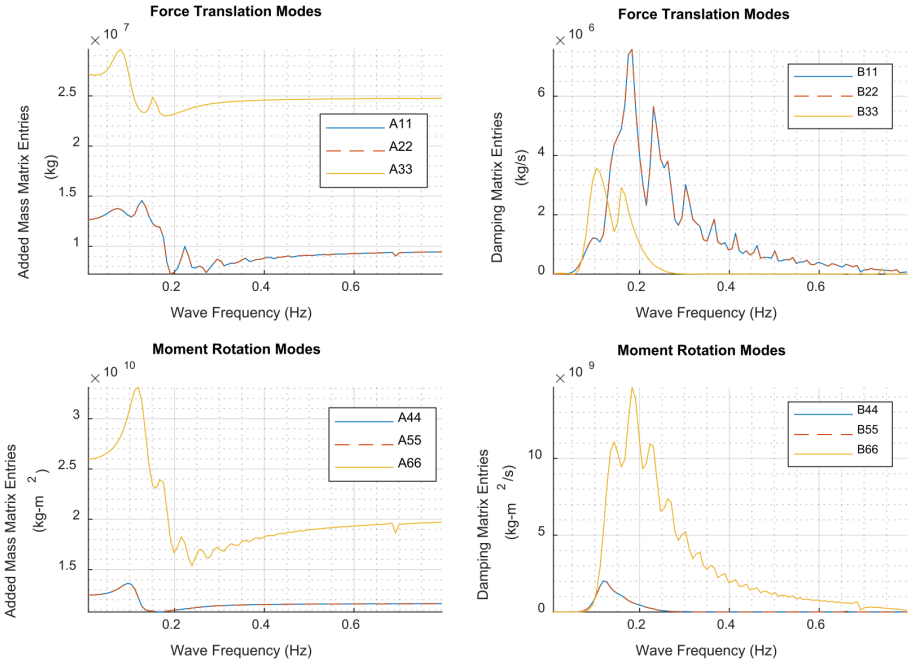

Figure 6.14: Added Mass and Damping Matrix Entries, UMaine Reference [2]

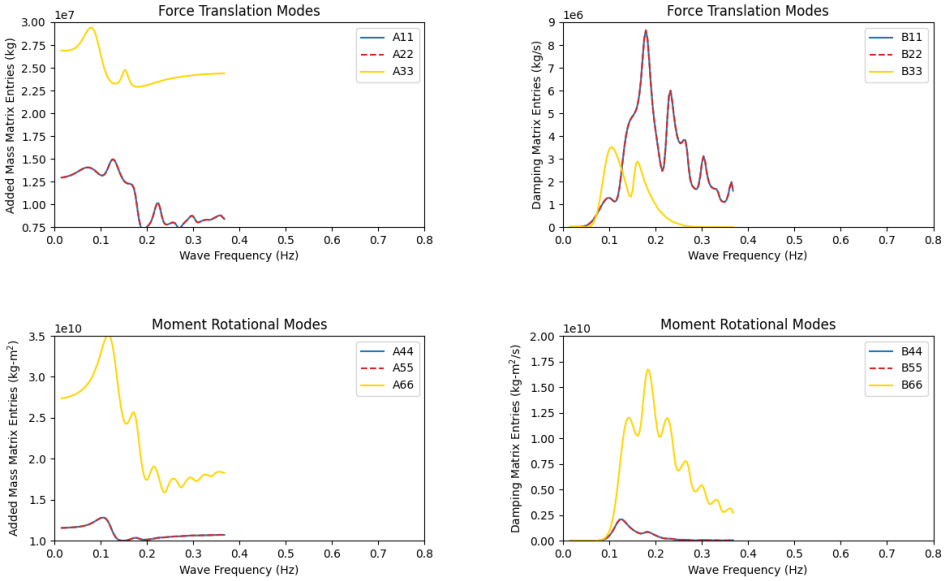

Figure 6.15: Added Mass and Damping Matrix Entries, AQWA Output

Subsequently, the hydrodynamic diffraction analysis results including the added mass, damping and quadratic transfer function (QTF) matrices are transferred to the time domain in order to assess the hydrodynamic response. The reference floater is moored to the seabed at a water depth of 200 meter using a 3-chain catenary mooring system. The detailed mooring properties and arrangement are provided in Appendix B and reproduced in AQWA. In naval architecture, the viscous damping (not accounted for in potential flow theory) is typically a large component of the total hydrodynamic damping of the system [**?**]. In the reference document, the viscous damping is accounted for by introducing an additional viscous damping matrix calculated in the CFD software openFOAM. As this software was not available (and known to the student), for this research the quadratic (viscous) damping was approximated by the addition of carefully selected cylindrical flooded Morison drag elements to the system. Damping ratio analysis of the free decay motions of the floater shows satisfying resemblance to the reference results.

To validate the damped hydrodynamic response of the system in the time domain, one translational (heave) and one rotational (pitch) RAO are compared with the reference document for a wave height of 1 and 8 meter. The selected Airy wave theory in AQWA does not allow for unrealistic (too steep) waves, which leads to RAOs over a smaller frequency range. Figures 6.16 and 6.17 show that the RAO shapes are very similar with the resonance peaks at the approximate same frequency. The magnitude of the response at resonance is, however, over-estimated by the AQWA model especially for the 1 meter amplitude waves. As these excitation frequencies are not present in the wave climate, the model is assumed to be fit for use in this research.

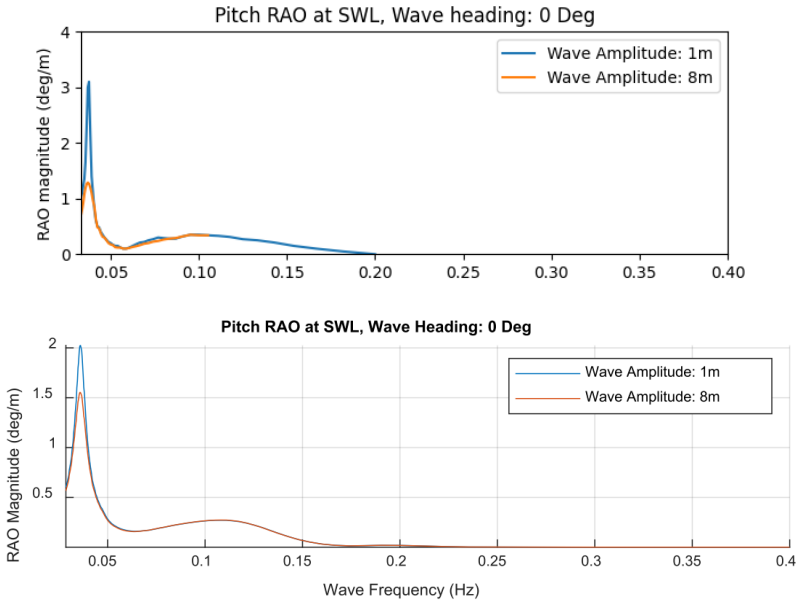

Figure 6.16: Damped Pitch RAO Comparison between AQWA (top) and reference (bottom)

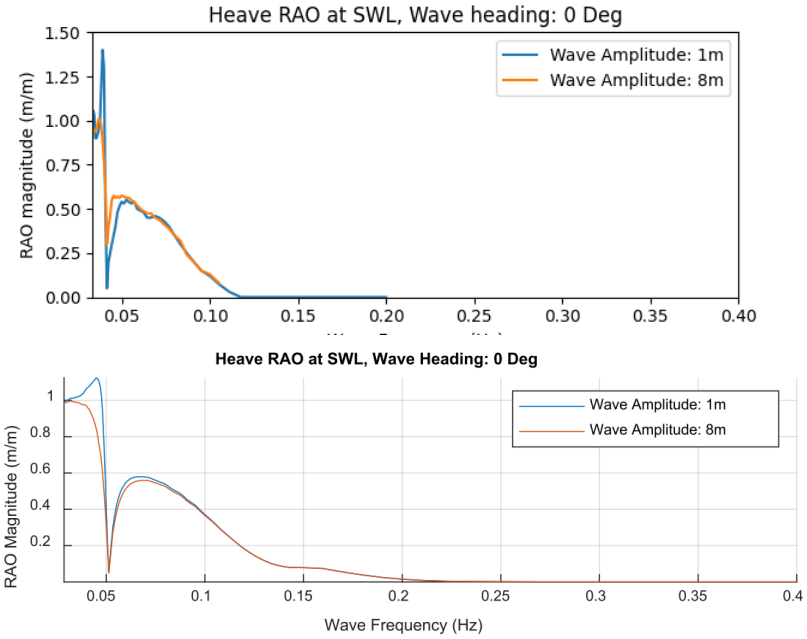

Figure 6.17: Damped Heave RAO Comparison between AQWA (top) and reference (bottom)

6.4.3. Vertical Hinge Location

The hybrid concept is tested on the same load cases (rated and parked) as the conventional monopile, with the environmental data given in Table 2.1. ANSYS AQWA is used to extract vertical and horizontal force reactions at the universal joint during these load cases. As discussed in sub-section 6.4.1, the possible reduction of forcing of the hybrid concept strongly depends on the vertical location of the universal joint. Additionally, the resulting stress in the monopile is a combination of the induced axial stress and bending stress resulting from the vertical and horizontal force component at the joint respectively. Figure 6.18 shows the absolute maximum horizontal and vertical forcing amplitude at the universal joint for an increasing hinge depth during ULS conditions. It shows a sharp linear decrease of maximum horizontal forcing amplitude, whilst the vertical forcing component increases.

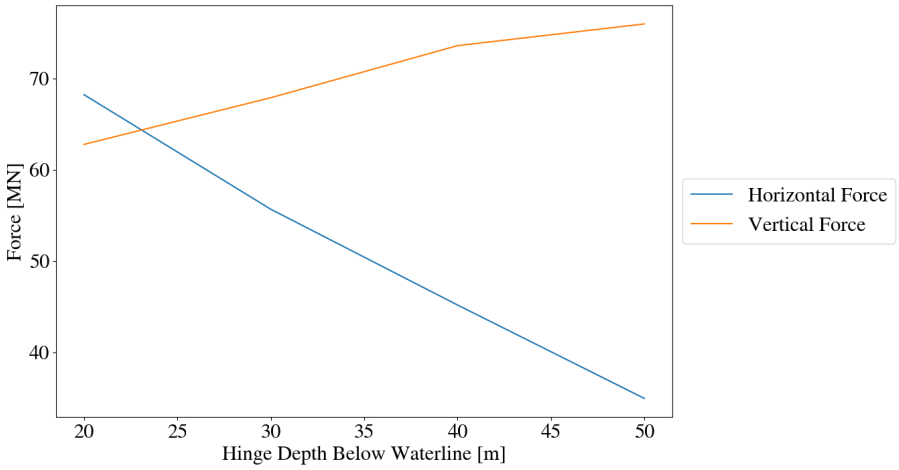

Figure 6.18: Horizontal and Vertical Hinge Force Response for Increasing Hinge Depth

Figure 6.19 shows time series of the pitch response of the reference semi-sub moored with catenary mooring lines and a set of hinged configurations during rated conditions. Too make sure that transient effect from the start-up of the motions is not present in the time series, a sufficiently long time range is chosen. It shows that the static pitch angle resulting from the thrust force increases for increasing hinge depth, but stays within the stated limits. Therefore, the pitch angle will not be a show stopper for this concept. Additionally, the pitch fluctuation is small, suggesting a stable power production.

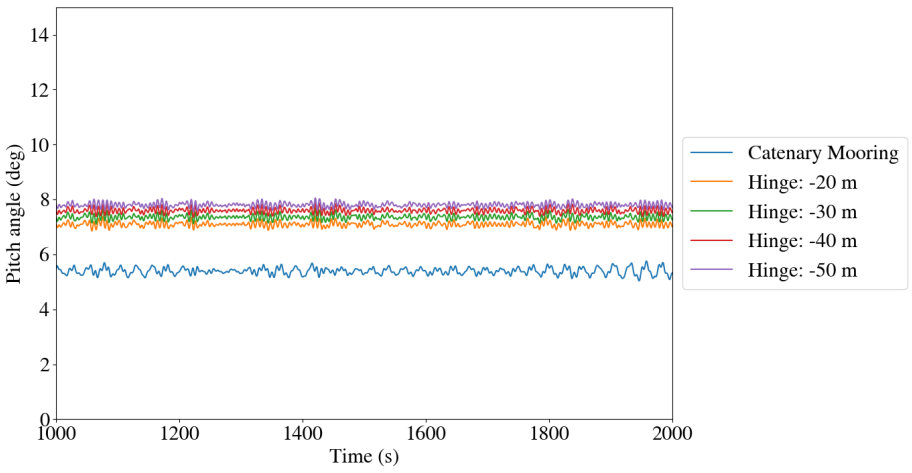

Figure 6.19: Pitch Response Comparison for Different Mooring Configurations

The monopiles designed for a 0.15 Hz target frequency and water depth of 60 and 120 meters (which previously failed the ULS and FLS checks) are adopted and the forcing components are transferred to stress components at the virtual fixation point. Figure 6.20 shows the stress response for 0.15 Hz target frequency monopiles in loose soil for 60 (top) and 120 (bottom) meter water depths with a hinge at 50 meter below the waterline during ULS conditions. It is concluded that, even though, a phase shift is observed for the 60 meter water depth monopile, the ULS check is (again) governed by the bending stress. When the hinge depth is decreased, the horizontal forcing component and the moment arm will increase and thus the bending stress will become even more dominant.

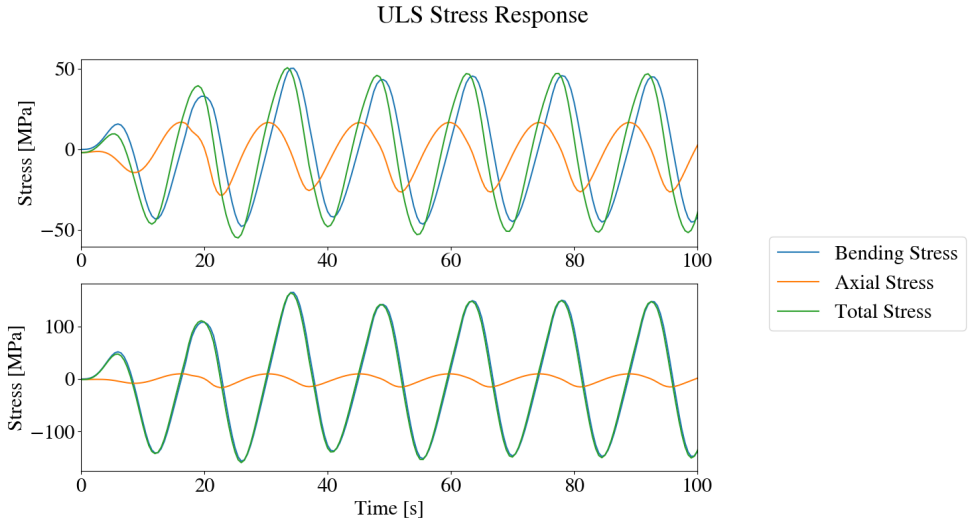

Figure 6.20: ULS Response of 0.15 Hz Target Frequency Monopiles with a Hinge 50 m Below the Waterline in 60 (Top) and 120 (Bottom) m Water Depth

To select a suitable joint depth, the vertical location of this hinge is varied between 20 and 50 meter below the waterline for the assessed monopiles, while keeping the same geometry below this depth. A deeper vertical hinge location is not assessed as it will diverge too far from the original concept. The resulting Von Mises stress during ULS is determined in a similar fashion to the conventional monopile design and compared with the initial results. Figure 6.21 clearly shows the increasing reduction of the maximum resulting Von Mises stress for increasing hinge depth. It also shows that the concept is more effective in shallower water depths due to the relatively larger reduction of forcing arm.

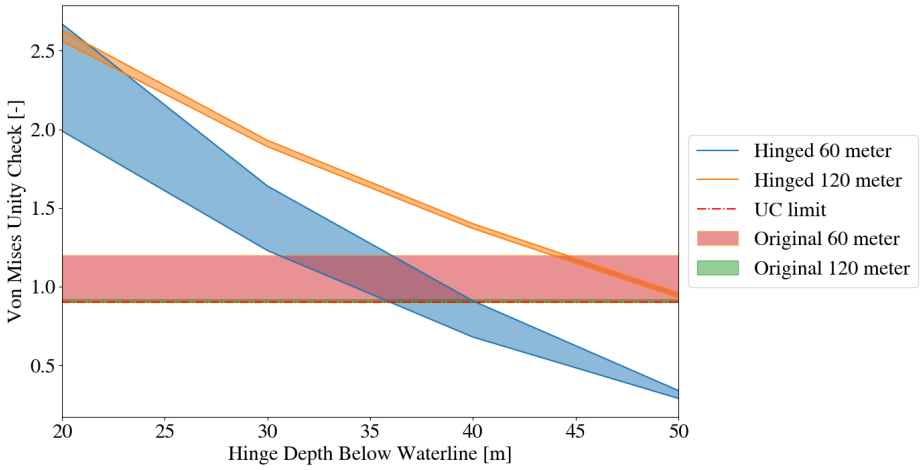

Figure 6.21: Von Mises Unity Check for Varying Hinge Depth and Water Depth

6.4.4. Steel Reduction

For the assessment of the potential steel reduction, a hinge depth of 50 meters below the waterline is adopted (being the most effective location). For this configuration the forces during ULS are extracted and the monopile design optimization tool is used to optimize the monopiles against the resulting stress. As the natural frequency of the system becomes very complex to determine analytically, this criterion is omitted. However, it is not expected that the new configuration will lead to a natural frequency that interferes with the present wave frequencies. The semi-sub has natural frequencies far below the wave excitation frequencies, whereas the shorter monopiles have a higher first natural frequency than the present wave frequencies. Figure 6.22 shows the total mass of the optimized monopiles with and without the reference platform steel mass (3,914 t). As expected, the monopiles use less steel which is partly due to the reduction of forcing in shallower water depths, but also largely due to the fact that they are simply shorter.

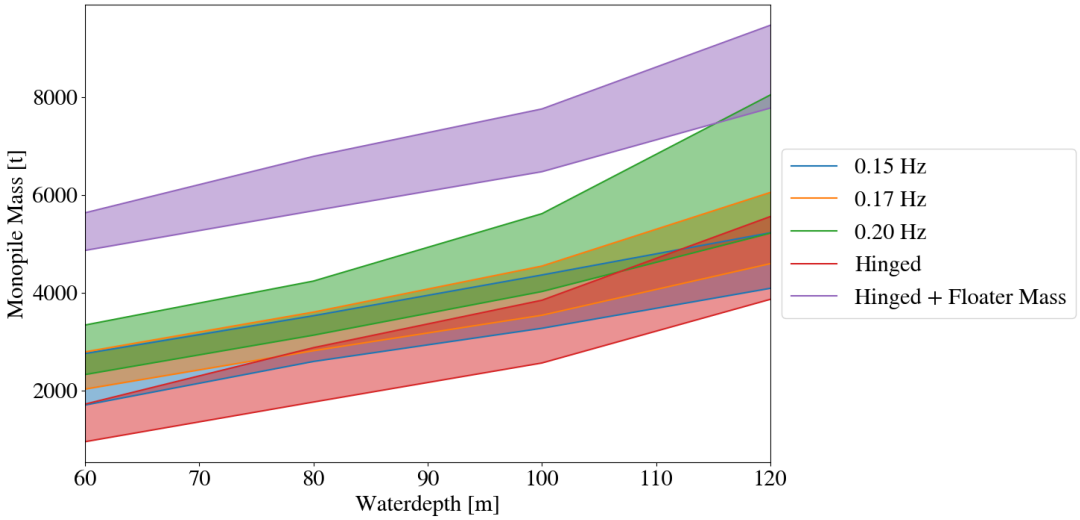

Figure 6.22: Total Monopile Mass Compared with Previous Results

The optimization and thus the required steel mass of the top part is not included in this study. It is expected that steel reduction is possible here, as the 'pontoons' that damp the heave motion are not required any more due to the restriction of movement in this direction. This optimization is a recommendation for further research. However, the current results suggest that it is difficult to achieve steel reduction with this concept with respect to the conventional monopile.

6.4.5. FLS Analysis

To complete the high level analysis of technical feasibility of the novel concept, the optimized monopiles are tested on their fatigue resistance. As the to-be-displaced volume around the waterline acted on by the fatigue inducing waves has increased with respect to conventional monopiles, the inertia component of the forcing becomes even more dominant. For all wave periods present in the wave scatter diagram (as presented in Figure 5.8), the forcing is extracted for a unit wave height and corresponding stress cycles are calculated. As the forcing is fully inertia dominated, the resulting force magnitude scales linearly with wave height and the resulting bending stress cycles can be determined for all wave states in the diagram.

AQWA does not allow for the introduction of local aerodynamic top damping to the system. However, to account for the aerodynamic damping, rotational damping to the joint equal to the aerodynamic damping multiplied by the arm between the RNA and the joint is added. This is under the assumption that the tower is rigid. As the system's natural frequencies are not close to the excitation frequencies, the motions are not dynamically amplified and the damping doesn't have much effect on the motions.

Similar to the conventional monopile FLS analysis, the fatigue over the 25-year design lifetime of the optimized conceptual monopiles is tested against a B2, C1 and D S-N curve. Figure 6.23 shows the accumulated fatigue damage in the monopiles for the proposed concept. It shows that similar to the conventional monopiles, the fatigue damage is practically depth independent. Although the fatigue damage is reduced with respect to the conventional designs that failed on FLS, the suggested C1 or D S-N curve still lead to a failure of the FLS check. The adoption of higher weld quality, however, would lead to technically feasible designs.

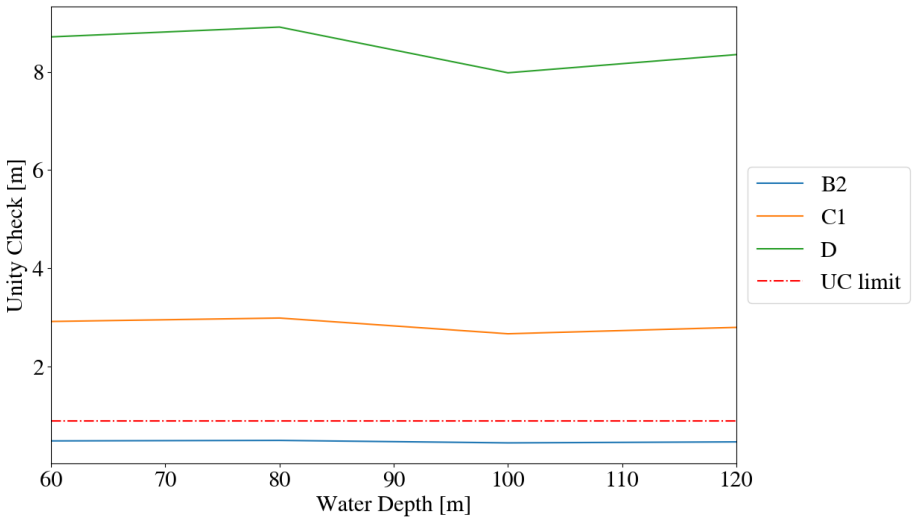

Figure 6.23: FLS Unity Check for the Optimized Monopiles

It must be noted that due to the more complex geometry of the proposed concept, it is possible that the monopile will not be the critical fatigue component of the system. A full fatigue damage assessment of the top side is recommended after optimization of the floater.

7

Conclusions and Recommendations

In this Chapter the main conclusions drawn from the conducted research are presented. Hereafter, limitations of the analyses are discussed and recommendations for future research are made.

7.1. Conclusions

Since the introduction of the first offshore wind farm in October 1991 the demand for offshore renewable wind energy has experienced exponential growth all around the world. To supply this demand, the power rating and corresponding dimensions of offshore wind turbines have grown significantly. Due to the ever-shrinking availability of easily accessible shallow water sites and the abundance of high quality wind resources in deeper water, the industry is stimulated to come up with innovative, yet cost effective, solutions to tap into these deep water sites. Where floating and jacket support structures are either difficult to install or expensive in water depths up to 120 meters, the historically most cost effective support structure, the monopile, has never been evaluated for these depths. This study is structured and conducted to address the research questions laid down in Section 1.6 with the following key objective:

"Investigate the technical feasibility of monopile foundations in water depths of 60 to 120 meters for large wind turbines and determine the critical design parameters for further upscaling."

The paramount conclusion of the conducted analyses is that **no** technical show-stoppers were found to use monopiles to support a 15 MW wind turbine in water depths up to 120 meters at the selected reference site, provided enough steel is used. Strategies to reduce this steel usage showed great potential and the industry already shows intentions to include some of the proposed solutions into the industry practice

Throughout this thesis, the crucial design parameter is the slenderness of the monopile, assessed by a range of 3 target first natural frequencies. All monopile designs were within manufacturing limits. However, for the stiffest (0.20 Hz) monopiles the limits were reached and up-scaling to deeper waters is not possible. The slenderness not only governs the ULS check, but also the FLS check from the magnitude of resulting bending stress and more importantly, encroaching of the structural resonant frequency into the frequency region of most recurring waves.

The overall design-driving ULS load case is dominated by the inertia force resulting from the ultimate wave during parked conditions. Generally, waves grow higher and longer in deeper waters due to reduced bottom interaction and open fetch, driving up the ultimate forces. The slenderness limit of the monopile for the reference site is found somewhere between a 0.15 and 0.17 Hz first natural frequency. The monopiles designed for a 0.15 Hz target frequency fail the ULS checks, whereas the ones designed for 0.17 Hz do not. As the reference location is considered to have a very severe wave climate, the ULS results are conservative for deep water locations with milder wave climate. At these locations the monopiles require less steel to survive this load case. The soil type has a strong impact on the first natural frequency and required penetration depth (and thus overall monopile mass), but showed limited effect on the maximum overturning moment. Adopting a higher grade steel (S420) in the monopile design allows 0.15 Hz monopiles to pass the ULS check for target depths of 80 to 120 m.

Also the fatigue damage is governed by the slenderness of the monopile. Both the monopiles designed for 0.15 and 0.17 Hz fail the FLS check, while the 0.20 Hz monopiles passes the check comfortably with UCs lower than 0.25. The lower resistance against fatigue damage for larger slenderness does not only result from higher bending stress cycles due to smaller dimensions, but also due to the increasing interference with occurring wave frequencies causing resonance. As operational loading showed limited fatigue damage, it is concluded that inertial wave forcing-induced bending stress cycles cause most of the fatigue damage. It is found that the total inertial wave forcing is independent of the wave frequency as the increasing force amplitude is cancelled out by the decreasing influence depth for increasing frequencies. Likewise, the accumulated fatigue damage showed to be independent of the water depth as the increase of required structural steel neutralizes the increase of overturning moment.

As expected, the system is shown to respond highly dynamically to waves near the first natural frequency. It is observed that the system behaves somewhat differently from a conventional cantilevered beam with an end mass, mainly in 2 aspects: 1. the tower section is significantly more slender than the heavily strengthened foundation monopile and 2. the hydrodynamic forcing acts on the monopile (rather than on the top of the "cantilevered beam"). The wave-induced motions of the monopile are transferred to the turbine tower/RNA, which in turn transmits a whip-like "amplified" motion back to the foundation, causing a high stress on the pile base and a complex dynamic interaction between the tower and foundation pile.

The fatigue damage strongly depends on the dominant wave states and most importantly wave periods and is thus also highly site-dependent. Due to the operating frequencies of the large turbine, the soft-stiff region (where the target frequencies are) is located within the exciting wave frequencies and resonance is inevitable. The chosen reference site is somewhat sheltered from the Atlantic by Scottish land mass, which results in shorter waves compared to open oceans. These wave frequencies interfere more heavily with the first natural frequency of the system, which makes this reference site relatively conservative with respect to many other more open sea locations. In the fatigue analysis only the aerodynamic damping is included, neglecting structural, hydrodynamic and soil damping. The increase of damping ratio alone, however, does not yield additional technically feasible solutions.

Only the stiffest and thus heaviest monopiles designed for a 0.20 Hz first natural frequency passed all conducted checks. To bring down the steel usage and herewith the costs, the effect of increasing the weld quality and higher steel grade is assessed. Thanks to the rapid technical and manufacturing advancements, the use of the B2 grade S-N curve may become an accepted industry practice in the near future, which would make the monopiles designed for a 0.17 Hz target frequency technically feasible. This would result in a mass reduction of up to 25% with respect to the stiffest monopiles assessed. If the adoption of higher steel grade and the B2 graded S-N curve is combined, the monopiles with a 0.15 Hz target frequency become technically feasible and a steel usage reduction of up to 35% can be realized.

Based on the fundamental limiting factors for monopiles found, also a novel hybrid floating-fixed bottom concept is proposed aiming at steel weight reduction. This alternative comprises a hinged monopile anchoring a semi-floater supporting a 15 MW wind turbine. The software ANSYS AQWA is used to perform the hydrodynamic analysis of the semi-like platform in waves based on the potential flow theory by considering the second-order wave exciting force. In this study, the linearized potential-flow hydrodynamic radiation and diffraction problems in the frequency domain were firstly solved by adopting the 3-D panel method. Subsequently, the hydrodynamic coefficients and wave loading data were transformed to time domain as a system loading input. The quadratic transfer function (QTF) matrices with different frequencies and directions were adopted for the calculation of slow-drift forces. The non-linear quadratic drag in a real system that is not included in the potential flow is introduced via careful use of Morison's elements. The turbine tower and mooring system are included in Ansys time domain model. The reaction forces at the hinge are recorded and used for further optimisation of the foundation monopile. This novel concept shows 2 desirable features, 1 moving the system resonance regions out of the forcing excitation zones and 2 decoupling the dynamic interactions between the aerodynamics at RNA and the hydrodynamics experienced by the monopile foundation. Even though there is no resonant response, the loading is still large due to much increased structural dimensions around the waterline. Although this novel concept shows promising technical feasibility, it does add complexity to the system and does not (yet) result in steel reduction.

7.2. Recommendations

As the research aims to capture highly complex interaction of multiple variables in analytic and parametric models, several assumptions and simplifications had to be made. This leads to high level results on the technical feasibility of the monopile and the introduced hybrid concept in deep water. It is key to assess all possible limiting factors in a detailed manner and this Section will present the recommended topics for further research. The recommendations are divided into two Sections: general recommendations and recommendations specifically for the hybrid novel concept.

7.2.1. General Recommendations

- As this research focused on the technical feasibility of wind turbine foundations rather than the wind turbine itself, a reference turbine and turbine tower were directly adopted. Currently the optimization of the turbine tower and the foundation pile are two separate analyses, which use each other's output to iterate their designs. The turbine tower design is typically governed by aerodynamic induced fatigue damage. However, with the increasing water depth, significant bending stress response also shows to be induced by the waves acting on deep water monopiles. It is recommended to assess whether these extra forces still yield a technically feasible wind turbine tower and connection to the monopile. If more stiffness is required, the dynamics of the system will be strongly changed and the overall system needs to be re-assessed. An overarching holistic design approach including both the foundation and turbine is recommended to reduce the required steel. In this approach also the manufacturability should be assessed for possible cost reductions.

- DNV standards require the multiplication of the initially determined fatigue damage with a Damage Design Factor. This factor ranges from 1 to 3 depending on the situation, which is a broad range. For the monopiles a DFF of 2.0 is dictated, but the exact reasoning remains vague. Possible reduction of this factor would enlarge the system's resistance against fatigue and is therefore a recommendation for further research.

- This thesis focused on the technical feasibility of the monopile. It already stated that cost reduction is very important in the energy industry. Therefore, financial feasibility is a possible show stopper for the monopile. Total costs including all components along the full lifetime of the support structure should be estimated and compared with alternative support structures. **The output monopile geometries will be used by Sif to compare the financial feasibility of the monopile with respect to jacket foundations in deep water.**

- Forces induced by the rotor such as thrust fluctuations or side-side excitation due to mass imbalance are neglected in this thesis. For a full analysis their effect should be quantified. As resonance with the rotor frequencies is avoided and the aerodynamic forcing is small with respect to the hydrodynamic forcing, these effect are expected to be limited.

- An analytical approach to determine the accumulated fatigue damage was used to reduce the computation time and assess the impact of different variables. A full computational model including components such as the variability in magnitude, shear and turbulence of wind forcing, complete (time) varying damping components and the rotor controller (pitch and torque control and lagging) must be assessed to check the validity of the analytical approach, which might be conservative.

- In this thesis the effect of different soil types on the system is modelled using equivalent linear springs. In reality soil reaction is highly non-linear, locality/depth dependent and will also vary over time. Additionally, the simplification is based on literature on earlier monopile foundations. However, due to the increased pile diameters, this reaction might be different for the XL monopiles. A full non-linear soil analysis is required to verify the assumptions or introduce a suitable soil model.

- In the thesis the effects of possible ice are neglected. Ice can cause serious damage to the system and is potentially present in deep water sites such as the northern North sea. Ice growth on the monopile increases the loading surface and volume and ice impact can also induce significant forces itself. The impact of ice occurrence should be assessed.

- Only two load cases are assessed during the thesis (rated and survival). However, a load case that can cause significant forces is the emergency stop of the turbine. Another load case (DNV DLC 5.1 [25]) should be assessed to quantify this forcing, not only on the monopile but also on the turbine tower and connection.
- Next to the proposed steel reduction strategies, many alternative solution to increase stiffness without adding steel weight. can be investigated. A proposed strategy for further research is increasing the stiffness by means of cross-bracing or sand/grout fill rather than increasing the dimensions.
- The analyses are only conducted for one reference site (Hywind Scotland) with highly severe wind and wave conditions. It is recommended to run the same analysis for a set of locations and corresponding environmental conditions to assess the feasible areas of deployment.

7.2.2. Hybrid Floating-Fixed Bottom Concept

- Due to the limited time a reference semi-sub developed for the 15 MW reference turbine was adopted for the hinged concept. This semi-sub is designed for a catenary mooring system, whereas a different geometry might be required for the proposed concept. For example, as the heave motions are restricted and damping in this degree of freedom is this not required, the horizontal pontoons can possibly be reduced to a bracing connection which could lead to steel reduction. A top part optimization study is recommended if further feasibility analysis of this concept is pursued in the future. Also optimization of the exact optimal vertical joint location could be assessed.
- A critical component to the proposed concept is the universal joint. Joints have been used in offshore practice before, but for different purposes. The technical feasibility and design of such a joint is recommended accounting for the different forces which are expected during the lifetime (e.g. yaw moment, axial and shear forces).
- Due to the buoyant elements an extra force component with respect to the conventional monopile is induced on the soil, namely a vertical upward buoyant force. The interaction and required foundation (e.g. suction bucket, conventional pile, multiple piles) is a recommendation for further research.
- The universal joint allow the top part to move freely in the pitch and roll direction. The effect of this movement on the power production is an important topic for further research, as this might reduced the 'true' power rating of the turbine. This possible interaction with RNA/controller and impact on power generation should be subject to further study.

A

Optimization Process Flowchart

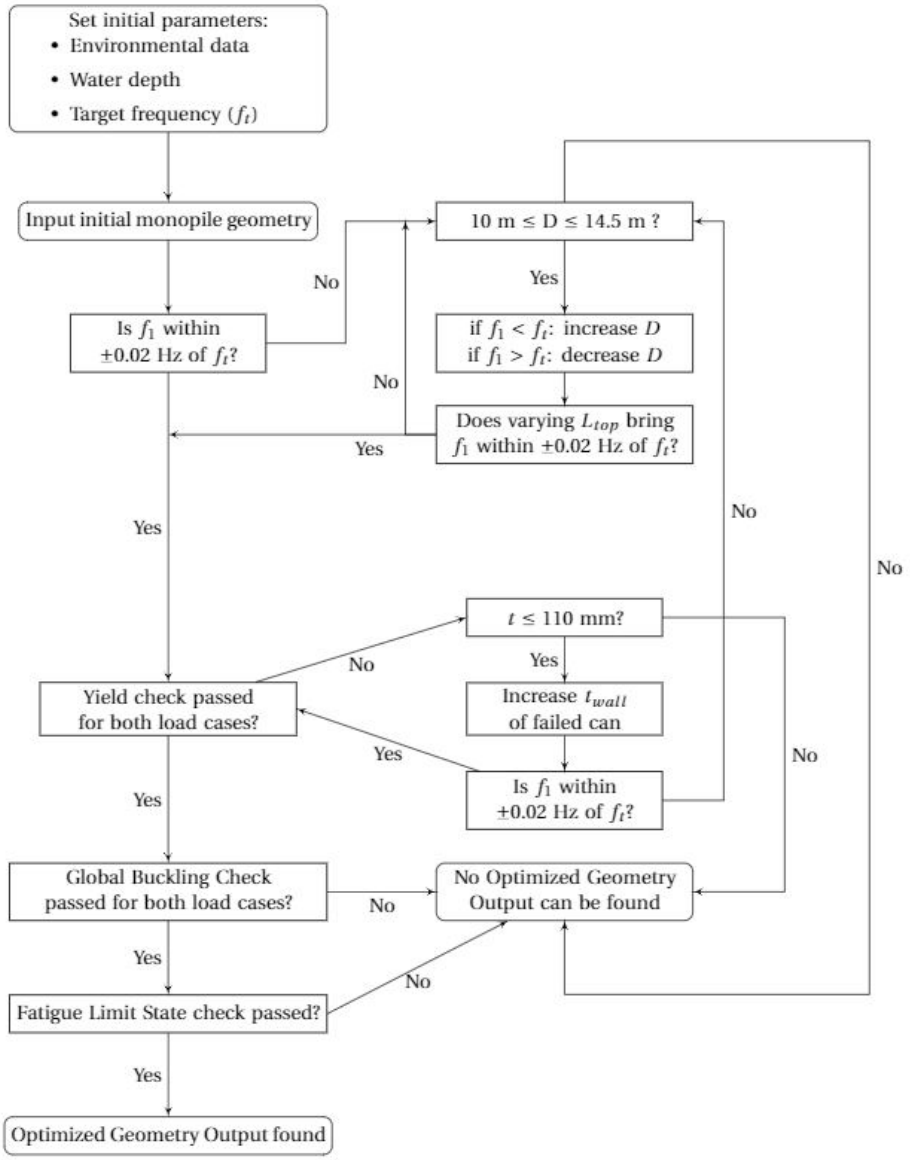

Figure A.1: Geometry Optimization Flowchart

B

UMaine Volturn US-S Reference Floater

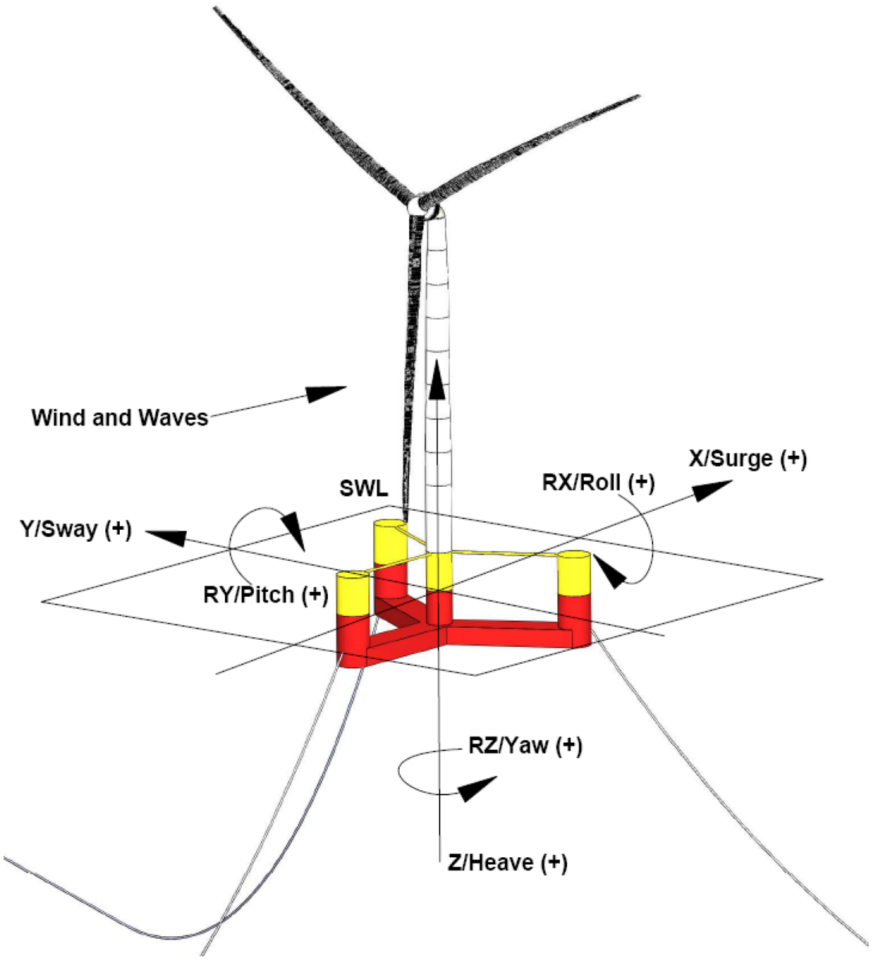

Figure B.1: Floating Offshore Wind Turbine Reference Coordinate System [2]

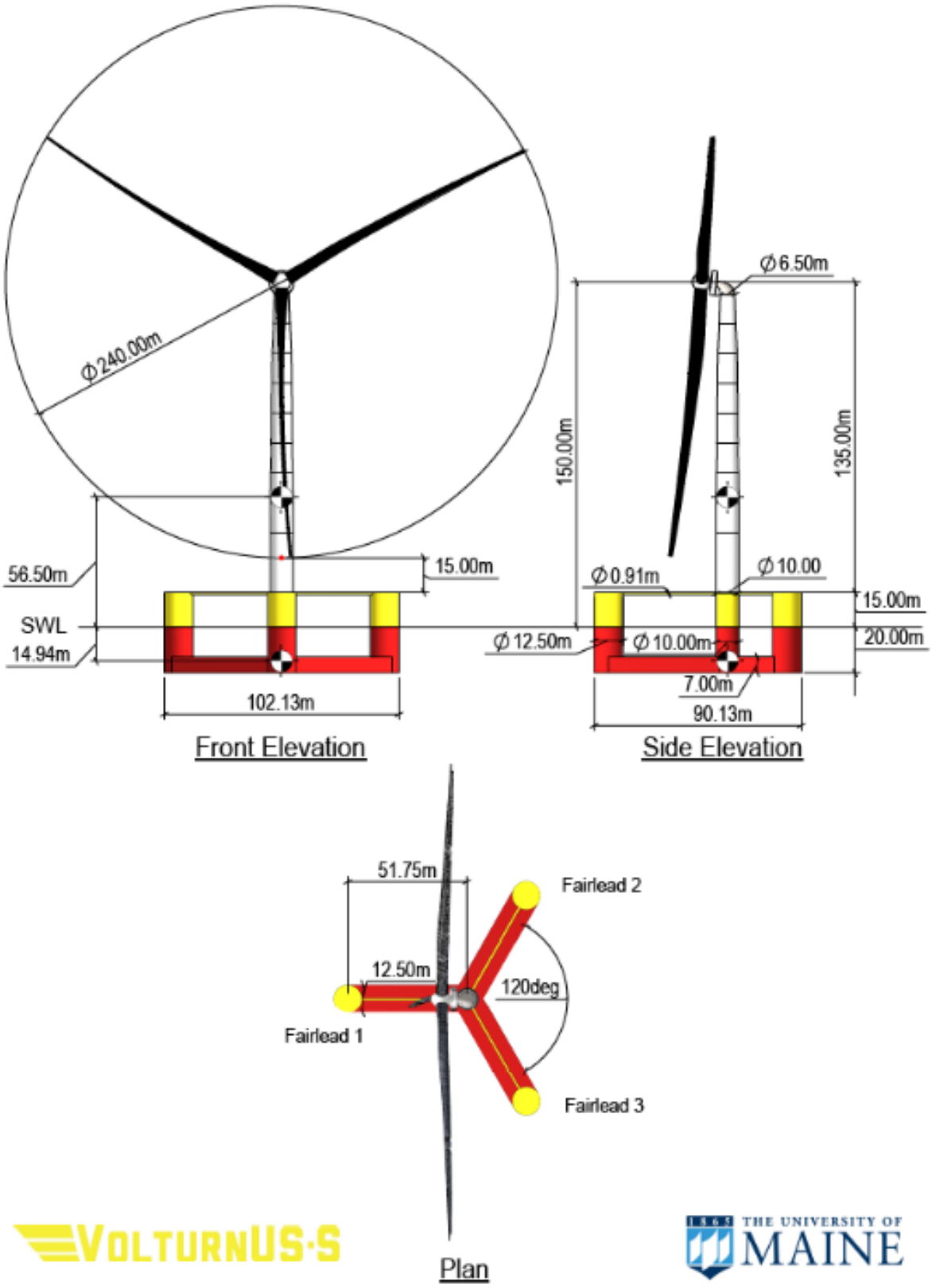

Figure B.2: General Arrangement [2]

Table B.1: Mooring System Properties [2]

Parameter	Units	Value
Mooring System Type	-	Chain Caternary
Line Type	-	R3 Studless Mooring Chain
Line Breaking Strength	kN	22,286
Number of Lines	-	3
Anchor Depth	m	200
Fairlead Depth	m	14
Anchor Radial Spacing	m	836.6
Fairlead Radial Spacing	m	58
Nominal Chain Diameter	mm	185
Dry Line Linear Density	kg/m	685
Extensional Stiffness Line	MN	3270
Line Unstretched Length	m	850
Fairlead Pretension	kN	2,437
Fairlead Angle from SWL	°	56.4

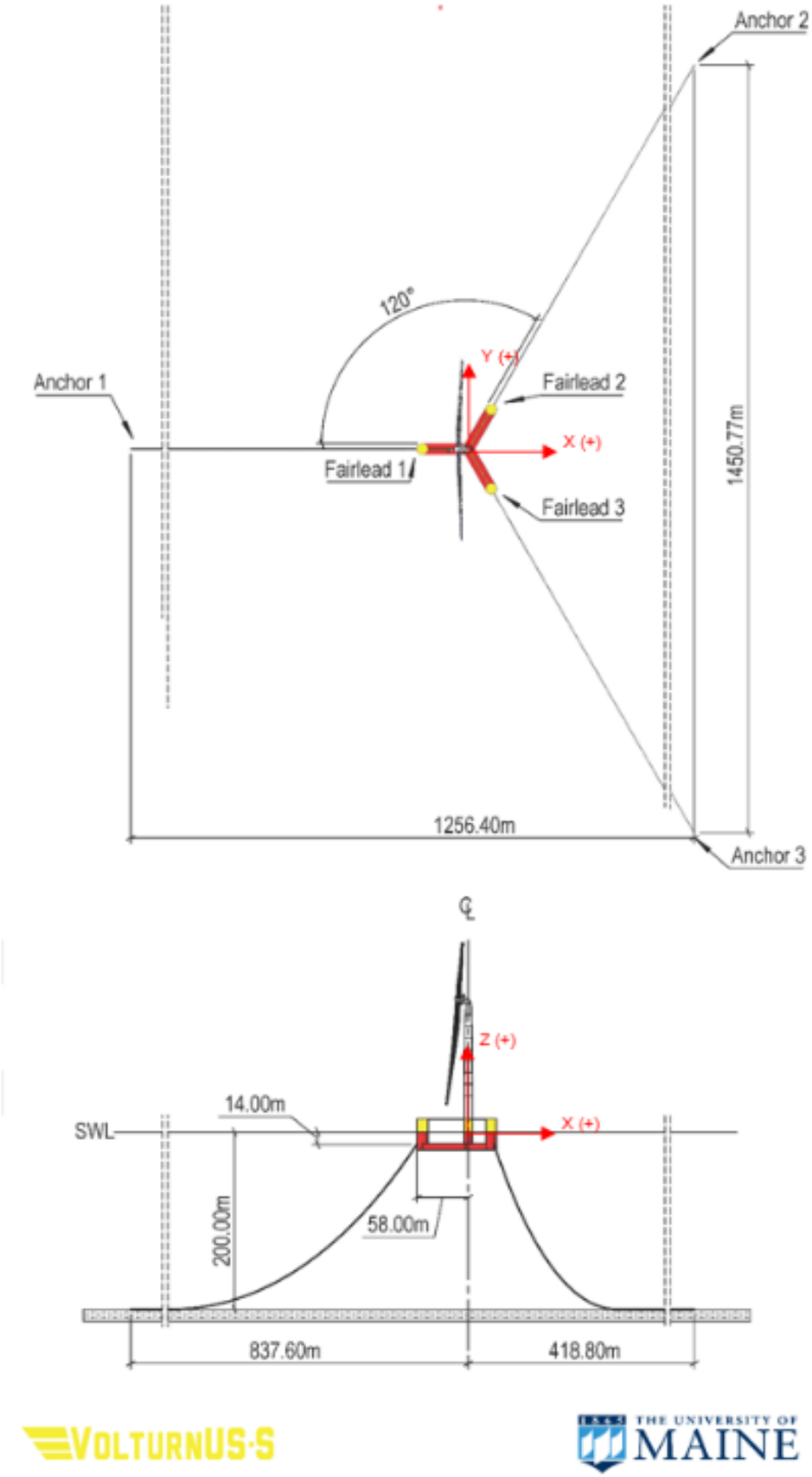

Figure B.3: Mooring system arrangement within the inertia frame shown in plan (top) and elevation (bottom) views [2]

C

Fatigue Check Turbine Tower

The dynamic analytical model of the offshore wind turbine showed that due to the relative stiffness differences between the monopile and the turbine tower, the system responds to wave cycles in a whip-like or fish tailing manner. The wave induced vibration of the monopile foundation is transferred to the turbine tower resulting in large deflections of the top part. In order to estimate whether this bending of the turbine tower will result in technical limitation for using monopile foundations for large turbines in deep waters, the bending stresses at the turbine base are extracted in a similar fashion to the FLS analysis as described in Chapter 5.

Figure C.1 shows the bending stress to frequency response function of the turbine tower base for water depths of 60 and 120 meter and the three target frequencies (0.15, 0.17 and 0.20 Hz) in loose soil against a unit wave height of 1 meter. It shows that contrary to the bending stress of the monopile base, the magnitude of response at the tower base is not independent of water depth. Where the monopile base dimensions increased for deeper waters, the turbine tower stays the same. The bending of the tower, however, does increase for deeper waters resulting in higher bending stress response.

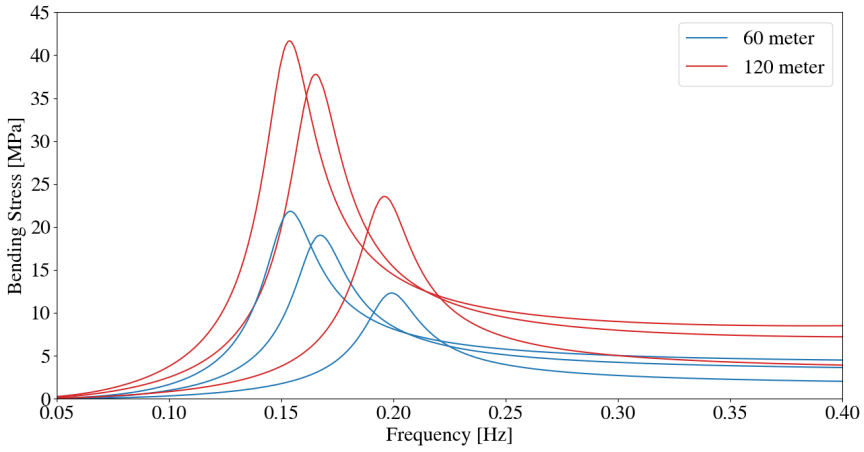

Figure C.1: Bending Stress Frequency Response Function of Tower Base

Tables C.1 and C.2 show the unity checks resulting from the FLS analysis. For the analysis of the tower base, S-N curves for welds in air rather than seawater can be used, which are slightly more tolerant [22]. It shows that the resistance against fatigue decreases significantly over the water depth range. The turbine tower base shows similar resistance against wave induced fatigue damage to the monopile for 60 meter water depth. However, for 120 meter water depth, the turbine base is significantly more critical than the monopile base. At this water depth, only the turbines supported by a 0.20 Hz monopile pass the FLS check.

Table C.1: 60 m Water Depth FLS Results Tower Base

SN curve	0.15 Hz	0.17 Hz	0.20 Hz
D	17.64	3.18	0.05
C1	8.94	1.33	0.02
B2	0.45	0.24	0.00

Table C.2: 120 m Water Depth FLS Results Tower Base

SN curve	0.15 Hz	0.17 Hz	0.20 Hz
D	127.97	36.86	2.00
C1	65.56	18.94	0.81
B2	1.71	1.47	0.15

It must be noted that the actual fatigue calculation for the turbine tower is more complex. The wind induced fatigue damage will have a larger role due to the smaller dimensions of the tower. Also, the type of connection between the monopile and the turbine tower will have a large impact on the dynamic response of the system. Stress concentrations in the connection also need to be counted for where geometric and stiffness discontinuities arise.

The results indicate that for the more slender monopiles in deeper waters, a stiffer turbine tower is required. This increase of stiffness influences the dynamic behaviour of the system by increasing its first natural frequency but also increasing the bending stress response at the base. When a stiffer tower is adopted, the foundation design must be re-assessed. As the increase of stiffness of the turbine tower increases the first natural frequency, the stiffness of the monopile would have to decrease to reach the target first natural frequency. Decreasing the stiffness of the monopile quickly reduces the system's resistance against forcing. However, if the target frequency criterion is lifted, the increase of stiffness of the turbine tower leads to a higher first natural frequency for the same monopile dimensions. This moves the first natural frequency away from the most occurring wave frequencies, which is very desirable in order to reduce resonance. This comes at an obvious cost of more structural steel. Over all, the monopile dimensions influence the turbine tower and vice versa. Therefore a holistic design approach including both the tower and the pile is advised.

Bibliography

[1] Pakhshan Ahmadian. *Effect of Hydrodynamic Forces on Spanning Pipes*. Master thesis, Eastern Mediterranean University, Gazimağusa, North Cyprus, 2015.

[2] Christopher Allen, Anthony Viselli, Habib Dagher, Andrew Goupee, Evan Gaertner, Nikhar Abbas, Matthew Hall, and Garrett Barter. Definition of the UMaine VolturnUS-S Reference Platform Developed for the IEA Wind 15-Megawatt Offshore Reference Wind Turbine. Technical report, National Renewable Energy Laboratory, Golden, CO, 2020. URL https://www.nrel.gov/docs/fy20osti/76773.pdf.

[3] Bård Amundsen. World's highest waves form west of Norway, 2018. URL https://sciencenorway.no/forskningno-norway-oceans/worlds-highest-waves-form-west-of-norway/1455407.

[4] Lászlõ Arany, Subhamoy Bhattacharya, John Macdonald, and S. John Hogan. Simplified critical mudline bending moment spectra of offshore wind turbine support structures, 2015. ISSN 10991824.

[5] Laszlo Arany, S. Bhattacharya, John Macdonald, and S.J. Hogan. Design of monopiles for offshore wind turbines in 10 steps. *Soil Dynamics and Earthquake Engineering*, 92:126–152, jan 2017. ISSN 02677261. doi: 10.1016/j.soildyn.2016.09.024. URL http://www.sciencedirect.com/science/article/pii/S0267726116302937https://linkinghub.elsevier.com/retrieve/pii/S0267726116302937.

[6] Hasan Bagbanci, D. Karmakar, and C. Guedes Soares. Comparison of Spar and Semisubmersible Floater Concepts of Offshore Wind Turbines Using Long-Term Analysis. *Journal of Offshore Mechanics and Arctic Engineering*, 137(6), dec 2015. ISSN 0892-7219. doi: 10.1115/1.4031312. URL https://asmedigitalcollection.asme.org/offshoremechanics/article/doi/10.1115/1.4031312/444916/Comparison-of-Spar-and-Semisubmersible-Floater.

[7] Subhamoy Bhattacharya. Challenges in Design of Foundations for Offshore Wind Turbines. *Engineering & Technology Reference*, (October), jan 2014. ISSN 2056-4007. doi: 10.1049/etr.2014.0041. URL https://digital-library.theiet.org/content/reference/10.1049/etr.2014.0041.

[8] Ghorai Bithin, R. Panneer Selvam, and R. Sundaravadivelu. Hydrodynamic Responses of a Single Hinged and Double Hinged Articulated Towers. In *Volume 7: Ocean Engineering*, number August 2017. American Society of Mechanical Engineers, may 2015. ISBN 978-0-7918-5655-0. doi: 10.1115/OMAE2015-41524. URL https://asmedigitalcollection.asme.org/OMAE/proceedings/OMAE2015/56550/St.John's,Newfoundland,Canada/280245.

[9] Mark L. Brodersen and Jan Høgsberg. Damping of Offshore Wind Turbine Tower Vibrations by a Stroke Amplifying Brace. *Energy Procedia*, 53(C):258–267, 2014. ISSN 18766102. doi: 10.1016/j.egypro.2014.07.235. URL https://linkinghub.elsevier.com/retrieve/pii/S1876610214011126.

[10] Adrijana Buljan. Final WindFloat Atlantic Turbine Ready to Go Home, 2020. URL https://www.offshorewind.biz/2020/05/19/final-windfloat-atlantic-turbine-ready-to-go-home/.

[11] Tony Burton, Nick Jenkins, David Sharpe, and Ervin Bossanyi. Appendix : Lift and Drag of Aerofoils. In *Wind Energy Handbook*, chapter Appendix A, pages 156–172. John Wiley & Sons, Ltd, second edition, 2011. ISBN 9781119992714. doi: 10.1002/9781119992714.

[12] Chao Chen and Philippe Duffour. Modelling damping sources in monopile-supported offshore wind turbines. *Wind Energy*, 21(11):1121–1140, 2018. ISSN 10991824. doi: 10.1002/we.2218.

[13] Jun-ling Chen and Christos T Georgakis. Spherical tuned liquid damper for vibration control in wind turbines. *Journal of Vibration and Control*, 21(10):1875–1885, jul 2015. ISSN 1077-5463. doi: 10.1177/1077546313495911. URL http://journals.sagepub.com/doi/10.1177/1077546313495911.

[14] John Codrington. On the effect of plate thickness on post-overload fatigue crack growth. *International Journal of Fracture*, 155(1):93–99, 2009. ISSN 03769429. doi: 10.1007/s10704-009-9322-y.

[15] Shane Colwell and Biswajit Basu. Tuned liquid column dampers in offshore wind turbines for structural control. *Engineering Structures*, 31(2):358–368, 2009. ISSN 01410296. doi: 10.1016/j.engstruct.2008.09.001. URL http://dx.doi.org/10.1016/j.engstruct.2008.09.001.

[16] C1 Connections. C1 Wedge Connection, 2021. URL https://c1connections.com/.

[17] Jason Deign. More 'Subsidy-Free' Offshore Wind Emerges in Europe, 2018. URL https://www.greentechmedia.com/articles/read/what-it-takes-to-get-subsidy-free-offshore-wind.

[18] Dillinger. Expert Interview, 2-7-2021, jul 2021.

[19] DNVGL-CG-0127. Finite element analysis. Standard, DNV GL, 2015.

[20] DNVGL-CG-0130. Wave loads. Standard, DNV GL, 2018.

[21] DNVGL-OS-B101. Metallic Materials. Standard, DNV GL, 2017.

[22] DNVGL-RP-C203. Fatigue design of offshore steel structures. Standard, DNV GL, 2014.

[23] DNVGL-RP-C205. Environmental conditions and environmental loads. Standard, DNV GL, 2014.

[24] DNVGL-ST-0126. Support structures for wind turbines. Standard, DNV GL, 2018.

[25] DNVGL-ST-0437. Loads and site conditions for wind turbines. Standard, DNV GL, 2016.

[26] Dogger Bank Wind Farm. Doggger Bank Wind Farm, 2021. URL https://doggerbank.com/about/.

[27] DOT BV. Slip Joint Offshore Research project (SJOR). URL https://grow-offshorewind.nl/project/sjor.

[28] Empire Engineering. Foundation Ex: The tech sessions: How deep can the monopile go?, 2020.

[29] Equinor. Hywind Tampen: the world's first renewable power for offshore oil and gas, 2021. URL https://www.equinor.com/en/what-we-do/hywind-tampen.html.

[30] European Commission. Clean Energy Transition – Technologies and Innovations. Technical report, European Commission, Brussels, 2020. URL https://ec.europa.eu/energy/topics/energy-strategy/energy-union/fifth-report-state-energy-union{_}en.

[31] European Investment Bank. Golfe du Lion Floating Offshore (EFGL), 2020. URL https://www.eib.org/en/projects/pipelines/all/20180690.

[32] European Standards. S355 European Standard Steel. Technical Report 7, 2004.

[33] Tim Fischer, Patrick Rainey, Ervin Bossanyi, and Martin Kühn. Study on control concepts suitable for mitigation of loads from misaligned wind and waves on offshore wind turbines supported on monopiles. *Wind Engineering*, 35(5):561–574, 2011. ISSN 0309524X. doi: 10.1260/0309-524X.35.5.561.

[34] Evan Gaertner, Jennifer Rinker, Latha Sethuraman, Frederik Zahle, Benjamin Anderson, Garrett E. Barter, Nikhar J. Abbas, Fanzhong Meng, Pietro Bortolotti, Witold Skrzypinski, George N. Scott, Roland Feil, Henrik Bredmose, Katherine Dykes, Matthew Shields, Christopher Allen, and Anthony Viselli. Definition of the IEA 15-Megawatt Offshore Reference Wind Turbine. Technical report, National Renewable Energy Laboratory, Golden, CO, 2020. URL https://www.nrel.gov/docs/fy20osti/75698.pdf{%}0ANREL.

[35] General Electric. GE's Haliade-X 12 MW, most powerful wind turbine operating to date, obtains full type certificate, 2020. URL https://www.ge.com/news/press-releases/ge-haliade-x-12-mw-most-powerful-wind-turbine-operating-to-date-obtains-full-type-certificate.

[36] Global Wind Energy Council. China installed half of new global offshore wind capacity during 2020 in record year, 2021. URL https://gwec.net/china-installed-half-of-new-global-offshore-wind-capacity-during-2020-in-record-year/.

[37] Sven-Erik Gryning. Wind Profiles, 2016. URL https://www.youtube.com/watch?v=Rwz0m6p7RQk{&}feature=youtu.be.

[38] Mats Gustafsson. A study of thickness effect on fatigue in thin welded high strength steel joints. *Steel Research International*, 77(12):873–881, 2006. ISSN 16113683. doi: 10.1002/srin.200606475.

[39] Thijs De Haan. *Buckling monopiles: Stability of an monopile based offshore wind turbine*. Master thesis, Delft University of Technology, 2020.

[40] Jan Hafele, Christian G. Gebhardt, and Raimund Rolfes. Innovative design of a hybrid-type jacket for 10MW turbines. Technical Report 308974, INNWIND, 2016.

[41] O. L. Hansen. *Basic Rotor Aerodynamics applied to Wind Turbines*. Number January. Lynhby, 1998. ISBN 87-7475-192-1. URL https://www.osti.gov/etdeweb/servlets/purl/618185.

[42] Leon Harland and Jan H Vugts. Analytic expression for the first natural period of a stepped tower. Technical report, 1996. URL https://ocw.tudelft.nl/wp-content/uploads/NF{_}stepped{_}monotower{_}{_}Rayleigh{_}.pdf.

[43] K W Hermans and J M Peeringa. Future XL monopile foundation design for a 10 MW wind turbine in deep water. Technical report, Energieonderzoek Centrum Nederland, Petten, 2016. URL https://www.ecn.nl/publications/PdfFetch.aspx?nr=ECN-E--16-069.

[44] Leo H Holthuijsen. *Waves in Oceanic and Coastal Waters*. Cambridge University Press., New York, 2007. ISBN 978-0-511-27021-5.

[45] S Hsu, E Meindl, and D Gilhousen. Determining the Power-law Wind-profile Exponent under Near-Neutral Stability Conditions at Sea. *Journal of Applied Meteorology of Applied Meteorology*, 33(6), 1994. doi: 10.1175/1520-0450(1994)033<0757:DTPLWP>2.0.CO;2. URL http://library1.nida.ac.th/termpaper6/sd/2554/19755.pdf.

[46] 2019 IEA, Offshore Wind Outlook. Offshore Wind Outlook 2019: World Energy Outlook Special Report. Technical report, International Energy Association, Paris, 2019.

[47] International Electrotechnical Commission (IEC). IEC 61400-1 Wind turbines - Part 1: Design Requirements, 2005. ISSN 21559600.

[48] IRENA International Renewable Energy Agency. Renewable Power Generation Costs in 2018. Technical report, International Renewable Energy Agency, Abu Dhabi, 2018. URL https://www.irena.org/-/media/Files/IRENA/Agency/Publication/2018/Jan/IRENA{_}2017{_}Power{_}Costs{_}2018.pdf.

[49] J M J Journée, W W Massie, and R H M Huijsmans. OFFSHORE HYDROMECHANICS Third Edition (2015). 2015.

[50] Yu-Shu Kuo, Martin Achmus, and Khalid Abdel-Rahman. Minimum Embedded Length of Cyclic Horizontally Loaded Monopiles. *Journal of Geotechnical and Geoenvironmental Engineering*, 138(3):357–363, 2012. ISSN 1090-0241. doi: 10.1061/(asce)gt.1943-5606.0000602.

[51] Michel Kurstjens. Michel Kurstjens: Product Strategy Director SIF Group, 2020.

[52] Matthew A. Lackner and Mario A. Rotea. Passive structural control of offshore wind turbines. *Wind Energy*, 14(3):373–388, apr 2011. ISSN 10954244. doi: 10.1002/we.426. URL http://doi.wiley.com/10.1002/we.426.

[53] David JC MacKay. Sustainable energy - without hot air, 2020. ISSN 18653537. URL http://www.withouthotair.com/cB/page{_}265.shtml.

[54] Martin Mathiesen, Anja K Meyer, and Børge Kvingendal. Hywind Buchan Deep Metocean Design Basis RE2014-002. Technical report, Statoil, Scotland, 2014.

[55] Matthew Hannon, Eva Topham, James Dixon, David Mcmillan, and Maurizio Collu. Offshore wind, ready to float? Global and UK trends in the floating offshore wind market. Technical report, University of Strathclyde, Glasgow, 2019. URL https://doi.org/10.17868/69501.

[56] NEN. Eurocode 3: Ontwerp en berekening van staalconstructies - Deel 1-1: Algemene regels en, 2003.

[57] This Norsok, The Norwegian Oil, The Federation, and Norwegian Industry. Norsok Standard N-003, 2013.

[58] Ocean Energy Resources. Revolutionary offshore transfer technology for Hornsea Two, 2020. URL https://ocean-energyresources.com/2020/10/16/revolutionary-offshore-transfer-technology-for-hornsea-two/.

[59] Ki Yong Oh, Woochul Nam, Moo Sung Ryu, Ji Young Kim, and Bogdan I. Epureanu. A review of foundations of offshore wind energy convertors: Current status and future perspectives. *Renewable and Sustainable Energy Reviews*, 88(May):16–36, 2018. ISSN 18790690. doi: 10.1016/j.rser.2018.02.005.

[60] M Oosterhof and S Kleinhuis. Tightening Bolts: A presentation about complexities of using large bolts. Technical report, Van Oord, 2014. URL http://www.maritimecampus.nl/sites/default/files/Groep6-Torqueingbolts.pdf.

[61] Semyung Park, Matthew A Lackner, Pariya Pourazarm, Arturo Rodríguez Tsouroukdissian, and John Cross-Whiter. An investigation on the impacts of passive and semiactive structural control on a fixed bottom and a floating offshore wind turbine. *Wind Energy*, 22(11):1451–1471, 2019. ISSN 10991824. doi: 10.1002/we.2381.

[62] John Parnell. Vestas Launches World's Largest Turbines as 'Big 3' Competition Ramps Up, 2021. URL https://www.greentechmedia.com/articles/read/vestas-launches-worlds-largest-turbines-as-big-3-competition-ramps-up.

[63] M. M. Pedersen. Thickness Effect in Fatigue of Welded Butt Joints: A Review of Experimental Works. *International Journal of Steel Structures*, 19(6):1930–1938, 2019. ISSN 20936311. doi: 10.1007/s13296-019-00254-y.

[64] Martin Pettersson. *Telescopic Tower Facilitating Installation of 12 MW*. Bachelor thesis, Uppsala University, Uppsala, 2020.

[65] H.G. Poulos and E.H. Davis. *Pile foundation analysis and design*, volume 18. Wiley, New York, 1981. ISBN 0-471-02084-2. doi: 10.1016/0148-9062(81)90191-1. URL http://worldcat.org/isbn/0471020842.

[66] Quest Float Wind Energy. Hywind Scotland. Technical report, Quest Float Wind Energy, LLC, Scotland, 2017.

[67] Mouafo Teifouet Armand Robinson and Zhenyu Wang. The effect of the TMD on the vibration of an offshore wind turbine considering three soil-pile-interaction models. *Advances in Structural Engineering*, 2021. ISSN 20484011. doi: 10.1177/13694332211008316.

[68] Scottish Government. Social and Economic Impact Assessment Scoping Report (Sectoral Marine Plan for Offshore Wind Encompassing Deep Water Options). Technical Report June, The Scottish Government, Edinburgh, 2018. URL https://www2.gov.scot/Topics/marine/marineenergy/Planning/smp-scoping-consultation.

[69] M. L.A. Segeren and N. F.B. Diepeveen. Influence of the rotor nacelle assembly mass on the design of monopile foundations. *Heron*, 59(1):17–36, 2014. ISSN 15744078.

[70] Marc Seidel. Substructures for offshore wind turbines - Current trends and developments. *Festschrift Peter Schaumann*, pages 363–368, 2014. doi: 10.2314/GBV.

[71] Marc Seidel. Marc Seidel: Principal Engineer Siemens Gamesa, 2021.

[72] M V Sickler. *Offshore Wind Farm Optimisation*. Master thesis, University of Technology Delft, 2020.

[73] Siemens AG. Brochure of Siemens Wind Turbine SWT-3.6-107, 2011.

[74] Siemens Gamesa. SG 14-222 DD Offshore Wind Turbine, 2020. URL https://www.siemensgamesa.com/products-and-services/offshore/wind-turbine-sg-14-222-dd.

[75] Emil Smilden, Asgeir Sørensen, and Lene Eliassen. Wind Model for Simulation of Thrust Variations on a Wind Turbine. *Energy Procedia*, 94(1876):306–318, 2016. ISSN 18766102. doi: 10.1016/j.egypro.2016.09.188. URL http://dx.doi.org/10.1016/j.egypro.2016.09.188.

[76] StatOil. Hywind Scotland Pilot Park - Environmental Statement. Technical Report April, Statoil, 2015.

[77] Steelwind Nordenham. Beyond XXL – Slim Monopiles for Deep-Water Wind Farms, 2020. URL https://www.offshorewind.biz/2020/05/11/beyond-xxl-slim-monopiles-for-deep-water-wind-farms/.

[78] Niels Jacob Tarp-Johansen, Lars Andersen, Erik Damgaard Christensen, Christian Mørch, Sten Frandsen, and Bjarne Kallesøe. Comparing Sources of Damping of Cross-Wind Motion. In *European Offshore Wind 2009 : Conference & Exhibition : 14-16 September, Stockholm, Sweden*, Stockholm, 2009. The European Wind Energy Association. URL https://vbn.aau.dk/en/publications/comparing-sources-of-damping-of-cross-wind-motion.

[79] Jorne Van der Ploeg. *Perforation of Monopiles to Reduce Hydrodynamic Loading*. Master thesis, Delft University of Technology, 2021.

[80] J Van der Tempel. *Design of Support Structures for Offshore Wind Turbines*. Phd thesis, Delft University of Technology, Delft, 2006.

[81] J. Van Der Tempel and D. Cerda Salzmann. AERODYNAMIC DAMPING IN THE DESIGN OF SUPPORT STURCTURES FOR OFFSHORE WIND TURBINES. Technical report, Delft University of Technology, Delft.

[82] Joey Velarde. *Design of Monopile Foundations to Support the DTU 10 MW Offshore Wind Turbine*. Master thesis, Delft University of Technology and Norwegian University of Science and Technology, 2016.

[83] V Venugopal, J Wolfram, and B T Linfoot. The properties of extreme waves. Technical report, Heriot-Watt University, Edinburgh, 2005.

[84] Jan H Vugts. *Handbook of Bottom Founded Offshore Structures Part 1. General features of offshore structures and theoretical background*. Eburon Academic Publishers, Delft, 2013. ISBN 978-90-5972796-0.

[85] W. E. De Vries, N. K. Vemula, P. Passon, T. Fischer, D. Kaufer, D.Matha, B. Schmidt, , and F. Vorpahl. Final report WP 4.2: Support Structure Concepts for Deep Water Sites: Deliverable D4.2.8 (WP4: offshore foundations and support structures). *Project UpWind*, pages 18–22, 2011.

[86] Simon Watson, Alberto Moro, Vera Reis, Charalampos Baniotopoulos, Stephan Barth, Gianni Bartoli, Florian Bauer, Elisa Boelman, Dennis Bosse, Antonello Cherubini, Alessandro Croce, Lorenzo Fagiano, Marco Fontana, Adrian Gambier, Konstantinos Gkoumas, Christopher Golightly, Mikel Iribas Latour, Peter Jamieson, John Kaldellis, Andrew Macdonald, Jimmy Murphy, Michael Muskulus, Francesco Petrini, Luca Pigolotti, Flemming Rasmussen, Philippe Schild, Roland Schmehl, Nafsika Stavridou, John Tande, Nigel Taylor, Thomas Telsnig, and Ryan Wiser. Future emerging technologies in the wind power sector: A European perspective. *Renewable and Sustainable Energy Reviews*, 113:109270, 2019. ISSN 18790690. doi: 10.1016/j.rser.2019.109270. URL https://doi.org/10.1016/j.rser.2019.109270.

[87] E. N. Wayman, P. D. Sclavounos, S. Butterfield, J. Jonkman, and W. Musial. Coupled dynamic modeling of floating wind turbine systems. *Offshore Technology Conference 2006: New Depths. New Horizons*, 3: 1587–1608, 2006. doi: 10.4043/18287-ms.

[88] I.L. Wijnant, H.W. van den Brink, and A. Stepek. North Sea wind climatology Part 1: a review of existing wind atlases. Technical Report May, 2014. URL http://www6.knmi.nl/knmi-library/knmipubTR/TR342.pdf.

[89] Kun Xu. Design and Analysis of Mooring System for Semi-submersible Floating Wind Turbines in Shallow Water. (May), 2015. URL https://brage.bibsys.no/xmlui/handle/11250/2350655.